University of Genova

PhD Program in Bioengineering and Robotics

Curriculum Bionanotechnology

Synthesis, Characterization and Toxicological Assessment of a new model of Nanoplastics

Valentina Tolardo

Thesis submitted for the degree of Doctor of Philosophy (XXXIV cycle)

Tutor: Athanassia Athanassiou

Supervisor: Despina Fragouli

Smart Materials Group, Italian Institute of Technology (IIT) and Department of Informatics, Bioengineering, Robotics and Systems Engineering

Declaration

I hereby declare that except where specific reference is made to the work of others, the contents of this dissertation are original and have not been submitted in whole or in part for consideration for any other degree or qualification in this, or any other university. This dissertation is my own work and contains nothing which is the outcome of work done in collaboration with others, except as specified in the text and Acknowledgements. This dissertation contains fewer than 65,000 words including appendices, bibliography, footnotes, tables and equations and has fewer than 150 figures.

Valentina Tolardo

April 2022

Acknowledgments

This thesis is the result of different collaborations and would not have been possible without the contribution of many people. First, I have to thank the Fondazione Istituto Italiano di Tecnologia and my supervisors, Athanassia Athanassiou and Despina Fragouli, for the possibility and the support they offered me during these years. I thank the various collaborators: Stefania Sabella, Andrea Armirotti, and Marina Veronesi, for improving me scientifically. A special thank is to Davide Magrì, his help and support were fundamental, thank you for all your suggestions, help and for the opportunity to meet the F2 unit of JRC. Thank Sabrina Gioria for her patience, she was a great knowledge source that allowed me to learn about the world of cell culture in few time. Thank you also for having supported me scientifically and humanly in the difficulties of every day during my visit to JRC. In the same way, I thank Fumagalli Francesco, Pascal Colpo, and all the F2 Unit in JRC in Ispra for teaching me so much. I am so proud to have been the person who allowed to "test" the efficiency of the protocol for the limitations of the spread of COVD-19 in your unit ;). Thank you very much to Arkadiusz Zych, Giovanni Perotto, Giulia Suarato, Laura Bertolacci and the entire postdoc group for their support scientifically and humanly. Thank you to my laser-room mate Amirreza Shayganpour for our usual conversation during the laser working. In the same way, I thank the technicians and collaborators on which the research carried out in IIT is based. In particular, I thank Lara Marini, Giorgio Mancini, Riccardo Carzino, Federico Catalano, Alessio Romaldini for their support in this work. I also thank my friends that made this adventure rich of friendship, love and several special moments. Starting to Ana, Dagmara, Federica, Fabrizio, Isabella, Gabriele, Giacomo, Marta, Martina, Despoina, Marco. Thank you for a lot of years of free psychotherapy ;) ;) and for all the unique moments together. A special thank you to Gabriella by the JRC, a great friendship was born in a very few time. Thanks to the entire "Hall of FAME sharp group": Danila, Benedetta, Emily, and all the new people who entered that group and made it unique. Thank you also to people that started a new adventure, but they had an important space in these years: Margherita, Giulia Scop, Giulia Mazz and Lia. Thank you to all my robotic friends (as I call them ;)) and to volleyball players and beachers that I met during this PhD, this sport was fundamental for me. Thank also to Smarties Team, our first football team. Special thanks to my twin sister Eleonora and all our special friends Arianna, Marianna, Ilaria, Alessia, and Marta. I am sure this job would have been very difficult without you! Last, but not least, thank you very much to my first fans ☺ my mum, my dad and my "little" sister for your patience to endure all my grumblings during these years (they were a lot ;)). You are the first persons who believed in me.

Abstract

Synthetic plastics were first introduced into the consumer markets in the 1950's. Over the next 70 years, annual global production increased reaching to 367 million metric tons in 2020 [1]. While plastic is a unique material in terms of its versatility, cost-effectiveness and resistance, these same properties, combined with the intensive consumption and rapid disposal of plastic products, have caused its accumulation in the environment. Nowadays, it has been estimated that 0.1% of the total global production (>8.3 billion metric tons) has reached the ocean as plastic marine debris[2–7] and can degrade into small micro and nano sized fragments. Microplastics (MPs) have been detected in numerous aquatic organisms and also in human samples, making significantly important to adopt a risk assessment of this pollutant for the human health. The lack of appropriate methodologies to collect the nanoplastics (NPs) from water systems imposes the formation of engineered models to explore their interactions with biological systems. Frequently, these models are colloidal and chemically synthesized, proving low correlated with the real case conditions. This thesis explores the possibility to fabricate diverse types of plastic particles that can be used as alternative models to the chemical model for a more realistic investigation. In particular, the adopted top-down fabrication approach, based on the laser ablation of polymer films in water, allows obtaining NPs and submicron sized plastic particles starting from bulk materials, mimicking, thus, a naturally occurred degradation pathway. Different typologies of NPs have been developed in this study; starting from the previously reported polyethylene terephthalate (PET) NPs, the methodology was further modified in order to fabricate polycarbonate (PC) NPs. It was revealed that the variation of the energy fluence (F), during the ablation process results in the modification of the size of the formed plastic particles. PC NPs were carefully characterized in terms of chemical/physical properties and stability in different media. Moreover, during the PC NPs formation, various byproducts are also released, also detectable in the PC photo-degradation reactions. Therefore with the herein proposed approach it is offered the possibility to obtain a fully integrated product composed by all the components that are expected to be released in the environment during the photo-degradation of the PC plastic litter. As the oral route has been defined as the main route for human exposure to NPs with the liver a secondary organ of the exposure, the impact of the PC NPs is evaluated using upcyte® hepatocytes as a human liver cell model, an advanced system for assessing *in vitro* nanomaterial hepatotoxicity. Additionally, considering the different types of NPs expected to be present in the environment and the limited outcomes of the conventional cytotoxicity evaluation methods for nanoparticulate matter, different *in vitro* technologies have been explored for the evaluation of different types of NPs. In particular, the toxicological assessment of PC and PET NPs (PET1) synthetized by laser ablation and of PET NPs (PET2) made by nanoprecipitation was explored using combinations of conventional and advanced cytotoxicity evaluation methods. In comparison to the particles made by nanoprecipitation, the laser-ablated NPs are generally smaller, with broader size distributions and a higher degree of oxidation on their surface. Two different cell lines were used: single and a monolayer of HePG2 cells, a standard cell model for hepatic organ, and undifferentiated and differentiated Caco-2 cells, a standard model for the intestinal epithelial barrier. Using conventional colorimetric tests no cytotoxic effects of the exposure to NPs were observed, in terms of both cell viability and membrane integrity. However,

using the High Content Screening (HCS), a multiparametric approach that allows for the monitoring of different cellular characteristics through a high-throughput fluorescence imaging it was revealed that PC NPs are more toxic than PET1 NPs, whereas the PET2 NPs showed no toxicity. Interestingly, on a model of the cellular monolayer and intestinal barrier, none of the NPs induced any measurable toxicity. Therefore, the laser ablation approach allows the formation of NPs of different nature, expanding its application to the different types of polymers. This approach allows obtaining a fully integrated product with all the expected components in the environment, with byproducts by the PC photo-degradation in water added to the NPs population. The results of the toxicological assessment do not show toxicity in cell viability on more complex cellular models, such as gastrointestinal barrier and hepatic monolayer. Still, a potential effect on the hepatic functionality has been revealed on cells closer to the human hepatocyte. The fabrication method has a significant impact on the evaluation of the toxicity of the model. Moreover, it might overcome the possible limitations of the technique used for the toxicological assessment by comparing different technologies.

Table of Contents

List of figures i
List of tables vi
Research Design vii
Motivation background and objectives vii
Outline of the thesis viii
Chapter I - Introduction 1
Plastic in the environment 1
Types of plastics 2
Degradation of plastics in water 3
Microplastics and Nanoplastics 4
Trophic transfer and biomagnification of plastic particles 6
Chapter II - Nanoplastics formed by laser ablation 9
Abstract 9
State of art 9
Models of nanoplastics 9
Laser ablation process 10
Polymer materials 12
Materials and Methods 14
Laser ablation process 14
Profilometer analysis 14
Dynamic Light Scattering (DLS) 14
NPs quantification 14
Results and Discussion 15
Laser ablation on PC 15
Conclusions 19
Chapter III - Characterization and toxicological assessment of PC NPs 20
Abstract 20
State of art 21
NPs generation from plastics 21
Photo-degradation pathways of polycarbonate 21
Hepatotoxicity of nanoplastics 23

Materials and Methods 24
Fabrication of PC NPs and dispersion 24
High-Resolution Scanning Electron Microscopy (HRSEM) 25
Transmission Electron Microscopy (TEM) 25
Raman Analysis 25
X-ray Photoelectron Spectroscopy (XPS) Analysis 25
Dynamic Light Scattering and Zeta Potential Analysis 26
Untargeted Liquid Chromatography - Mass/Mass (LC-MS/MS) analysis 26
^{1}H Nuclear Magnetic Resonance (NMR) analysis 26
Upcyte® Hepatocyte Culture 27
Cell Viability Assay 27
Cytotoxicity Assay 28
Reverse Transcription and Quantitative Real-Time PCR 28
Statistical Analysis 28
Results and Discussion 29
Characterization of the PC laser ablation product 29
Characterization of the leachate during the PC laser ablation 35
Toxicological assessment of PC NPs in upcyte® hepatocytes 40
Conclusions 45
Chapter IV - Exploration of different toxicological evaluation methods for the biological fate of NPs 46
Abstract 46
State of art 46
Toxicological assessment methods 46
High content screening (HCS) 48
Electric cell-substrate impedance sensing (ECIS) technology 48
Materials and Methods 50
NPs synthesis 50
Morphological and chemical characterization of NPs 50
Cytotoxicity Evaluation by colorimetric assays 51
HCS assay 52
ECIS set up procedure 53
Immunocytochemistry analysis 53
Statistical Analysis 54

Results and discussion 54
Physical and morphological characterization of NPs 54
Toxicological assessment by colorimetric assays 58
Cytotoxicity evaluation by high content screening (HCS) 62
Electric cell-substrate impedance sensing (ECIS) technology 70
Immunocytochemistry 73
Conclusions 76
Final conclusions 77
Future perspectives 78
List of publications 78
Other activities 78
References 79

List of figures

Figure 1. Schematic of the physical processes that affect the transport of plastic (pink items) in the ocean.

Figure 2. Plastic demand distribution by resin type.

Figure 3. Weathering processes of plastic pollution in the environment. Weathering proceeds along two co-occurring and synergistic pathways: (I) fragmentation and the release of soluble or volatile components (top of the panel); (II) biofouling and oxidative degradation processes (bottom of the panel).

Figure 4. Potential health effects resulting from the bioaccumulation and biomagnification of NPs, MPs and chemical contaminants in the human body.

Figure 5. Schematics of the laser ablation process at different timescales. The time frame gives insight into the different characteristic times of the main physical process in laser ablation in liquid-phase for femtosecond and nanosecond laser pulses: energy transfer from the laser-excited electron gas to the lattice (a few ps, light blue and red lines), phase transition of the target (above 100 ps, orange line), plasma lifetime (a few μs, yellow line), and bubble lifetime (a few hundreds of microseconds, green line). Each process is included in specific phase listed in the blue elliptic boxes on the left.

Figure 6. PET, PC and PVC molecular structure**.**

Figure 7. The trend of ablation depth as a function of the laser F for PC at different irradiation conditions.

Figure 8. Hydrodynamic diameter (D_H) distribution of PC particles synthetized at three different F.

Figure 9. (a) The trend of D_H of the PVC ablation product as a function of the irradiation F; (b) Hydrodynamic diameter (D_H) distribution of particles synthetized at F 4.52 ± 0.04 J/cm^2.

Figure 10. Calibration curve of PC ablation product to define the concentration.

Figure 11. UV-Vis absorption spectrum of (a) the pristine PC film and (b) the ablation products at different F.

Figure 12. Hydrodynamic diameter (D_H) distribution of PC NPs after filtration and concentration.

Figure 13. Representation of the different components of the laser ablation products, then the PC NPs after a first filtration and concentration and the dispersant after the ultrafiltration with the 30kD Amicon filter.

Figure 14. Photo-Fries rearrangement via the radical process.

Figure 15. Photo-oxidation of polycarbonate.

Figure 16. SEM images of PC ablation product after irradiation at F=2.8 J/cm^2.

Figure 17. TEM images of PC ablation product after irradiation at F=0.9 J/cm^2. Scale bar is reported in each image.

Figure 18. Raman analysis of pristine PC and the ablation product after irradiation at (a) F=2.8 J/cm^2 and (b) F=0.9 J/cm^2.

Figure 19. (a) TEM images and (b) corresponding size distribution analysis. The mean diameter of the NPs is 31.5 nm (scatter intervals = -20.3, +48.9 nm).

Figure 20. Survey XPS spectra of the pristine polymer and of the as-synthesized NPs with the respective elemental composition. NP dispersion drop-casted on Teflon (C_2F_4) substrate.

Figure 21. XPS C1s high resolution spectra of the pristine polymer and of the as-synthesized NPs with the corresponding deconvolutions. NP dispersion drop-casted on Teflon (C_2F_4) substrate.

Figure 22. Atomic bonding distribution from XPS C1s spectra analysis of PC NPs in comparison with the pristine polymer (PC bulk film) and ablated PC polymer.

Figure 23. Z-Pot at different pH of PC NPs. The increasingly negative charge in the basic environment indicates the negative surface charge of the PC-NPs.

Figure 24. Hydrodynamic diameter (D_H) distribution of the starting PC NPs complex (solution before the ultrafiltration separation (red)) and the spectra of the two separated solutions: the dispersant (grey) and the recovered PC NPs (yellow). Milli-Q water spectrum is in blue.

Figure 25. UV-vis spectra of the starting PC NPs complex (solution before the ultrafiltered separation (red)) and the spectra of the two separated solutions: the dispersant (grey) and the recovered PC NPs (yellow).

Figure 26. (a) MS/MS chromatogram of partial intermediates in the leachate detected by Shi et al. P271 after the irradiation of PC MPs; (b) Corresponding MS/MS spectrum of one of the intermediates detected in the dispersant after the separation by the NPs population. The diagnostic MS/MS fragment ions, that confirm P271 structure for our unknown compound, are tagged by black arrows.

Figure 27. High-resolution MS/MS spectra of two isomeric species at 243.1 m/z, likely corresponding to degradation products P243a and P243b reported by Shi et al. 2021.

Figure 28. 1D ^{1}H spectra of the dispersant in black and the dispersant with adding of acetone, methanol and acetic acid in red to confirm the presence of these products in the dispersant.

Figure 29. 1D ^{1}H spectra of the dispersant in black and the dispersant with adding of BPA in red to confirm the presence of these products in the dispersant.

Figure 30. Cell viability by resazurin reduction assay upon (a) 24 and (b) 48 hour exposure and cell membrane integrity by cytotoxicity assay upon (c) 24 and (d) 48 hour exposure. "CTRL" refers to un-treated control cells and "Triton" to the positive control, represented by cells treated with 0.03% Triton X-100. Results are means ± SD of three independent experiments. The symbols ** and **** refer to $p = 0.0012$ and $p < 0.0001$, respectively, calculated *versus* CTRL (ordinary one-way ANOVA). Data courteously provided by Dr. Alessio Romaldini, Nanoregulatory Group of D3-PharmaChemistry-IIT.

Figure 31. Representative images by optical microscope relative to cells treated with different PC NPs concentrations or un-treated for 24 (a) or 48 hours (b). All the images are 40x magnifications (scale bar = 75 µm). Data courteously provided by Dr. Alessio Romaldini, Nanoregulatory Group of D3-PharmaChemistry-IIT.

Figure 32. Cell viability by resazurin reduction assay upon 24 and 48 hour exposure. The cells are treated with PC NPs at 40 µg/mL and an equal volume of dispersant and filtered water (pure water subjected to the ultrafiltration process using the same type of filter and conditions). "CTRL" refers to un-treated control cells. Results are means ± SD of three independent experiments. The symbols ** and **** refer to $p = 0.0012$ and $p < 0.0001$, respectively, calculated *versus* CTRL (ordinary one-way ANOVA). Data courteously provided by Dr. Alessio Romaldini, Nanoregulatory Group of D3-PharmaChemistry-IIT.

Figure 33. Relative gene expression of (a, b) CYP3A4 and (c, d) Albumin in cells treated for 24 and 48 hours with PC NPs at 40 µg/mL and an equal volume of dispersant and filtered water. "CTRL" refers to un-treated control cells. Results are means ± SD of three independent experiments. The symbols *, **, *** and **** refer to $p \leq 0.0495$, $p \leq 0.0078$, $p \leq 0.0004$ and $p < 0.0001$, respectively, calculated *versus* CTRL (ordinary one-way ANOVA). Data courteously provided by Dr. Alessio Romaldini, Nanoregulatory Group of D3-PharmaChemistry-IIT.

Figure 34. Schematic explaining ECIS theory. This shows endothelial cells growing on gold electrodes which are coated with rat tail collagen I. The endothelial cells form a monolayer by forming junctions with each other and the collagen substrate, shown by black and grey bars respectively. Once these junctions are formed, less current, supplied by the electrode, can flow through the cell junctions. This increases the electrical resistance as seen on the graph (right). As the cells become confluent, maximum resistance is achieved and the resistance plateaus. Upon treatment with factors that disrupt the endothelial barrier, the junctions weaken, current flows more freely between the cells and the electrical resistance decreases (blue trace, right).

Figure 35. Imaging of mitotoxicity and cytotoxicity of valinomycin in HeLa cells using the HCS Mitochondrial Health Kit (HCS Mitochondrial Health Kit Protocol (Invitrogen)).

Figure 36. D_H distribution of PC NPs (black), PET1 NPs (red) and PET2 NPs (blue).

Figure 37. Morphology of the a) PC NPs, b) PET1 NPs and c) PET2 NPs by TEM. Scale bar is the same in each panel and represents 100 nm.

Figure 38. Survey XPS spectra of the three different NPs with the respective elemental composition.

Figure 39. XPS C1s high resolution spectra of the three different NPs with the corresponding deconvolutions. NP dispersion drop-casted on Teflon (C_2F_4) substrate.

Figure 40. Atomic bonding distribution from XPS C1s spectra analysis for all NPs types, and comparison with the pristine polymers (PC and PET bulk films).

Figure 41. HepG2 and Caco-2 cell viability after exposure to NPs at the concentration of 10, 20, 40, 80 µg/mL for 24 or 48 h. In the case of PET2 data are represented only at 80 µg/mL (LDH assay). Data are reported as % of cell death (average of three independent experiments ± SD).

Figure 42. Mitochondrial activity of HePG2 cells after exposure to NPs at the concentrations of 1, 10, 20, 40, 80 µg/mL for 24 or 48 h (MTT assay). Data are reported as average of three independent experiments ± SD. $p < 0.001$, $p < 0.01$ and $p < 0.05$ are reported (***, ** and * respectively), calculated versus CTRL (one-way ANOVA).

Figure 43. Representative morphological images of HePG2 cells after different treatments for 24 h. Scale bar at 50 µm for all images.

Figure 44. Cell viability of HePG2 cells exposed to different NPs concentrations or to the PC and PET NPs dispersants at 24 or 48 h. Results are expressed as % cell viability compared to the untreated cells. Data are reported as average of three independent experiments ± SD. Valinomycin (900nM) was used as positive controls. $p < 0.001$, $p < 0.01$ and $p < 0.05$ are reported (***, ** and * respectively), calculated versus CTRL (one-way ANOVA).

Figure 45. Cell viability of Caco-2 cells exposed to different NPs concentrations or to the PC and PET NPs dispersants at 24 or 48 h. Results are expressed as % cell viability compared to the untreated cells. Data are reported as average of three independent experiments ± SD. Valinomycin (900 nM) was used as positive controls. $p < 0.001$, $p < 0.01$ and $p < 0.05$ are reported (***, ** and * respectively), calculated versus CTRL (one-way ANOVA).

Figure 46. Mitochondrial activity of HePG2 cells exposed to different concentration of PC and PET NPs for 24 or 48 h, measured by HCS. Results are expressed as % mitochondrial activity compared to the untreated cells. Valinomycin (900 nM) was used as positive controls. Data are reported as average of three independent experiments ± SD. $p < 0.001$, $p < 0.01$ and $p < 0.05$ are reported (***, ** and * respectively), calculated versus CTRL (one-way ANOVA).

Figure 47. Mitochondrial activity of Caco-2 cells exposed to different concentration of PC and PET NPs for 24 or 48 h, measured by HCS. Results are expressed as % mitochondrial activity compared to the untreated cells. Valinomycin (900nM) was used as positive controls. Data are reported as average of three independent experiments ± SD. $p < 0.001$, $p < 0.01$ and $p < 0.05$ are reported (***, ** and * respectively), calculated versus CTRL (one-way ANOVA).

Figure 48. NPs effects on HePG2 cells on nuclear size (top of the panel) and nuclear intensity (bottom of the panel). Cells were exposed to PC, PET1 or PET2 NPs at concentrations between 10 and 80 µg/mL for 24 or 48 h, stained with Hoechst 33342 and analyzed by HCI. Data are expressed as % nuclear effect normalized to the control (untreated cells) and reported as mean of three independent experiments ± SD.

Figure 49. NPs effects on Caco-2 cells on nuclear size (top of the panel) and nuclear intensity (bottom of the panel). Cells were exposed to PC, PET1 or PET2 NPs at concentrations between 10 and 80 µg/mL for 24 or 48 h, stained with Hoechst 33342 and analyzed by HCI. Data are expressed as % nuclear effect normalized to the control (untreated cells) and reported as mean of three independent experiments ± SD.

Figure 50. Two-way analysis of HePG2 cells exposed to PC, PET1 or PET2 NPs concentrations between 10 and 80 µg/mL for 24 or 48 h. Valinomycin was used as positive control. Results are expressed in function of two different parameters: mitochondrial activity and cellular membrane damage. Data are reported as average of three independent experiments.

Figure 51. Two-way analysis of Caco-2 cells exposed to PC, PET1 or PET2 NPs concentrations between 10 and 80 µg/mL for 24 or 48 h. Valinomycin was used as positive control. Results are expressed in function of two different parameters: mitochondrial activity and cellular membrane damage. Data are reported as average of three independent experiments.

Figure 52. Cell viability of undifferentiated and differentiated Caco-2 cells exposed to different doses of PC, PET1 or PET2 NPs for 24 or 48 h. Data are expressed as % cell viability normalized to the control (untreated cells), and reported as mean of three independent experiments ± SD.

Figure 53. Mitochondrial activity of undifferentiated and differentiated Caco-2 cells exposed to different doses of PC, PET1 or PET2 NPs for 24 or 48 h. Data are expressed as % mitochondrial activity normalized to the control (untreated cells), and reported as mean of three independent experiments ± SD.

Figure 54. Electrical a) impedance, b) resistance and c) capacitance in differentiated Caco-2 cells. After a recovery period of 12 days, cells were re-exposed for others 48 h to the treatments. At the end of the second treatment, medium was given to the cells and maintained for an additional 48 h. Triton X-100 (0.1%) was then added as positive control.

Figure 55. Electrical a) impedance, b) resistance and c) capacitance of the HePG2 cells monolayer. After a recovery period of 12 days, cells were re-exposed for others 48 h to the treatments. At the end of the second treatment, medium was given to the cells and maintained for an additional 48 h. Triton X-100 (0.1%) was then added as positive control.

Figure 56. Electrical resistance. Differentiated Caco-2 were exposed to PC, PET1 or PET2 dispersants for 48 h. At the end of each treatment, the medium was given to the cells and then the recovery period is also analyzed. Valinomycin was used as a positive control. $NaCrO_4$ was then added as a second positive control to conclude the experiment.

Figure 57. Representative images of HePG2 cells incubated with 10 µg/mL of the three different NPs for 48 h and stained with phalloidin (Alexa 488, F-actin green staining) and Hoechst 33258 (DAPI, nuclei blue staining). Scale bar is represented 20 µm.

Figure 58. Representative images of Caco-2 cells incubated with 10 µg/mL of the three different NPs for 48 h and stained with phalloidin (Alexa 488, F-actin green staining) and Hoechst 33258 (DAPI, nuclei blue staining). Scale bar is represented 20 µm.

List of tables

Table 1. Identification of each physical processes show in the **Figure 1.**

Table 2. Overview on some currently discussed definitions of MPs and NPs.

Table 3. Intrinsic properties of PET, PC and PVC polymers.

Table 4. The concentration of the ablated product for different ablation irradiation F.

Table 5. Assignment of the Raman modes for pristine PC and post-ablated PC at F=2.8 J/cm^2.

Table 6. Percentage of respective elemental composition of survey spectra.

Table 7. Percentage of the areas of the deconvolution curves of the C1s spectra for the PC NPs, PC pristine films and PC ablated areas of the films. The C_2F_4 signal is attributed to Teflon substrate.

Table 8. Intermediates by the PC photo-degradation identified by Shi et al., 2021 [8], but not available to buy for the NMR analysis.

Table 9.Percentage of respective elemental composition of survey spectra for the three types of NPs. F and Na signals are attributed to fluorine and sodium respectively.

Table 10. Percentage of the corresponding deconvolutions of the C1s spectra. The C_2F_4 signal is attributed to Teflon substrate.

Table 11. The table reports EC_{50} values (µg/mL) of PC, PET1 and PET2 NPs for HePG2 and Caco-2 cells at 24 or 48 h of exposure.

Research Design

Motivation background and objectives

The research described in this doctoral thesis is focused on the investigation of plastic particles as emerging water pollutants. Plastic dispersed in the marine environment degrades creating smaller pieces in the form of micro, submicron and nanofragments. The size of plastic items plays an important role when it comes to their fate. In fact, MPs, sub-micron and NPs may impact the base of the ocean food chain causing possible damage to the entire trophic chain. The lack of studies on the effect of plastic particles on the living organisms and on the human health is due to the limited information related to the characterization and quantification of MPs and NPs [9–13]. The currently available analytical techniques are still lagging behind the urgent need to characterize particles with sizes <100 nm, although there have been some recent advancements in the fields of correlative microscopy and Raman imaging [14–16]. Nonetheless, recent results indicate that NPs research has grown substantially from 6 publications per year in 2004 to 272 publications in 2020 [17], with a priority research area on environmental science and ecology [17]. Instead, a low number of work dealing with the biological effects of NPs has been identified [10], underlining the current lack of knowledge in this field. Mostly of the researches on this field are based on engineered bead models of polystyrene, a limited model which extremely differs from NPs deriving from environmental degradation of plastics. This study offers the possibility to fabricate diverse types of NPs and sub-micron plastic particles that can be used for the realistic investigation of their interactions with biological systems, ranging from cells to organisms, but also with other pollutants. Therefore, part of the studies of the present thesis was focused on the use of a top-down approach to fabricate NPs and sub-micron plastics, namely the laser ablation approach, previously developed to obtain PET NPs [18]. In this thesis, we expand its use to develop different types of plastic particles. With this strategy, it is aimed at the formation of plastic particles directly as a result of the light-matter interaction, rather than the production of nanoparticles by polymerization, and this is closer to the real pathway of the environmental formation of these pollutants. The scope is to minimize the utilization of any additional components, such as surfactants or precursors, to better assess the behavior of NPs in the various media and the interaction with other environmental contaminants [19]. Subsequently, were performed toxicological evaluations, using different alternative biological methods in order to provide a deep understanding of the biological impact of the fabricated NPs. To do so polyethylene terephthalate (PET), polycarbonate (PC) and polyvinyl chloride (PVC) NPs were fabricated that have been selected due to their large use in several consumer goods sectors as in the food packaging industry, beverage bottles' production, construction and electronic applications [1].

The specific objectives of the thesis are:

- The study of the experimental parameters in order to effectively synthesize NPs starting from different polymeric materials using the laser ablation approach

- To produce a “realistic model” of PC sub-micron and nano particles.
- Assess the impact of different typologies of NPs on *in vitro* human cells using different toxicological methods.

Outline of the thesis

The thesis is structured into one chapter focusing on the introduction to the plastic particles as emerging pollutants, three chapters that provide the experimental results, and a final chapter conclusion. The first chapter of the experimental results, is composed of the study of the laser ablation approach as a method for the development of submicron and NPs model particles, the second is dedicated to the chemical and physical characterization of the material produced, and to their biological evaluation. The third section is dedicated to the toxicological assessment of three different types of NP models by means of a combination of different in vitro methods. Apart from the introduction and conclusion chapter, each central chapter consists of an introduction that collects the state of the art and the main concepts of the research developed, the description of the experimental procedures, and the presentation and discussion of the obtained results. In particular:

Chapter 1 gives an overview of the origin of plastic pollution, the development of MPs and NPs, and their known and possible effects on the ecosystem and environment.

Chapter 2 presents the development of models of NPs of different nature. The details of the application of the laser ablation technique for the synthesis of PC and PVC particles are described.

Chapter 3 is mainly dedicated on the PC particle models. Characterization in terms of chemical composition, size distribution, surface chemical analysis of different laser ablation products and particles are presented. In addition, the biological evaluation of NPs hepatotoxicity was investigated *in vitro*, with the second-generation upcyte® hepatocytes used as human hepatic cell model.

Chapter 4 illustrates the toxicological evaluation of three different types of NPs on two different cell lines, the Caco-2 and HepG2 cells, as models of the intestinal epithelial barrier and liver respectively, using three different *in vitro* technologies. Two types of laser-ablated NPs (PC and PET) were studied in comparison with PET NPs made by nanoprecipitation.

Final conclusion give a general overview of all the results obtained in the thesis, in which way this work contributed on improvement of the NPs knowledge.

Chapter I

Introduction

Plastic in the environment

Plastics, predominately derived from petrochemicals and, in lower portion, from renewable sources, show diverse and, at the same time, interesting properties that make them a fundamental component of our everyday life [20]. This "plastic dependence", associated with strong consumerism and poor recycling, is leaving its mark on our environment to the point of irreversibly influencing the planet's geology [21], insofar the scientists proposed a new geologic age for the current chronological period: we are living the Plasticene (Age of Plastics) [22]. Plastic is a unique material in terms of its versatility, cost-effectiveness and resistance, these same properties combined with the intensive consumption and rapid disposal of plastic products have caused its accumulation in the environment [23,24]. Due to the last decades increasing evidence of plastic contamination, in the 2014, the United Nations Environment Program (UNEP) identified the plastic pollution in the oceans as one of the top 10 emerging global environmental problems and put a price tag of US $13 billion per annum on its damages to the marine ecosystems [27]. Sea and ocean represent a particularly dynamic ecosystem for plastic debris. Longevity and relatively high buoyancy of this material facilitate long-distance transport from source areas [28]. Environmental plastic debris consists of mixtures of numerous particles with different sizes, densities, and shapes [29] and these characteristics change continuously over time due to several external events [30]. **Figure 1** shows the most relevant physical processes in the ocean, from the littoral zone to the open ocean, summarized in the **Table 1**. Biota has also a large role in moving floating plastic [31], and may also cause fragmentation through biting or grinding occurring during digestion.

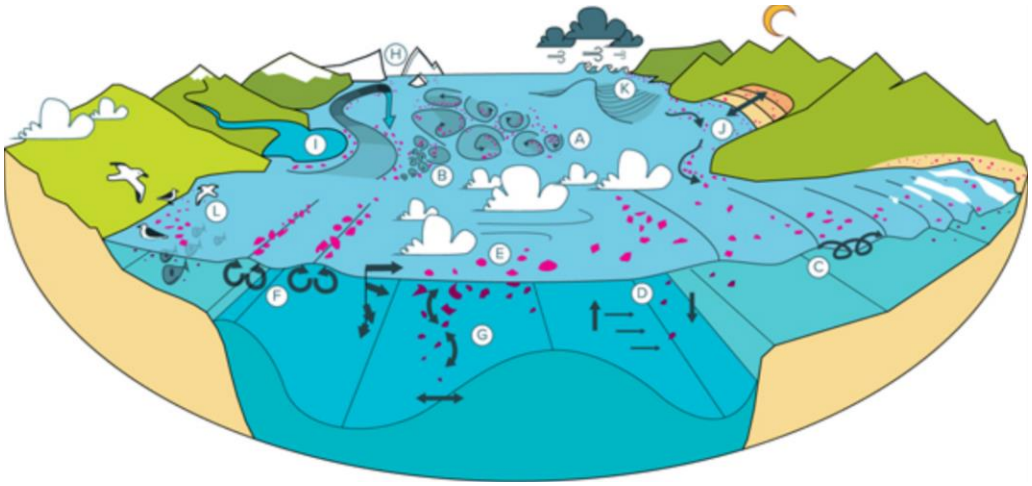

Figure 1. Schematic of the physical processes that affect the transport of plastic (pink items) in the ocean [31].

PHYSICAL PROCESSES	
A	Large-scale open ocean processes
B	Sub mesoscale open ocean processes
C	Open ocean Stokes drift
D	Internal tides
E	Direct wind transport (windage)
F	Langmuir circulation
G	Vertical mixing
H	Ice formation, melting and drift
I	River plumes and coastal fronts
J	Coastal currents, surface waves and beaching
K	Extreme events
L	Transport by biology

Table 1. Identification of each physical processes show in the **Figure 1** [31].

Nowadays, the limitations of the eco-toxicological risk assessment applied to NPs are numerous [32]. The forms of NPs that induce toxic effects, and thus the relevant exposure concentrations, are unknown [33,34]. This happens because the exposure concentrations of small plastic particles formed by the continuous fragmentation of weathering plastic are underestimated. This is due to the scarcity of reliable measurements, especially for smaller particles.

Types of plastics

Plastics are a family of thousands of different polymeric materials with a wide variety of properties designed to meet the needs of each application. The largest market shares belong to low-cost, commodity thermoplastic polymers. From the total plastic produced yearly (in 2020) 30% is PE (HD and LD), 19.7% PP, 9.6% PVC, 8.4% PET followed by other plastic types as shown in **Figure 2** [1]. These plastics are principally made from nonrenewable petrochemicals, so they are derived from fossil oil, natural gas, and coal. Their strength, permeability, porosity, opacity, and color, but mainly their low production and processing costs make plastic particularly attractive [35] and useful in several application fields as shown the **Figure 2**. The basic polymer resins can be adjusted with fillers, and additives to provide many desirable properties such as high strength to weight ratios, durability, barrier capabilities, antimicrobial and UV-resistance at a cost/performance ratio that is difficult to achieve with alternative materials [36]. Packaging, building and construction by far represent the largest end-use markets. The third biggest end-use market is the automotive industry. Other applications includes plastics for furniture, medical applications, machinery and mechanical engineering, technical parts [1]. Nonetheless, such very important properties that make plastics so versatile for humans has also created an emerging threat to the environment as they are widely found as litter in the environment [37].

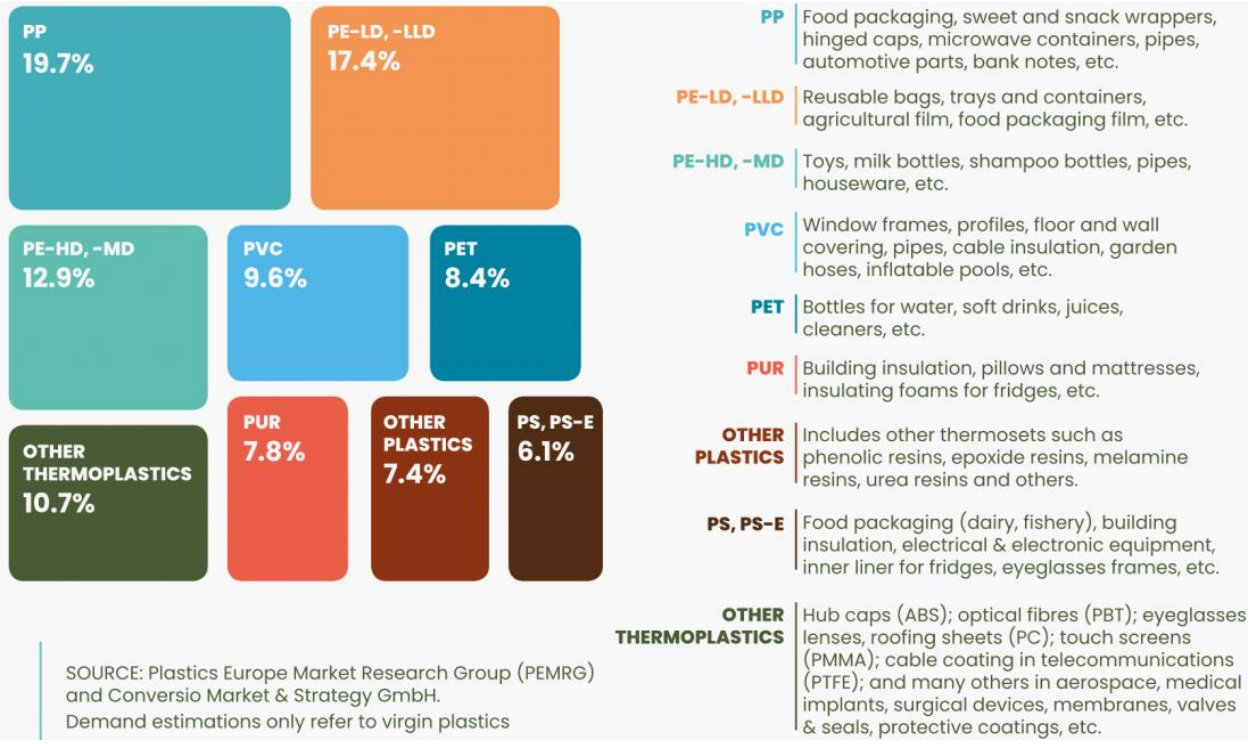

Figure 2. Plastic demand distribution by resin type [1].

Degradation of plastics in water

When plastic is exposed to the environment, its degradation time is estimated to range between few and thousands of years, depended on the plastic type [38,39]. When exposed to the environment plastic is subjected to different weathering processes, such as abiotic and biotic degradation (**Figure 3**). Abiotic factors change the morphology and mechanical properties of both the surface and bulk phase of plastics, as cracking, embrittlement, and flaking may occur. Abiotic factors also affect the plastic at the molecular level. In fact, photo-oxidation, due to the interaction between UV light and plastics in the presence of oxygen, leads to the polymer chain scission, the production of radical and the reduction of the molecular weight, and to the formation of polar functional groups such as carbonyl groups in most polymers [40–42]. As a result the polymers become more brittle and with lower surface hydrophobicity [43]. Specifically, some studies have validated that chain scission reactions induce the formation of products such as long and short-chain alkanes and carbonyl compounds, oligomers, MPs and NPs [44,45]. Furthermore, an increase in crystallinity and brittleness occurs for semi crystalline polymers such as polyethylene as a result of chain scissions, by exposure to high-energy radiation and photo oxidation, in amorphous regions [46,47]. Some typologies of materials (such as PET and PLA) can also undergo thermo-oxidative degradation and hydrolysis, even if extremely slow due to the relatively low environmental temperatures, exposing carboxylic acid and alcohol functional groups and reducing the molecular weight [35,41]. In addition to abiotic processes, plastic exposed to the environment undergoes diverse, co-occurring, and in many cases synergistic biotic weathering

(**Figure 3**). This weathering involves the formation of a biofilm on the surface, mineralization by bacteria, and digestion by marine organisms. After plastic particles enter natural waters, an initial surface layer of microorganisms, organic and inorganic substances is formed, the so-called "eco-corona" [48]. Subsequently a biofilm [49] composed of communities that are phylogenetically distinct from surrounding planktonic communities [50] are formed on the surface of the plastic. The development of biofilms is affected by the polymer type, the surface properties and by diverse external factors such as light, temperature and oxygen conditions, which collectively influence the plastic physicochemical properties [51]. Biofilms favor colonization by sessile organisms, excrete extracellular enzymes that break down the plastic surface, and form extracellular polymeric substances that facilitate aggregation. Biofilms also lead to the alteration of buoyancy, and provide an additional sorption phase for other chemical pollutants. Although biotic degradation pathways are also undoubtedly important, degradation is typically initiated abiotically (light, heat, etc.) [51,52]. Biotic processes often work synergistically with abiotic degradation leading to smaller particles that are subsequently mineralized by microbes. Fragmentation rates increase with a reduction of particle size [30].

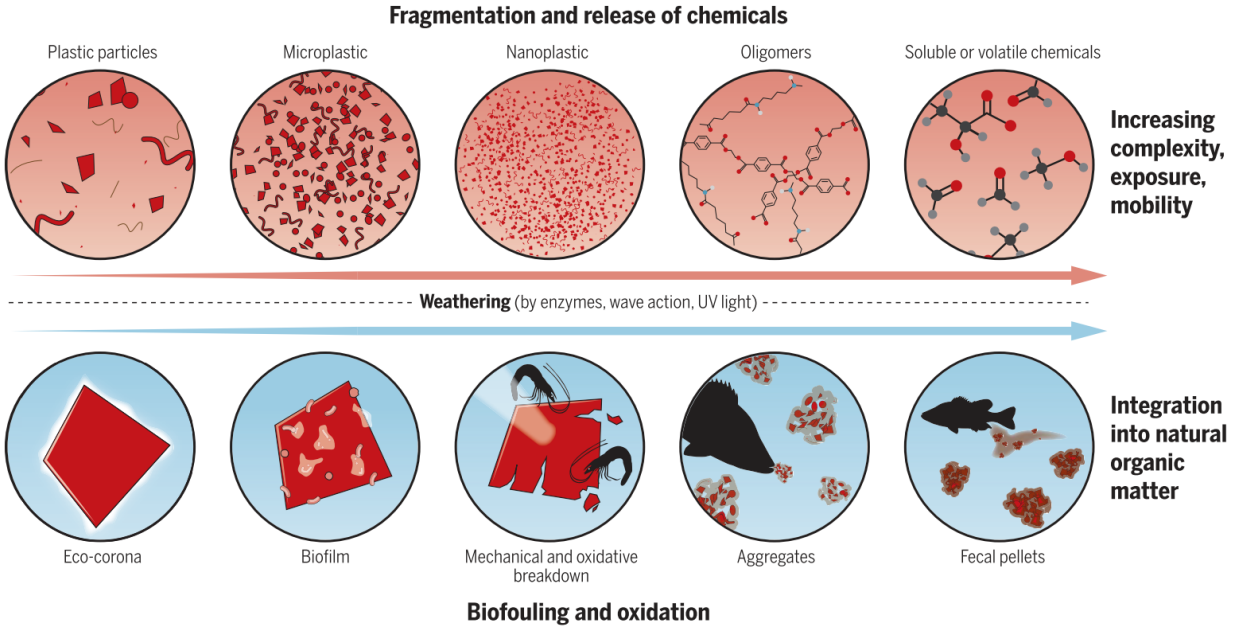

Figure 3. Weathering processes of plastic pollution in the environment. Weathering proceeds along two co-occurring and synergistic pathways: (I) fragmentation and the release of soluble or volatile components (top of the panel); (II) biofouling and oxidative degradation processes (bottom of the panel) [53].

Microplastics and Nanoplastics

Although a number of scientific organizations and regulatory bodies worldwide are increasingly investigating the fate of plastics and monitoring the occurrence of MPs and NPs, there is no formal definition for these small plastic particles [54–56]. Plastic debris can be categorized according

to different properties, such as size, shape, color and origin [54]. Following the definition provided by the European Union (EU) on nanomaterials in 2011, the International Organization for Standardization (ISO) has defined the term nanomaterial as a material with any external dimension, having internal structure or surface structure, ranging from approximately 1 to 100 nm. From this nomenclature point of view, it is intuitive to categorize the plastics based on the conventional units of size. This, however, conflicts with the current terminology. Indeed, ISO defined: nanoplastics (NPs) plastic particles smaller than 1 µm; microplastic (MPs) any solid plastic particle insoluble in water with any dimension between 1 µm and 1 mm; macroplastic any solid plastic particle insoluble in water with any dimension above 5 mm [57]. Aside from size, plastic debris is also commonly categorized on the basis of shape and structure. Frequent descriptors of nanoparticles shape are spheres or beads [54]. But, NPs result from the erosion or breaking down of larger plastic debris and, contrary to manufactured nanomaterials, there are no specific shapes [58]. The term "fragment" is commonly adopted to describe particles with irregular shape. This term, however, implies that these have been formed by fragmentation in the environment, which is not always the case. For instance, abrasives used in cosmetics and personal care are produced as such [59,60] and cannot be distinguished from particles generated by weather fragmentation [54]. Other typologies of possible plastic debris shapes are significantly longer in one dimension (high length-to-diameter ratio) and are commonly (and interchangeably) described as fibers or filaments, with both terms describing thread-like structures [54]. Within toxicology, there is a long-standing tradition of referring to such structures as fibers rather than filaments. For some types of fibers, their aspect ratio has been found to determine toxicological responses, for example, in the case of asbestos and carbon nanotubes. In conclusion, NPs present high polydispersity in physical properties and heterogeneous composition [47,61,62]. **Table 2** shows an overview of the currently used definitions for MPs and NPs proposed by some selected organizations [55].

Organization	Definition of Microplastics (MPs) and Nanoplastics (NPs)
European Food Safety Authority (EFSA)	MPs: Heterogeneous mixture of differently shaped materials referred to as fragments, fibers, spheroids, granules, pellets, flakes or beads, in the range of 0.1–5000 µm (100 nm–5 mm); NPs: Material with any external dimension in the nanoscale or having internal structure or surface structure in the nanoscale (0.001–0.1 µm = 1–100 nm).
European Chemicals Agency (ECHA)	MPs: Consisting of solid polymer-containing particles, to which additives or other substances may have been added, and where ≥ 1% w/w of particles have (i) all dimensions 1 nm ≤ x ≤ 5 mm, or (ii), for fibers, a length of 3 nm ≤ x ≤ 15 mm and length to diameter ratio of >3.
International Standardization Organization (ISO)	Large MPs: Solid plastic particles insoluble in water with any dimension between 1 mm and 5 mm MPs: Solid plastic particles insoluble in water with any dimension between 1 µm and 1000 µm (MP); NPs: plastic particles smaller 1 µm
United Nations (UN)	MPs: Particles in the size range 1 nm to <5 mm.

European Academies	MPs and NPs: Tiny plastic particles of mixed shapes and sizes below 5 mm.
US National Oceanic and Atmospheric Administration	MPs: Any type of plastic fragment that is less than 5 mm in length.

Table 2. Overview on some currently discussed definitions of MPs and NPs [55].

Another distinction can be made by the origin discerning between primary and secondary MPs and both of them might become NPs sources. Primary MPs are originally manufactured to be that size and are widely used in industrial 'scrubbers' used to blast clean surfaces (air blasting), plastic powders used in moulding, microbeads introduced cosmetic formulations as well as spherical or cylindrical virgin resins used during the production of plastic products [63]. Secondary MPs are the predominant form and originate from fragmentation of plastic debris floating in the oceans through prolonged exposure to ultraviolet (UV) light and mechanical abrasion by sand or wave action. They may originate from land-based or sea-based plastic litter sources. Sea-based sources include fishing equipment and sewage from ships. Land-based sources may be single use plastic (e.g. plastic bags) packaging materials, waste from plastic industry etc. [63]. NPs and MPs in natural soils and waters undergo various transformations that will influence their aggregation, deposition, and transport. These processes depend largely on the chemical condition of water (pH and ionic strength), aquifer pore waters, and interactions with the organic matter, microorganisms and other sediments in the water [64]. Aggregation may occur with particles of the same type (homo-aggregation), or between different particles (hetero-aggregation). Moreover, NPs can collide with larger sediments and slow down their precipitation towards the seabed [65]. These behaviors vary also according to the environmental conditions, the density of the polymer and the particle surface chemistry [47,58]. Indeed different types of plastic debris are detected in the environment, such as polystyrene (PS), polypropylene (PP), polyethylene (PE), polyethylene terephthalate (PET), polyvinyl chloride (PVC), and polyamide (PA) [47,64]. Owing to the fact that it is extremely difficult to isolate and identify the type of MPs and NPs from environmental and biological samples, precise numbers about the human exposure towards this type of pollutant have not been determined yet [10].

Trophic transfer and biomagnification of plastic particles

NPs and MPs can be both sources and sinks for other contaminants in the environment. Chemicals including phthalates, bisphenol A (BPA), flame retardants, triclosan, bisphenone, organotins etc. are added during the manufacturing of plastics and these additives may leach from the plastic particles into the environment [66]. The release of such chemical from MPs and NPs is much more efficient compared to the bulk plastics as they have a much larger surface-to-volume ratio and some of them may have a porous and rough surface [67] facilitation the release of the additives. For the same reasons and also due to their modified surface chemistry due to the degradation processes they are subjected to, NPs and MPs are also excellent sorbents of

various pollutants already present in the environment, such as heavy metals, persistent organic pollutants (POPs), antibiotics, and toxic microorganisms [27]. Therefore NPs and MPs can be excellent carries of pollutants, and based on the fact that they may easily pass in the trophic chain they can also act as "trojan-horse" for the internalization of many of these hazardous pollutants [68], which may lead to the biomagnification and bioaccumulation of this "cocktail" of pollutants. Several factors such as the type, size [69], surface charge and concentration [70] of the plastic affect the bioavailability of pollutants. For this reason, the smaller size provokes more concern, NPs can be easier ingested and taken up by a wide range of aquatic biota, but they are more difficult to rapidly excrete from the body through the intestinal tract than MPs. Therefore, the ingestion of NPs and MPs represents an environmental concern for the health of the individual as well as for the trophic transfer of plastic contaminants to larger predators as in the case of transfer from algae, to zooplankton, to fish and humans (**Figure 4**) [71].

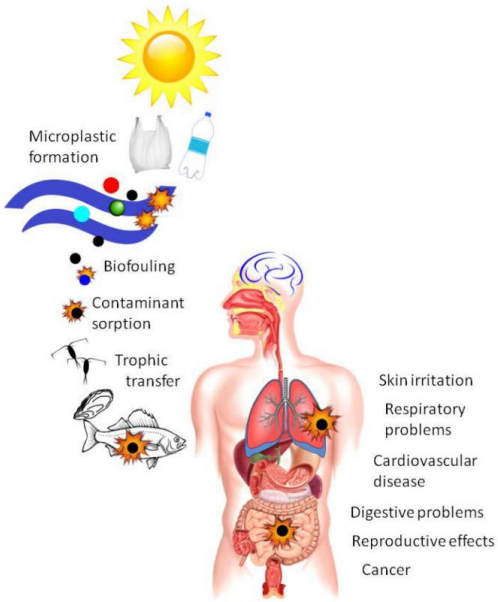

Figure 4. Potential health effects resulting from the bioaccumulation and biomagnification of NPs, MPs and chemical contaminants in the human body [68].

The first study of trophic transfer came about almost a decade after their discovery in sea lion scats. Exposed fish to MPs took twice the time to consume the same amount of zooplankton compared to control fish. Moreover, metabolic effects including weight loss, differences in the triglycerides were also reported [72]. After that, the number of studies on the exposure to MPs in several groups of test organisms increased, testing different typologies of organism. Cole et al. (2013) [73] showed different MPs uptake varying by taxa, life-stage and bead-size. Other invertebrates with a range of feeding strategies, including filter feeders (barnacles), deposit feeders (lugworms) and detritivores (amphipods, sea cucumbers), have been shown to ingest MPs [74,75]. Other studies demonstrated that the ingestion of MPs in marine invertebrates depends also on the particle concentration [76]. Plastic particles found in the scat of fur seals (*Arctocephalus* spp.) were speculated to have been ingested by lantern fish (*Electrona subaspera*), which is

common prey for seals [77]. Fish meal has some use in poultry production and pig rearing, hence MPs may end up in non-marine foods [78]. Moreover, NPs were found to directly absorb through the intestinal wall of mussels [79] and bioaccumulate in barnacles [80]. These findings indicate that this kind of pollutant has the potential to be transferred between trophic levels and raise concerns regarding the bioaccumulation and biomagnification [68,81,82]. The increase in research on this topic led several researchers to investigate the possible plastics content in different food. MPs have been found in mussels, but also in farmed mussels [83]. Moreover, MPs have been reported also in honey, beer and table salt. Honey samples of different origin, mostly from Germany, were found to contain plastic fibers and fragments [84]. MPs were also detected in 24 German beer brands [85]. The same fate in sea salts: MPs fragments and fibers, principally of PET and PE, were the prevalent types of particles detected [63]. Plastic particles have contaminated also vegetables and fruits [86]. Finally, a recent publication has documented that MPs are found also in the feces of human beings, confirming the ingestion of these pollutants by human [87]. Despite the increasing number of works investigating the effects of plastics in aquatic systems, the potential impact of NPs on humans has not been extensively studied yet [88]. Given the enormous complexity of the ecosystem in which they are found, a properly detailed characterization of these pollutants results impossible. Therefore to obtain models closer to reality, it is necessary to reproduce the weathering of the plastic artificially. The next chapter is presented the approach followed in this thesis that allows to obtain NPs models for further studies.

Chapter II

Nanoplastics formed by laser ablation

Abstract

This chapter highlights the use of the laser ablation approach of polymeric material in water as a method for fabrication of NPs of different nature. Experiments focused on PC were carried out with the KrF laser pulse (248 nm). Initially, the investigation of the effect of different irradiation conditions on the etch depth of polymer bulk and ablation products is performed. After that, the formation of PC NPs through the laser ablation of solid PC films in water was demonstrated. The modification of the F affects the size of the produced particles, ranging from the submicrometer to the nanometer range as F increases, and on the amount of the material ablated, increasing the amount of ablated materials as F increases. After that, the characterization and toxicological assessment were focused on the F that forms the whole amount of NPs. In the last part of this work, the analysis and toxicological assessment of dispersants and NPs are also analyzed separately.

State of art

Models of nanoplastics

Research on MPs and especially on NPs has started only recently and thus, there are many unresolved issues. While some information on MPs is available, research data on NPs is virtually non-existent [55]. Therefore, a global effort is necessary to provide basic information about NPs to overcome the large knowledge gap in understanding the effects of this kind of pollutants on human health. The separation and identification of NPs directly by environmental samples are still difficult and it is not possible to collect sufficient samples by the environment to develop standardized characterization studies. Referring to the literature, the NPs models are mainly based on the commercially available particles of PS and PE [17,89], although the reality is widely different [64,86]. Furthermore, in most studies spherical NPs were used. This trend can be partly explained by the fact that most of the manufactured virgin NPs are spherical and NP fibers, or fragments, are generally difficult to produce and control under laboratory conditions [90]. In fact, focusing the attention only on these last three years, several studies are focused on exploring the formation of different types of NP samples. Specifically, Balakrishnan et al. developed a simple method to obtain PE NPs using nanoprecipitation of a PE toluene solution [91]. Rodriguez-Hernandez et al. also used nanoprecipitation to produce PET NPs from fine chips of PET [92]. Pessoni et al. synthesized NPs with different surface functionalities using a soap free emulsion polymerization. These NPs exhibited smooth or raspberry-like surface morphologies, and were monodisperse in size (polydispersity index (PDI) < 0.05) [93]. Focusing on the other types of polymers, Cassano et al. developed a novel synthesis route for Polypropylene (PP) NPs via oil-in-water emulsion precipitation in the presence of the sodium cholate biosurfactant [94]. Mitrano et

al. synthesized metal-doped NPs to be used as tracers [95], whereas Johnson et al. made fluorescent PET NPs [96]. These kind of NPs offer the advantage of being easily detected with accuracy and reliability in complex systems. With these methods, plastic nanostructures with few defects and homogenous chemical composition and size distribution are produced, substantially different from the NPs dispersed in the environment, which have irregular shapes, similar to a fractal structure, and complex surface chemistry, due to the degradation experienced [61]. This indicates the need to explore new procedures for the development of accurate and environmental relevant NPs models. Therefore, to overcome these limitations, recently, various top-down approaches have been explored. In particular, Astner et al. developed a top-down process to produce MPs and NPs through the mechanical degradation of agricultural plastics (mulch films prepared from biodegradable polymer polybutyrate adipate-co-terephthalate and low-density PE) [97]. The mechanical degradation is also performed by El Hadri et al. to obtain fragmented NPs starting from commercially available primary MPs and secondary MPs (collected on beaches) [98]. In this work, the NPs size distribution is very low, but the grinding process includes steps in wet conditions using ethanol as a dispersant. A completely different approach, based only of water as dispersant, is presented by Magri et al. who utilized the laser ablation approach to obtain PET NPs, with size distribution of ca 50 nm, with significant size and shape heterogeneity (compared to the formation on NPs upon polymerization in dispersed media), and weak acid groups at the particle surface [18], confirming to be a fabrication method for a realistic NPs model. Chemical analysis reinforced the validity of this model, since, the chemical properties of the NPs were in accordance with what has been observed in UV-exposed plastic materials in the environment [18]. Considering that laser ablation is validated only for PET NPs, in this thesis this technique is explored for the development of other NP models.

Laser ablation process

Laser is the acronym for “light amplification by stimulated emission of radiation”, a high energy beam of electromagnetic radiation. The initial idea of laser theory was presented by Einstein. However, the first ruby laser was developed in 1960 by the physicist Theodore H. Maiman. Soon after the experimental realization of the laser, lasers were applied in several applications such as in the military, health, industrial and scientific fields. The first widely recognized application of the lasers was the laser printers, which were invented in 1971 by the US engineer Gary Starkweather [99]. Successively, several industries led to the development of novel machining processes such as laser beam milling, laser drilling and laser etching. All of these laser-involving machining operations share a common phenomenon known as laser ablation. Laser ablation is the top-down process of removing material by focusing a laser beam onto a substrate and it may occur in vacuum, air or liquid [100]. Laser ablation was also applied as a method to synthetize nano sized objects [101,102] such as nanoparticles, nanowires and nanotubes directly in suspensions. Specifically, the pulsed laser ablation in liquid-phase (PLAL) describes the process in which nanoparticles are produced by the ablation of a solid bulk target immersed in a liquid using short and intense laser beam pulses. When a focused beam of laser radiation strikes a surface, the electrons present in the bulk target are excited by the laser photons (I). This excitation in liquid

produces a fast phase transition at the target-liquid interface (II). Within a few nanoseconds, the target material undergoes melting and phase explosion leading to a dense plasma (III). The plasma is characterized by high pressure and high temperatures. The interaction between the molten target material, the plasma, and the surrounding liquid along a sharp temperature gradient leads to shockwave and the plume expands in a cavitation bubble (IV), resulting in fast cooling and condensation of the atomized matter into nanoparticles (V) (**Figure 5**). In the last stage the bubble collapses the nanoparticles mix with liquid where can undergo coalescence/aggregation processes (VI) [103]. The ablation process and the properties of the nascent plasma are transient and depend on the applied pulse duration and energy. As **Figure 5** shows, when the pulse length is shortened (femtosecond (fs) laser pulse) energy is more rapidly projected into the target leading to a faster material ejection. Moreover, it is demonstrated that for nanosecond (ns) laser pulses, the energy of the laser photons is used for electronic excitation resulting in direct bond breaking (photo-chemical event) [104,105]. Differently, the electronic excitation is thermalized on a picosecond (ps) timescale that then results in thermal bond breaking (photo-thermal event) [106]. There is even the possibility of having a mixture of both, but it is most adequate for short laser pulses in the ps and fs ranges [107]. Furthermore, PLAL, as already demonstrated in previous studies, favors the heat exchange between the ejected material and the surrounding aqueous medium, decreasing the thermal effect on the polymer [108,109].

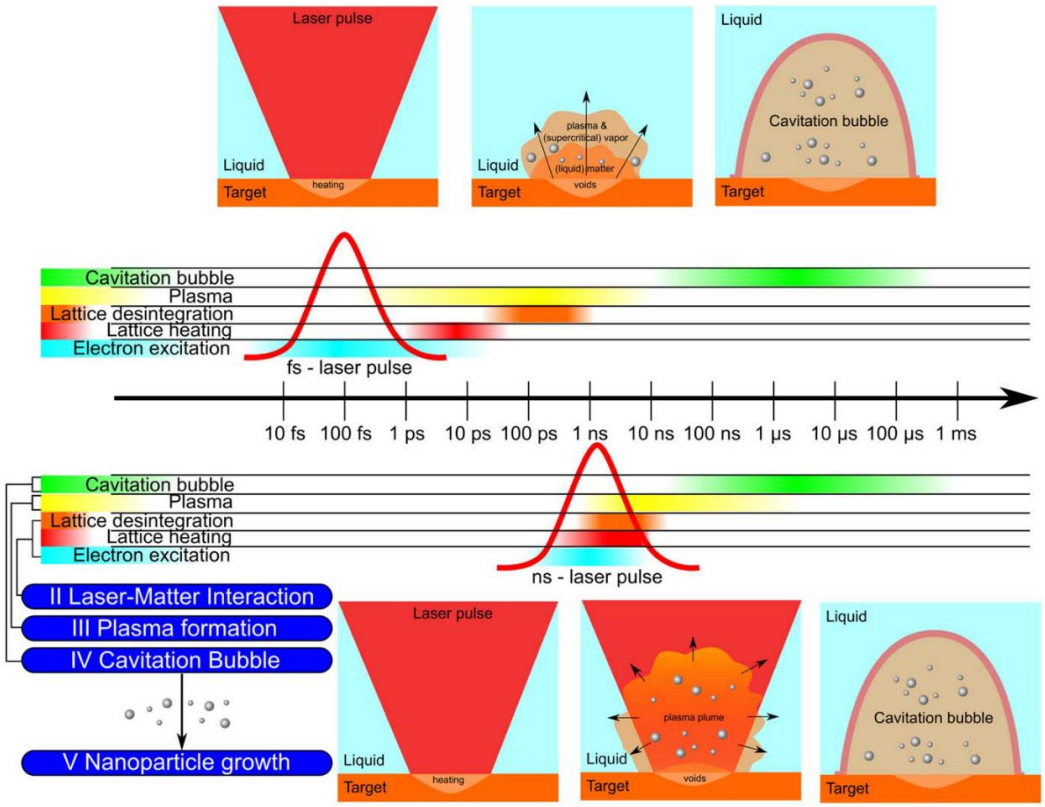

Figure 5. Schematics of the laser ablation process at different timescales. The time frame gives insight into the different characteristic times of the main physical process in laser ablation in

liquid-phase for femtosecond and nanosecond laser pulses: energy transfer from the laser-excited electron gas to the lattice (a few ps, light blue and red lines), phase transition of the target (above 100 ps, orange line), plasma lifetime (a few μs, yellow line), and bubble lifetime (a few hundreds of microseconds, green line). Each process is included in specific phase listed in the blue elliptic boxes on the left [103].

The ablation occurs above a specific threshold fluence that is the total energy of the laser pulse per unit area [J/cm^2]. This parameter changes on the basis of the type of target and of the surrounding environment (liquid, vacuum or air). PLAL has been largely applied for the synthesis of inorganic nanomaterials (such as metals, semiconductors and ceramics), expanding its application also on polymeric nanoparticles [108,109], because there is the possibility to control size and polydispersity of the produced samples, as a function of the irradiation fluence, wavelength, and pulse number. Furthermore, the laser ablation in water is a green fabrication technique which offers the possibility to produce nanoparticles without the use of chemical reagents or compounds. Based on all these information, Magrì et al. have studied and demonstrated that PLAL can be used for the fabrication of environmental relevant NPs [18] with characteristics similar as the ones of the NPs expected to be present in the environment and formed by plastic degradation. The light-matter interaction that occurs during the ablation process is the laboratory scale-down that happens in the marine environment with the interaction between the sunrays and the plastic waste in the sea. Considering, the difficult characterization of the NPs from the environment, it is not possible a comparison, but following the photo-degradation pathway for the polymer photo-degradation and the chemical characterization shown in the next chapter, it is possible to suppose the same reactions that occur during the photo-degrade reaction may occur in the ablation process.

Polymer materials

Since its discovery, laser polymer processing has become an important field of applied and fundamental research. Most of the studies on the PLA on polymers are focused on the study of the polymer surface with mainly application on the fabrication of micro-optical devices and microfluidic channels [107]. Considering that PLA is affected also by the material properties, not only by laser parameters, the type of the polymer is fundamental for the ablation process. Polymers with a high absorption coefficient and low thermal conductivity have some advantages for ablation, such as the reduced thermal load in the bulk of the polymer and the development of high temperatures at the laser-polymer interaction zone [110]. Also the decomposition mechanism of the material is an important aspect. They can either depolymerize upon irradiation, for example, poly-methyl-methacrylate, or decompose into fragments such as polyimides or polycarbonates [107]. Herein, in contrary to the so far studies on the ablation of polymers that are focused on ablated surface, it is presented the PLAL as a valuable tool to produce NPs coming from different types of polymers. Starting from the previous work on PET NPs [18], the methodology was further modified in order to fabricate PC and PVC particles. As PET, also PC has been chosen due to its large diffusion in several sectors as in the food packaging

industry, for bottles' production, in building, construction and electronic applications [1] and therefore due to the higher possibility to be found exposed in the environment as plastic litter. In fact, PET and PC MPs have been not only detected in the environment [111], but also in the food [112] and in some meconium samples and in human stool specimens [113]. PET and PC are thermoplastic polymers, chemically and thermally stable, strong and durable. The combination of intrinsic properties (**Table 3**) make PET and PC easily manageable and suitable for their wide range of application. The presence of aromatic rings (**Figure 6**) in their repeating units makes these polymers materials with notable stiffness and strength and great ability to absorb UV light. The rigidity of the PC is also conferred by its carbonate esters with planar (−O−(C=O)−O−) cores. As for the PVC, it is one of the third most widely produced synthetic polymers, after polyethylene and polypropylene (**Figure 2**). There are two forms of PVC, the rigid form used in construction applications, in packaging and in plastic cards. The soft form, formed upon the addition of plasticizers, is used as imitation leather, for rubber replacement and several others.

	PET	**PC**	**PVC**
Density (g cm^{-3})	1.300 - 1.400	1.200	1.400
Refractive index	1.580-1.640	1.584–1.586	1.540
Thermal conductivity ($Wm^{-1}K^{-1}$) at 23°C	0.15 - 0.40	0.19 - 0.22	0.12 - 0.25
Water absorption - over 24 hours (%)	0.100	0.100	0.030 - 0.400

Table 3. Intrinsic properties of PET, PC and PVC polymers [114,115].

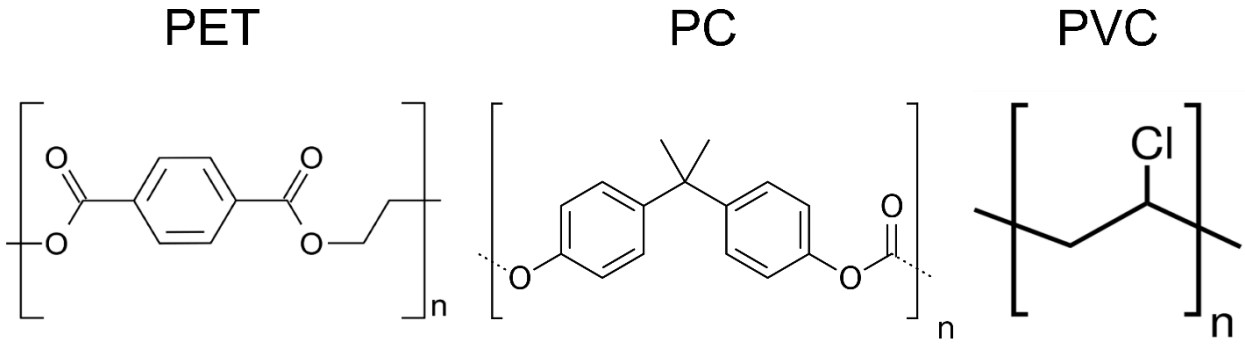

Figure 6. PET, PC and PVC molecular structure.

In this chapter, it is presented the formation of PC particles upon the PLAL of a solid PC film immersed in water. It is proved that the laser irradiation conditions affect the size of the produced PC particles which ranges from the submicron to the nanosize range. The same approach is used also on PVC film and preliminary results on the irradiation conditions to obtain particles in the nano-size range are presented.

Materials and Methods

Laser ablation process

The polymeric films (Goodfellow Cambridge Ltd.), immersed in 8 ml of Milli-Q® water, were exposed to a laser irradiation using a KrF excimer laser (Coherent-CompexPro 110, wavelength: 248 nm, pulse duration: 20 ns, repetition rate: 10 Hz, number of pulses: 50) coupled with a micromachining apparatus (Optec-MicroMaster). Initially a systematic study on the irradiation of a single spot of 4 cm^2, with different fluences (F) was performed in order to define the ablation conditions. F is varied by attenuator (A), voltage (V) and demagnification (D). F (J/cm^2) is calculated using equation (1), where energy (J) is the energy of the laser beam:

$$F = \frac{Energy}{3.6} \times D^2 \times \frac{A}{100} \quad (1)$$

Subsequently, after defining the ideal irradiation parameters for an optimized ablation process, three different irradiation F are used (2.8 J/cm^2, 2.1 J/cm^2, 0.9 J/cm^2) to investigate the effect of the laser F to the PC ablation product. To obtain the PC NPs fraction of the laser ablation product with F of 2.8 J/cm^2, the ablation products were filtered (Cellulose Acetate, Ø = 0.22 µm, Millipore), collected and concentrated by a Rotavapor treatment at 45°C to obtain particle dispersions with defined concentrations (0.600-0.300 µg/ml).

Profilometer analysis

Each spot on the PC films formed upon laser irradiation of different conditions was analyzed by 3D Optical Profilometry. Different magnifications, ranging from 2.5× to 20×, were used corresponding to a Z profile resolution ranging from 25.0 µm to 0.5 µm respectively [116]. The data were collected and analyzed by Origin Pro version (2018), used also for data representation.

Dynamic Light Scattering (DLS)

The analyses of the hydrodynamic diameter (D_H) by Dynamic Light Scattering (DLS) were performed using a Zetasizer Nano ZS spectometer (Malvern Instruments, United Kingdom). Size distribution is analyzed on the laser ablation products at different F, 1 ml of the sample is analyzed. Size distribution results were expressed as average of three consecutive measurements, carried out at 25 °C. The data were collected and analyzed by Origin Pro version (2018), used also for data representation.

NPs quantification

To evaluate the NPs amount produced after the ablation process, in terms of mg/mL, the weight of PC ablation product previously concentrated by a Rotavapor treatment at 45°C was quantified by means of thermogravimetric analysis (TGA) (Q500, TA Instruments). Measurements were performed adding drop by drop (50 µl) the PC suspension on the balance. The weight of the solid ablation product present in the sample was then defined after subjecting it in an isothermal ramp under inert N_2 atmosphere (flow rate of 50 mL/min) at 100°C in order to permit to the water to evaporate. As will be discussed below, this was an important step in order to define the

concentration of the solution, and then to use it in order to construct a method for the definition of the concentrations of the other PC ablation products through the UV-vis absorption spectrum analysis (Cary 6000i, Varian).

Results and Discussion

Laser ablation on PC

PC films were used as targets for the laser ablation process, and the ablation products after different F were analyzed. Initially, the study has been focused on the irradiation conditions useful to have a successful ablation process on the PC substrate The performance of the laser ablation under different irradiation conditions is indirectly estimated by the measuring the etch depth of the irradiation spot on the polymer by the profilometer. As **Figure 7** shown, as the irradiation F increases also the etch depth increases with the higher etch depth to occur at F of 2.89 J/cm^2. This event occurs also in other different polymer and no-polymer materials as previously demonstrated [110,117,118]. The material removal is linked to the F and pulse duration and is based on polymer degradation kinetics for random scission, depolymerization, and mending of main chain links [103,119].

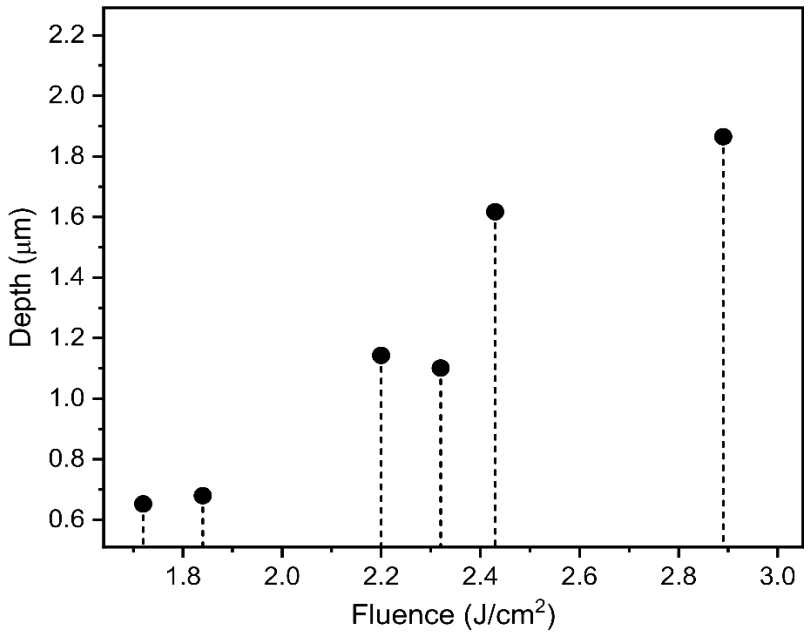

Figure 7. The trend of ablation depth as a function of the laser F for PC at different irradiation conditions.

Therefore for a higher ablation productivity, and therefore for a higher amount of etched material, the PC polymer target should be irradiated with F of c.a. 2.89 ± 0.10 J/cm^2. To further explore the ablation process for the production of PC NPs, the attention was focused on the investigation of the laser ablation product using DLS. In fact as previously discussed, the shockwave produced from the laser irradiation causes the ejection of solid matter from the

polymer surface in the surrounding water. As shown in **Figure 8**, the ablation product after the irradiation of the PC substrate with F 2.80 ± 0.03 J/cm^2 and 50 pulses, contains particles with a hydrodynamic diameter (D_H) of 110 ± 16 nm. Lower irradiation F (2.06 ± 0.05 J/cm^2) results in the production of bigger particles as most of them are in the submicron range with a maximum D_H value of around 410 ± 25 nm, while there is also a small amount in the nanosize range (D_H c.a. 90 ± 10 nm). Lower irradiation F (0.94 ± 0.04 J/cm^2) results in the formation of even bigger particles in the submicron range, at around 710 ± 100 nm. Therefore, it is proved the direct dependence of the irradiation F to the particles size formed and that higher F value results in smaller particles in the nanometer range. In fact, during ablation the photons of specific energy and surface density are interacting with the PC polymer substrate, resulting to the fragmentation of the polymer in small pieces which are ejected and dispersed in the liquid environment [107]. The variation of the fragments' size is directly related to the F of the system. The higher the F, more are the photons that interact with the polymer surface and therefore more violent the breakdown and fragmentation of the polymer layer is, resulting to the formation of smaller polymer pieces.

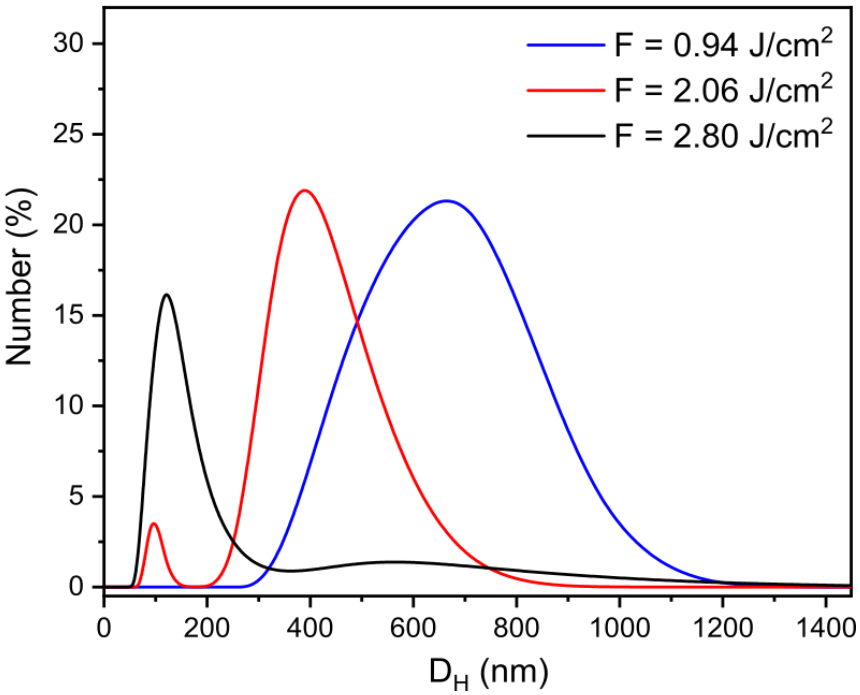

Figure 8. Hydrodynamic diameter (D_H) distribution of PC particles synthetized at three different F.

Concerning the laser irradiation of the PVC films, as **Figure 9 a** shows, the particles size decreases as the irradiation F increases. In this case, to form PVC NPs the PVC films should be irradiated with F 4.5 J/cm^2 (**Figure 9 b**).

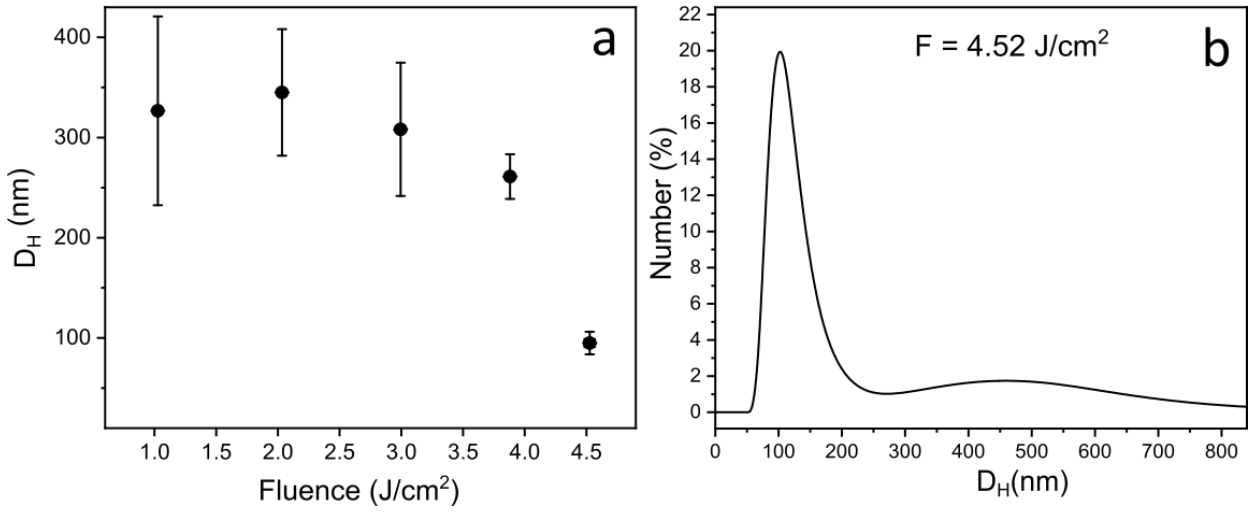

Figure 9. (a) The trend of D_H of the PVC ablation product as a function of the irradiation F; (b) Hydrodynamic diameter (D_H) distribution of particles synthetized at F 4.52 ± 0.04 J/cm^2.

The quantification of the formed PC particles was performed in order to define the concentration of the ablation products. To do so, the calibration curve, shown in the **Figure 10**, was constructed by monitoring the absorption intensity of the peak at 278 nm of the UV-Visible absorption spectra of the PC dispersions of known concentrations obtained by of different dilutions of a starting stock solution of 0.917 mg/ml (concentration defined by the TGA analysis).

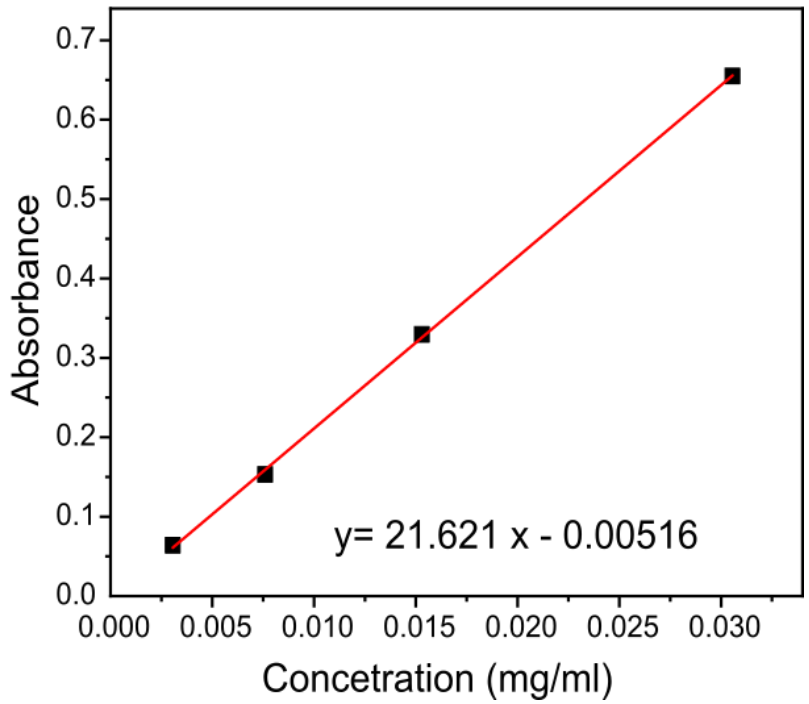

Figure 10. Calibration curve of PC ablation product to define the concentration.

By the linear fitting of the obtained points, the equation that gives the dependence of the absorption intensity at 278 nm to the concentration was obtained, making possible the measurement of unknown concentrations of the ablated products by simply monitoring the UV Vis absorption spectra. The absorption edge of the UV vis spectra of dissolved PC pristine lies in the 200–300 nm region, as the pristine PC spectrum shows in the **Figure 11 a**. These absorption bands in that range are associated to the π - π* electronic transition [120,121] in the aromatic compounds. This transition is very sensitive to the change in the environment around the phenyl ring. This in turn results in the formation of double/triple bonds, conjugation of bonds [122], formation of carbon clusters [123] etc. As shown in **Figure 11 b** and **Table 4** the ablation product amount decreases with the decrease of irradiation F confirming previously presented results on the etch depth (**Figure 7**). The increase of the absorption edge in the UV spectrum with increasing irradiation dose indicates the increased ablated material in the films as the F is increased.

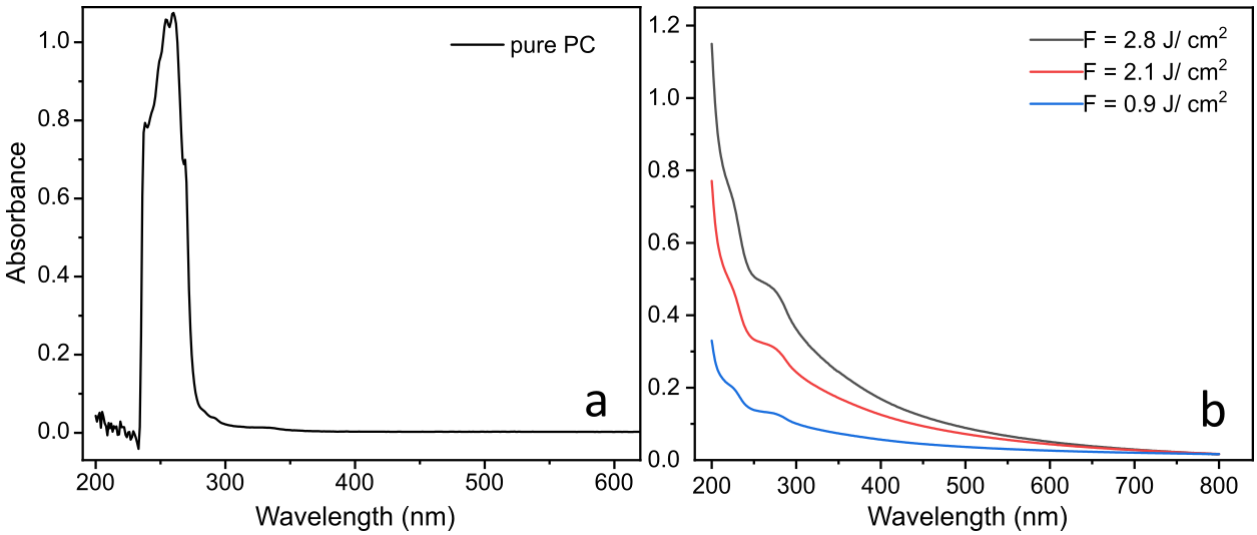

Figure 11. UV-Vis absorption spectrum of (a) the pristine PC film and (b) the ablation products at different F.

F (J/cm^2)	Concentration (µg/mL)
0.94	6.0540 ± 0.0017
2.06	16.0660 ± 0.0025
2.80	24.5380 ± 0.0012

Table 4. The concentration of the ablated product for different ablation irradiation F.

Based on the fact that in the aim of this thesis is to explore the biological fate of NPs, the ablation product obtained by F 2.80 J/cm^2 filtered using a filter with a cutoff of 200 nm, in order to decrease the polydispersity of the NPs size (**Figure 12**). After the filtration, each ablation cycle had a yield of 5.900 ± 0.001 µg/mL of NPs.

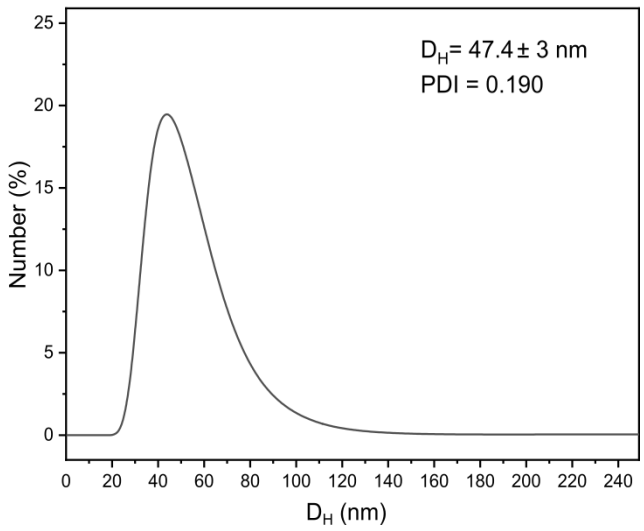

Figure 12. Hydrodynamic diameter (D_H) distribution of PC NPs after filtration and concentration.

Conclusions

The incessant development of technologies for the fabrication of different types of NPs did not still reach the objective of providing NPs with sizes smaller than 100 nm, with properties similar to what would be expected to be found in the environment after the degradation of larger plastic fragments. In this regard, a model that faithfully mimics a real NPs sample has been developed through laser ablation in water, with the advantage of producing nanoparticles without impurities, chemical precursors, and their byproducts. This chapter explores the laser irradiation conditions of PC and PVC solid targets and defines the effect of the different irradiation F on the size and quantity of the fragments produced during ablation. In the next chapters, the physicochemical characterization of the PC NPs (formed upon irradiation at F 2.80 J/cm^2) and the toxicological assessment is performed, while the submicron-particles obtained at F 0.94 J/cm^2 have been partially characterized.

Chapter III

Characterization and toxicological assessment of PC NPs

Abstract

This chapter is focused on the physicochemical characterization and toxicological assessment of PC particles synthetize through laser ablation. Focusing on NPs of the smallest size range, a detailed chemical characterization proves that the produced particles are composed of PC, while their surface is highly oxidized, in accordance with the PC fragments deriving from natural photo-degradation processes. Furthermore, the molecular components released in the water during the fabrication process are similar as the ones of the components released during the photo-degradation of the environmentally exposed plastic. Such realistic mixture of the photo-degradation products of PC, namely PC NPs and other by-products, makes possible the risk assessment evaluation on the biological effects of the PC based plastic litter to human health. Considering the human liver as a secondary organ of exposure, the impact of the PC NPs and dispersant are evaluated *in vitro*, using upcyte® hepatocytes as a human liver cell model. The **Figure 13** shows the representation of the different components of the ablation product.

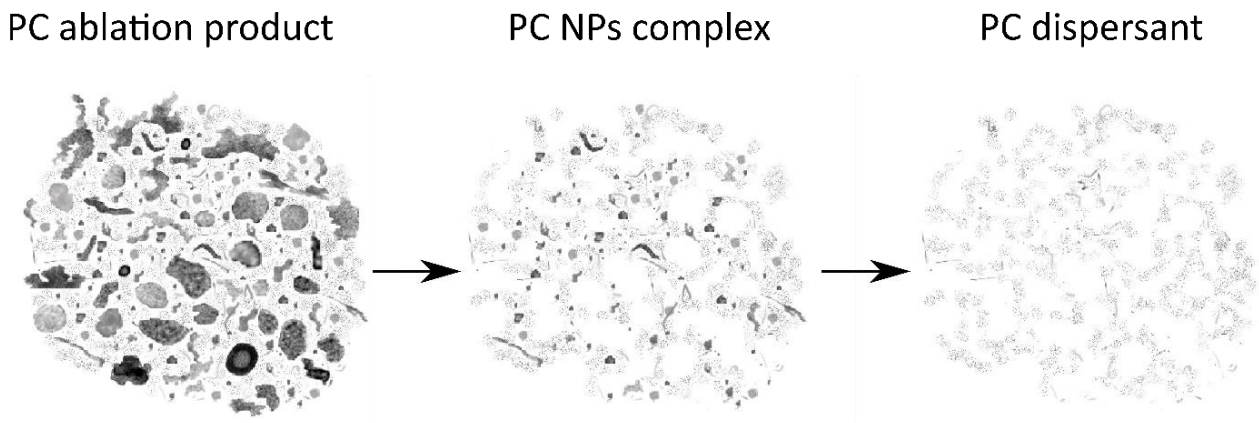

Figure 13. Representation of the different components of the laser ablation products, then the PC NPs after a first filtration and concentration and the dispersant after the ultrafiltration with the 30kD Amicon filter.

State of art

NPs generation from plastics

As shown in previous chapters, plastic wastes are subject to various weathering processes. The generation of NPs through fragmentation of MPs and larger pieces of plastic debris in the marine environment is a process that depends on numerous factors, as well as characteristics inherent to the nature of the degrading material, including molecular weight distribution and the presence of additives. It is essential to estimate the fragmentation rates of the plastics present in the marine environment to develop reliable models. The fragmentation rates cannot be described by classical chemical kinetics in a general way for all types of plastics. Based on the typology of polymer, different reactions occur in the presence of the UV Vis rays and oxygen [42]. The formation of NPs by the weathering or aging of macroplastics and MPs leads to the release of various chemicals, additives, polymeric fragments, and ultrafine particles (e.g., NPs) [53]. Thus, it is essential to understand the degradation processes of plastic particles to increase our understanding of the source of NPs and evaluate the potential environmental hazards to organisms. Several studies regarding the degradation of plastics have been conducted under outdoor conditions or accelerated weathering conditions investigations on the characterization of different typologies of MPs after UV exposure [8,40,124]. Their results show the UV ray tended to modify the surface of the particles as the photoreaction proceeded with an increase of oxygenated functional groups and an increase in the polydispersity index [8,40]. The study of the polymer photo-degradation mechanism in the aquatic environment allows having the information on the chemistry of the NPs that are expected from the environment. Focusing on the PC, in the next paragraph, there is an overview of the PC chemistry after the photo-degradation of the material that gives an idea of which types of chemical groups or byproducts might be present after the PC irradiation.

Photo-degradation pathways of polycarbonate

The chemistry underlying the PC photo-degradation has been ascribed to two different mechanisms: photo-Fries rearrangement (**Figure 14**) and photo-oxidation (**Figure 15**). The relative importance of these mechanisms depends on the wavelengths of the light that cause the degradation process. Lemaire et al. [125] illustrated that the photo-Fries rearrangement reaction is more likely to occur when light with wavelengths shorter than 300 nm is used, whereas photo-oxidation reactions are more important when the light of longer wavelengths (>340 nm) is used. Taking into account that the spectral composition of the natural sunlight spectrum ranges between 100 nm and 2 mm, with the ultraviolet radiation to account for less than 4%, while the visible light (wavelength >400 nm) to constitute around 43% of the solar energy [126], there is a possibility that both reactions take place under outdoor exposures. The photo-Fries rearrangement reaction is a photolytic reaction occurring when the polymer absorbs the irradiated wavelengths. This reaction causes the scission of the carbonate linkage in PC, forming two primary free radicals [127,128]. Fries rearrangement and crosslinking of these free radicals result in the formation of phenyl salicylates, dihydroxybenzophenones, and substances, such as

dihydroxybiphenyl and hydroxydiphenylether. Further ‘‘rearrangement’’ of these groups yields substances, such as ortho-dihydroxy-benzophenone or diphenoquinone, which absorb in the blue range, and are responsible for the yellowing observed in photodegraded samples [128,129]. The products formed during photo-Fries reactions can also undergo photo-oxidation, yielding secondary and tertiary products of lower molecular weight [130]. The photo-oxidation reaction is initiated with radicals formed by irradiation. The photo-oxidation mechanism proceeds through three routes: side chain oxidation, ring oxidation and ring attack [131]. In the side chain reaction, UV radiation is absorbed by the polymer, and, as a result of the energy excitation, hydrogen atoms are abstracted from the methyl groups, forming free radicals, which abstract hydrogen from neighboring molecules yielding new free radicals. In the presence of oxygen, the methyl side chains are photo-oxidized into hydroperoxide intermediates, and the reaction can either propagate or terminate yielding tertiary alcohols and ketones. Photo-oxidation of the aromatic rings yields polyconjugated species. The empirical formulas obtained for many of these products indicate the presence of a high degree of reactive unsaturated groups that could be easily oxidized to colored products [131]. This reaction is considered the main cause of yellowing in PC [131]. Chain scission is favored over ring oxidation, particularly near polymer chain ends, yielding phenolic end groups and reducing the molecular weight. Chain scission forms polar groups that favor hydrolysis and releases monomers and oligomers that offer less resistance to oxidation compared to the original PC units [132].

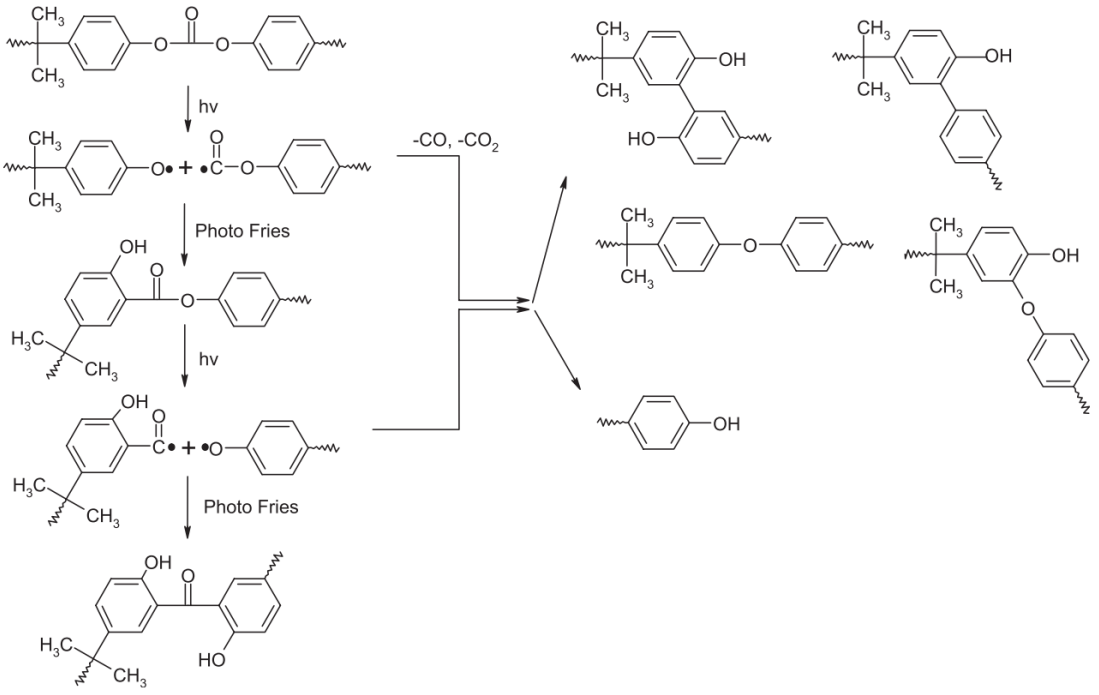

Figure 14. Photo-Fries rearrangement via the radical process [127].

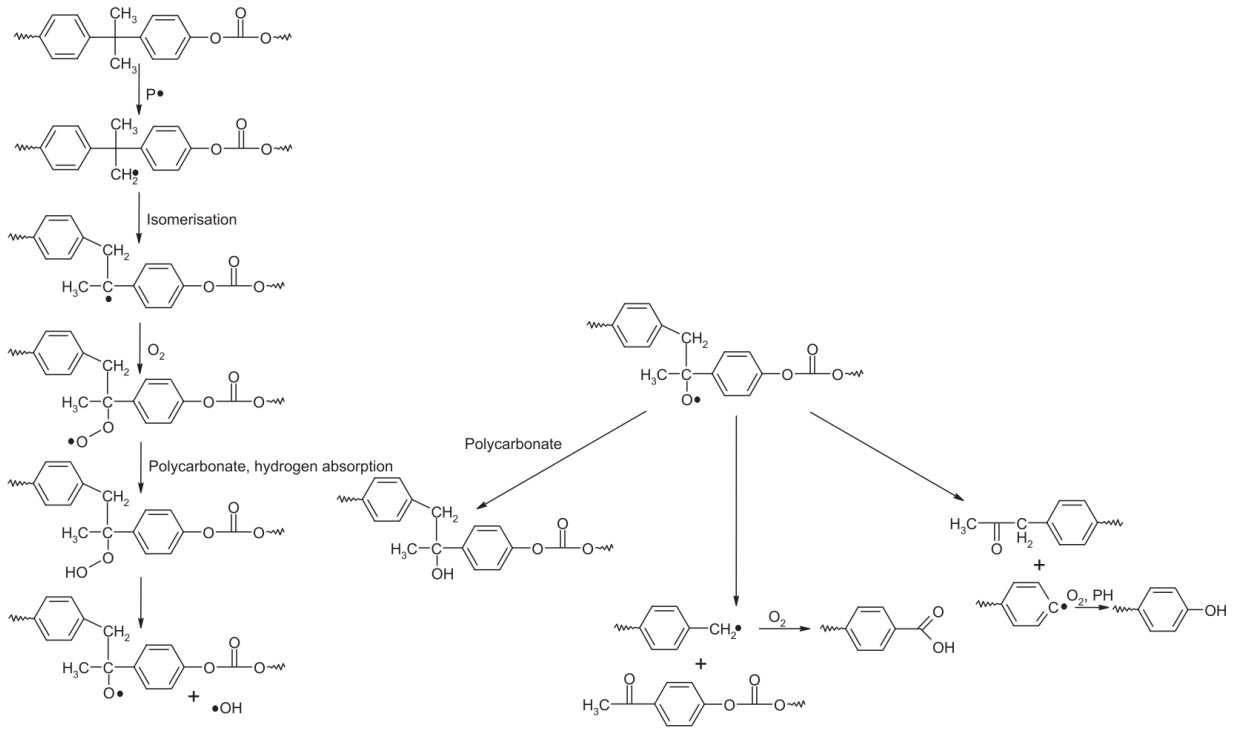

Figure 15. Photo-oxidation of polycarbonate [127].

As extensively discussed in the previous chapters, plastic waste in the form of macroplastics, mesoplastics or even in the form of smaller plastic fragments (MPs) can be subjected to various weathering processes, and several studies have focused their interest on the investigation of such processes. Concerning PC, in the recent study [8] it has been investigated the photo-aging behavior of PC MPs in aquatic environments under UV light irradiation. Their results show that the light exposed MP surfaces tended to become smooth as the photoreaction proceeds with an increase of oxygenated functional groups on the surface. Furthermore, they detect an increase of PDI, and a decrease of the molecular weight distribution. On the top, as a result of the depolymerization and photo-oxidation processes occurred, it has been observed the release of a small portion of BPA and a greater amount of other low-molecular weight intermediates (e.g., hydroxylation, carbonylation and carboxylation products) which also contribute to the toxicity of the system and to the potential estrogenic activity, emphasizing the integral cumulative toxicity of the photo-aged plastic debris [8].

Hepatotoxicity of nanoplastics

The non-biodegradability and, therefore, the long life of most of the current types of plastic makes the MPs and NPs presence to persist for very long time in the soil and water, making possible their entrance in the ocean food chain, which as demonstrated may cause potential damage to the entire trophic chain, including humans [48,133–135]. Despite the increasing number of studies investigating the effects of MPs and NPs in aquatic systems [136,137], the potential impact of NPs on humans has not been extensively studied yet [88]. Dermal absorption, inhalation, or

ingestion represent the main routes of human exposure to NPs [63,88,134], which they may arrive via the bloodstream to the liver and accumulate there. Human liver has a central role in detoxifying the body from xenobiotics/toxicants and, thus, the accumulation of MPs or NPs in the liver can be plausible. This scenario has been demonstrated by several studies: polystyrene nanospheres (50 and 100 nm) were found in the liver of rats after ingestion [138] and NPs from different materials are found in the liver of fishes [139,140]. For this reason, PC NPs hepatotoxicity was investigated *in vitro* taking advantage of second-generation upcyte® hepatocytes used as human hepatic cell model. These cells are genetically engineered hepatocytes deriving from primary human hepatocytes (PHH), which are commonly considered as the gold standard for *in vitro* drug metabolism and toxicity investigations. Nevertheless, PHH show some limitations: they maintain their metabolic functions for a short time when cultured ex vivo [141,142], and the supply of human liver tissue is mostly limited as well as the yield of PHH is generally low [142,143]. Upcyte technology has provided the generation of easy handling human hepatocytes that present functional features combined with the advantage of being derived on a large scale, which implies virtually unlimited availability of hepatocytes from different donors [141,143,144]. Their potential suitability for preclinical drug metabolism and for hepatotoxicity assessments has also been recently shown [144]. The first-generation upcyte® hepatocytes were shown to be responsive to cytochrome P450 (CYP) inducers. CYP constitute a superfamily of heme enzymes and they are involved in the biosynthesis of compounds or biotransformation of drugs and xenobiotics. CYP3A4 is the most important P450 enzyme for drug metabolism in humans. This is not only because of its amount in the liver, but mainly because it participates in the metabolism of the majority of drugs [145]. The second-generation upcyte® technology results to be the model do avoid the limitation of the PHH and an optimization of the first generation [141–144]. Therefore, in this chapter, the chemical properties of the formed PC NPs as well as the possible by-products released in the liquid environment during the laser ablation process (presented in the previous chapter) are fully characterized. Subsequently, the toxicological evaluation of the PC NP system is performed using the second-generation upcyte® hepatocytes as a human hepatic cell model in order to assess their impact to the human health.

Materials and Methods

Fabrication of PC NPs and dispersion

As discussed in Chapter II in the Material and Methods section, PC NPs and submicron particles were formed through the laser ablation of solid PC films immersed in water. To consent to the toxicological evaluation of the PC NPs, the ablation products synthesized by F 2.8 J/cm^2 were filtered and concentrated with a Rotavapor operating at 45°C in order to reach a definite concentration. To investigate the leachates release in the dispersant, an aliquot of PC NPs was further filtrated using Millipore Amicon™ Ultra Centrifugal Filter Units (cut-off 30 kD, Cat number UFC5030) at 10000 g for 30 min at 20 °C in order to separate the NPs dispersant by the particulate fraction.

High-Resolution Scanning Electron Microscopy (HRSEM)

A first morphological characterization was performed by HRSEM microscopy using a JEOL JSM-7500LA equipped with a cold field emission gun (FEG), operating at 10 kV acceleration voltage. After the formation of the PC NPs by the ablation process, the concentrated (by Rotavapor treatment) PC particle dispersion was drop casted on silicon substrates and dried in vacuum at room temperature. The samples were coated with a very thin layer (2 nm) of gold/palladium by a sputter coater (Cressington 208HR).

Transmission Electron Microscopy (TEM)

The morphology of the PC particles was evaluated using a JEOL JEM 1011 TEM microscope with a thermionic source (W filament) and accelerating voltage of 100 kV. The PC particle dispersions were drop casted on ultrathin carbon layered Cu grids (CF300-CU-UL) (Electron Microscopy Science) at room temperature. The size distribution of the NPs was determined using the ImageJ software and the Origin Pro version of 2018.

Raman Analysis

Chemical characterization was performed using LabRam HR800 (Horiba Jobin-Yvon Inc., France) spectrometer equipped with a built-in microscope with the 632.8 nm He-Ne laser excitation. After the concentration of the laser ablation products (by Rotavapor treatment) PC water dispersions were drop casted on a silicon substrate and dried at room temperature. A pristine PC film (4 mm^2) was also analyzed after being purified with ethanol followed by Milli-Q® rinses. The spectra were recorded in the spectral range from 360 to 3600 cm^{-1} and with a 100x objective lens with a spectral resolution of approximately 1 cm^{-1}. For the pristine PC, for each spectrum the acquisition time was 180 sec for one spectrum, and the final spectrum was a result of 20 repetitions, while for the PC particles the acquisition time was 20 sec for one spectrum with 10 accumulations. Graphical representation and normalization were performed with Origin Pro version of 2018.

X-ray Photoelectron Spectroscopy (XPS) Analysis

XPS measurements were performed with an Axis Ultra spectrometer (Kratos Analytical, Manchester, UK), using a Kα Al monochromatic source (hν = 1486.6 eV) operating at 150 W (15kV, 10mA) and a x-ray spot size of 400 × 700 μm^2 in hybrid electromagnetic lens configuration mode. The residual pressure of the chamber during the analysis was less than 8×10^{-9} Torr. Survey spectra (0–1150 eV, pass energy 80 eV) and high-resolution spectra (pass energy at 40 eV) were recorded. Surface charge was compensated by a magnetic charge compensation system, and the energy scale was calibrated by setting the C 1s hydrocarbon peak to 285.00 eV in binding energy. The data were acquired using Vision2 software (Kratos Analytical, UK) and the analysis of the XPS peaks was carried out using a commercial software package (CasaXPS v2.3.18PR1, Casa Software, Ltd., UK). Peak fitting was performed with no preliminary smoothing. Symmetric Gaussian–Lorentzian (70% Gaussian and 30% Lorentzian) product functions were used to approximate the line shapes of the fitting components after a 3-parameters Tougaard-type

background subtraction. PC NP dispersions were drop-casted on both clean Teflon substrates and Si-wafers. The use of Teflon substrate allows minimizing the uncertainties due to adventitious hydrocarbons contamination.

Dynamic Light Scattering and Zeta Potential Analysis

Zeta potential (Z-pot) of the PC NPs and the hydrodynamic diameter (D_H) of the dispersant were determined via dynamic light scattering (DLS) analysis using a Zetasizer Nano-ZS (Malvern Instruments) spectrometer at 25°C. Z-pot was studied at different pH values after pouring 10 µl of PC NPs dispersions (300 µg/ml) in 1 ml of the following buffer solutions: Tris (hydroxymethyl) aminomethane hydrochloride salt (Trizma hydrochloride, Sigma-Aldrich) in Milli-Q® water (pH 9-8, 0.002M), phosphate buffer saline (Sigma-Aldrich) in Milli-Q® water (pH 7-6, 0.002M) and diluted acetic acid (Sigma-Aldrich) in Milli-Q® water with sodium hydroxide (Sigma-Aldrich, pellet) (pH 5-4, 0.002M). After the separation of the particle population from the dispersant, each D_H distribution is performed after pouring 10 µl of different suspensions in 1 ml of in Milli-Q® water. Three consecutive measurements were run for all the suspensions. The colloidal stability of PC NPs in complete culture media was evaluated as a function of the incubation time (up to 48 hours). The surface charge of particle-corona complexes, in comparison to bare PC NPs (i.e. particles incubated in Hepatocyte High Performance Medium (HHPM) (Upcyte Technologies GmbH, Hamburg, DE), was measured via Z-pot analysis. Three consecutive measurements were run for all the PC NPs suspensions.

Untargeted Liquid Chromatography - Mass/Mass (LC-MS/MS) analysis

Samples were acquired in positive (ESI+) and negative (ESI−) ion modes with an ACQUITY UPLC system coupled to a Synapt G2 QToF high-resolution mass spectrometer (Waters, Milford, MA, USA). The column used was an ACQUITY UPLC® HSS T3, 1.8 µm internal diameter, 2.1x50 mm (Waters). Eluents were water with formic acid 0.1% (A) and acetonitrile with formic acid 0.1% (B) (Aldrich, Milano, Italy). Injection volume was 3 µL for ESI+ and 5 µL for ESI-. The flow rate was 0.450 mL/min. The column was kept at 45°C. Samples were eluted with a linear gradient of eluent B in A for 5 minutes before reconditioning. The total run time was 8 minutes. The scan range was set from 50 to 600 m/z (sensitivity mode). Cone voltage was 30 V. Source temperature was set to 90 °C, desolvation gas was 700 L/h and cone gas flows was 20 L/h for both ESI+ and ESI-, desolvation temperature was set to 400 °C. Data were acquired in MSE mode, alternating MS and MS/MS scans. The scan time was 0.3 s, low collision energy was set to 4 eV. The real-time spectra recalibration was performed using Leucine encephalin 2 ng/mL as Lock Mass. From the total extract chromatograms, the most intense m/z values were manually analyzed with MassLynx (Waters Inc.) and annotated for both ESI+ and ESI- polarities following already available references [8].

^{1}H Nuclear Magnetic Resonance (NMR) analysis

NMR spectroscopy was used characterize the dispersant and discriminate between the components due to the purification and that due to the ablation process. All NMR experiments were recorded at 25 °C with a Bruker FT NMR AvanceIII and AvanceNeo 600 MHz spectrometer

equipped with a 5-mm CryoProbe QCI $^{1}H/^{19}F-^{13}C/^{15}N$-D-Z quadruple resonance with shielded z-gradient coil, and the automatic sample changer SampleJet™ with temperature control. For all sample a ^{1}D ^{1}H spectrum with water suppression was obtained using the standard NOESY (nuclear Overhauser effect spectroscopy) preset Bruker pulse sequence, with 64 k data points, a spectral width of 30 ppm, 128 scans, an acquisition time of 1.84 s, a relaxation delay (d1) of 4 s and a mixing time of 100 µs. In each 5mm NMR tube were added 450 µL of sample plus 50 µL of D2O (for the lock signal) and 200 µM of 3-propionic-2,2,3,3-d_4 acid (TSP, for the ^{1}H chemical shift reference). To identify the solvent components, we added sequentially 1 µl of solvent (i.e. Aceton, MeOH, Formic Acid, Acetic Acid etc) in the same samples recording a NMR experiment after each addition. For the identification of the aromatic components, we follow the same approach adding the different compounds at a final concertation of 2 mM and recording the NMR spectra after each addition.

Upcyte® Hepatocyte Culture

Second-generation human upcyte® hepatocytes (derived from donor 653-03; Upcyte® Technologies GmbH, Hamburg, DE) were cultured as previously reported. After thawing, cells were expanded for 2 passages in collagen-coated tissue culture flasks (VWR, Radnor, PA, USA) and, finally, treated with PC NPs at passage 3 (P3) in collagen-coated flat bottom 24- or 96-well plates (Corning Incorporated, Corning, NY, USA), as described below. At P3, the number of viable cells was higher than 92.9%, as revealed by trypan blue (Sigma Aldrich-Merck KGaA, Darmstadt, DE) exclusion test. For avoiding alterations of cytochromes P450 activity, antibiotics were not used at any passage.

Cell Viability Assay

Resazurin reduction test was used for determining the cell viability after treatment with PC NPs dispersions. At P3, upcyte® hepatocytes were seeded into collagen-coated flat bottom 96-well plates (growth area: ~0.3 cm^2; ~1.2E5 cells/cm^2) and, the day after, were treated for 24 or 48 hours with increasing concentrations of PC NPs (0.1 mL/96-well) and the equivalent volume of dispersant and of Milli-Q® water after the ultrafiltration, as control. Cells treated with complete medium supplemented with 0.03% Triton X-100 (Sigma Aldrich-Merck KGaA, Darmstadt, DE) for 24 or 48 hours were used as a positive control of cell viability reduction. At the end of any time interval, stimulation media were replaced with 44 µM resazurin sodium salt (Sigma Aldrich-Merck KGaA, Darmstadt, DE) in serum-free phenol red-free high glucose DMEM (Sigma Aldrich-Merck KGaA, Darmstadt, DE) and, after 1-hour incubation, resazurin solution was transferred into a clean 96-well plate. Fluorescence was read at 535 nm by Tecan Spark® reader (Tecan, Männedorf, CH). Three independent experiments were carried out, each one arranged with a technical triplicate. In each experiment, a couple of cell-free collagen-coated wells per stimulation condition, incubated under the same condition, was used as blank value. Results are reported as percentages (means $\pm$ SD) of the control (set as 100%).

Cytotoxicity Assay

CytoTox96® Non-Radioactive Cytotoxicity Assay (Promega Corporation, Madison, WI, USA) was used for evaluating the cell membrane integrity after the different treatment. At the end of any incubation time interval, stimulation media derived from the cell viability assay were saved, centrifuged at 20000g for 15 minutes at 4°C and analyzed following manufacturer's instructions. The condition "0.03% Triton X-100" was used as positive control of cell membrane damage. Three independent experiments were carried out, each one arranged with a technical triplicate. In each experiment, a couple of cell-free collagen-coated wells per stimulation condition, incubated under the same condition, was used as blank value. Results are reported as percentages (means ± SD) of the positive control (set as 100%).

Reverse Transcription and Quantitative Real-Time PCR

At P3, upcyte® hepatocytes were seeded into collagen-coated flat bottom 24-well plates (growth area: ~2.0 cm^2; ~9.5E4 cells/cm^2) and, at the confluence, were treated for 24 or 48 hours with 40 µg/mL of PC NPs (0.667 mL/24-well) and the equivalent volume of dispersant and of MillQ water after the ultrafiltration, as control. At the end of any time interval, cells were extensively washed with DPBS (Sigma Aldrich-Merck KGaA, Darmstadt, DE) and incubated at -80°C with TRIzol™ Reagent (0.5 mL/24-well; Invitrogen-Thermo Fisher Scientific, Waltham, MA, USA). Total RNA was isolated following Chomczynski's protocol [146] and reverse-transcribed to first-strand cDNA (2 µg of RNA per sample in a 20-µL reaction) using SuperScript™ VILO™ cDNA Synthesis Kit (Invitrogen-Thermo Fisher Scientific, Waltham, MA, USA), following manufacturer's instructions. For each target gene, the transcript level was measured via quantitative Real-Time PCR (qPCR), using iTaq™ Universal SYBR® Green Supermix (Bio-Rad, Hercules, CA, USA) on Applied Biosystems ViiA 7 Real-Time PCR System (Life Technologies-Thermo Fisher Scientific, Waltham, MA, USA). Nucleotide sequence, temperature of annealing, qPCR efficiency and amplicon size of each primer pair are reported in Romaldini et al. The quantification of each target transcript relative to the control condition was calculated using Pfaffl's model [147]. Results are means ± SD of three independent experiments.

Statistical Analysis

Statistical analysis was run on Prism (GraphPad Software, San Diego, CA, USA). Ordinary one-way ANOVA was used for analyzing data from cell viability assay, cytotoxicity assay and qPCR analysis. If ANOVA revealed significant differences within a data set, Dunnett's multiple comparisons test was used. Differences were considered statistically significant as p value was lower than 0.05. All reported data are means ± standard deviations (SD) of three independent experiments.

Results and Discussion

Characterization of the PC laser ablation product

The first essential information to evaluate if the laser ablation in water is an efficient technique for the synthesis of a model of NPs is the characterization of the obtained product. Focusing on the F which gives the higher amount of NPs (2.8 J/cm^2), the entire ablation product has been analyzed by HRSEM (**Figure 16**). In accordance with what is observed for the degradation of bulk polymers in accelerated weathering testers [61], the plastic fragments produced, upon the interaction of the laser beam with the polymer target surface and the generation of the shock wave, have an irregular morphology and a broad size distribution.

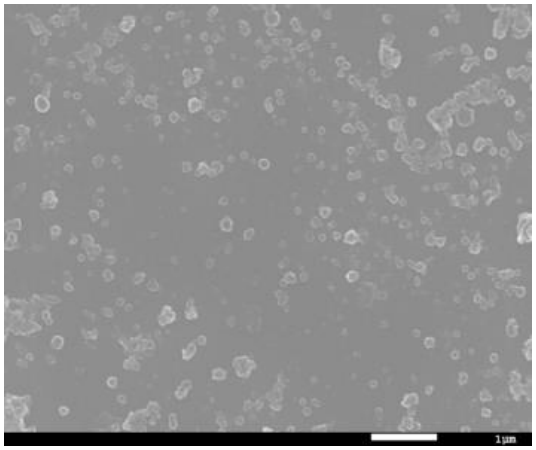

Figure 16. SEM images of PC ablation product after irradiation at F=2.8 J/cm^2.

In addition, the ablation product by 0.9 J/cm^2 is analyzed by TEM (**Figure 17**) for a morphological characterization of the sub-micron particles. By the TEM images is clear the high roughness on the surface of the sub-micron particles. On the left of the **Figure 17**, the clusters produce during the laser ablation process are shown.

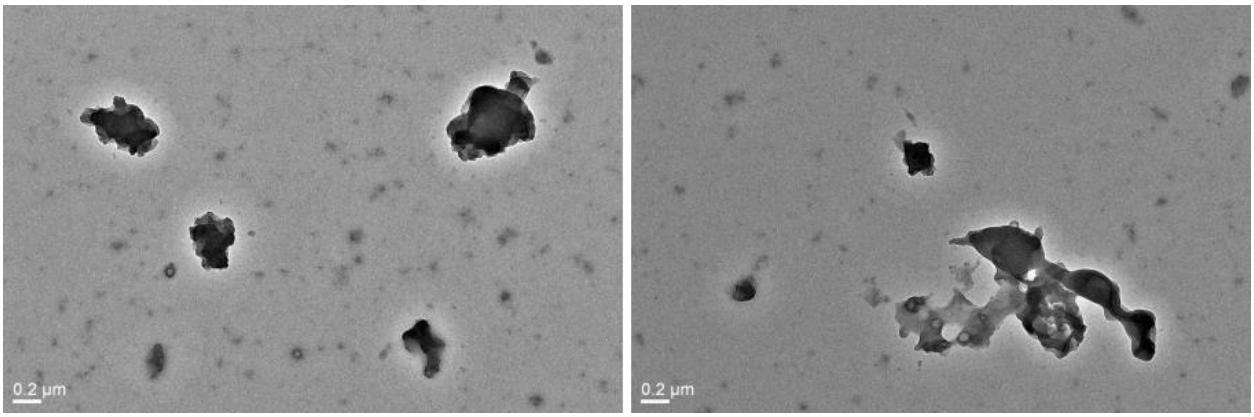

Figure 17. TEM images of PC ablation product after irradiation at F=0.9 J/cm^2.

A chemical characterization of these products was performed by Raman analysis. As shown in the normalized spectra of **Figure 18** the comparison with the pristine PC film shows no significant difference with both ablation products, with the main peaks characteristic of the PC chemical structure to appear in pristine and ablation product. **Figure 18 a** shows the spectra of the pristine PC with the ablation products containing the whole amount of NPs. In **Figure 18 b** the pristine PC is associated with the spectrum of the ablation product containing the whole of particles in the sub-micron range size. The frequencies of the observed bands in both spectra are summarized in the **Table 5** and each of them are represented in the spectra by the reference lines. Specially, an intense peak at 896 cm^{-1} associated with O-C(O)-O stretching, a set of three bands, 1118 cm^{-1}, 1186 cm^{-1} and 1245 cm^{-1} attributed to the C-O-C stretching, and a band at 1611 cm^{-1} which corresponds to the phenyl ring stretching mode. The sub-micro particles show an additional peak at 954 cm^{-1} representatives of the increase of the C-H bending. The band at 1460 cm^{-1} is attributed to the CH_3 deformation and 1787 cm^{-1} to the C=O stretching [123,148,149]. Therefore, the laser-ablated particles have all the peaks corresponding to the characteristic peaks of polycarbonate confirming that the PC is the chemical fingerprint of the ablation products.

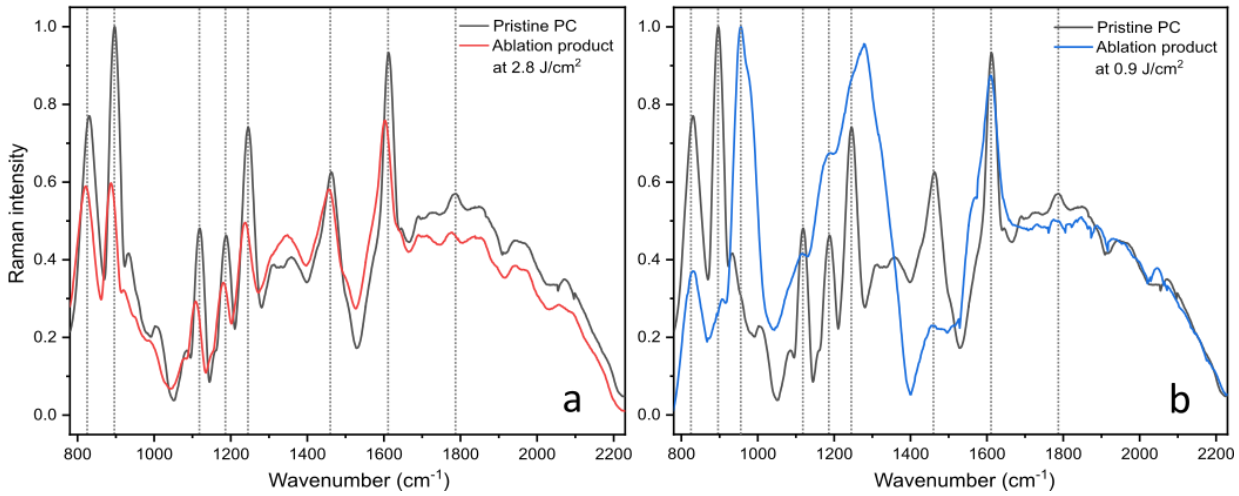

Figure 18. Raman analysis of pristine PC and the ablation product after irradiation at (a) F=2.8 J/cm^2 and (b) F=0.9 J/cm^2.

Frequency [cm^{-1}]	**Mode**
825	Phenyl ring vibration
896	O-C(O)-O stretch
954	C-H bending
1118, 1186, 1245	C-O-C stretch
1460	CH_3 deformation
1611	Phenyl ring stretch
1787	C=O stretch

Table 5. Assignment of the Raman modes for pristine PC and post-ablated PC at F=2.8 J/cm^2.

As the scope is to explore the biological fate of the NPs, the ablation product formed after irradiating with F of 2.8 J/cm^2 PC films immersed in water, was filtered in order to remove any possible PC big fragments and the final material was concentrated with a Rotavapor in order to prepare a stock solution of PC NPs of concentration of 300 µg/mL. The morphology of the PC NPs is investigated by TEM analysis as shown in **Figure 19 a**. Specifically the PC NPs show an almost spherical shape, with a mean size of 31.5 nm (scatter intervals= -20.3, +48.9 nm) (**Figure 19 b**), confirming the fact with the specific top-down approach, particles in the nanometer range are formed. This value is slightly lower compared to the D_H of the NPs in water as defined by the DLS measurements (see Chapter 2, **Figure 12** (D_H = 47.4 ± 3 nm, PDI= 0.190)), as usually occurs, due to the differences of the experimental methods.

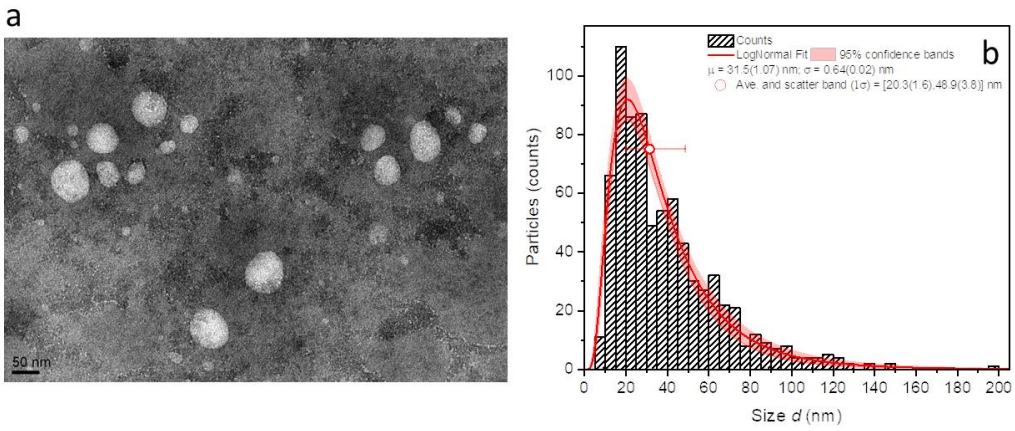

Figure 19. (a) TEM images and (b) corresponding size distribution analysis. The mean diameter of the NPs is 31.5 nm (scatter intervals = -20.3, +48.9 nm).

The surface chemistry of a material is a fundamental parameter necessary for the evaluation of its environmental and biological fate. XPS analysis was performed in order to identify the PC NPs surface chemistry. By the survey spectra analysis (**Figure 20**), the O/C ratio is higher in the NPs (O/C_{NPs}= 1.53 ± 0.04) compared to the PC film ($O/C_{pristine}$= 0.21 ± 0.02), that is similar to the ablated PC film ($O/C_{ablated}$= 0.20 ± 0.01), demonstrating a higher presence of the oxygen element on the surface of the NPs compared to the bulk films (O/C_{stoich}= 0.19). The percentage of the respective elemental compositions of survey spectra are represented in the **Table 6**. The additional elements (Chlorine, Fluorine and Sodium) are the typical contaminates of the water, indeed they are detected only on the PC NPs.

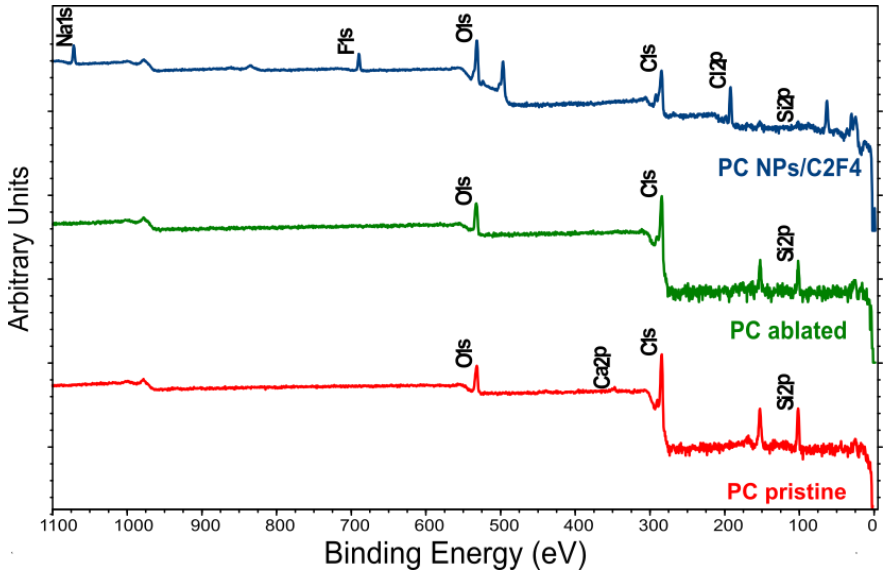

Figure 20. Survey XPS spectra of the pristine polymer and of the as-synthesized NPs with the respective elemental composition. NP dispersion drop-casted on Teflon (C_2F_4) substrate.

	Binding Energy	PC pristine	PC ablated	PC NPs/C_2F_4
C 1s	284.7 eV	78.60%	81.44%	29.66%
O 1s	532.2 eV	16.17%	16.65%	45.37%
Si 2p	102.2 eV	5.22%	1.91%	0.40%
Ca 2p	347.3 eV	0.31%		
F 1s	689.7 eV			8.9%
Na 1s	1071.16 eV			10.05%

Table 6. Percentage of respective elemental composition of survey spectra.

A more detailed study on the surface composition was performed through the deconvolution of the C1s spectrum (**Figure 21**) in order to identify the chemical groups of the surface, and the corresponding presence of each of them is presented at the **Table 7**. Concerning the C1s spectra, the contribution located at 284.8 eV, which corresponds to both the aromatic and aliphatic C–H/C–C groups, decreases in the NPs (58.4%) compared to both PC types of films (pristine PC: 83.5% and ablated PC: 65.8%). The peak at 286.3 eV is due to the presence of the C–O–C/ C–OH and it is higher in the NPs (17.8%) compared to the pristine polymer (8.7%), but lower than the ablated PC film (19.2%). A slight decrease is observed in PC NPs on the contribution of the O=C(–O)$_2$ group at binding energy 290.4 eV compared to the film surfaces (PC NPs: 2.0%, pristine PC: 2.6% and ablated PC: 3.7%). Furthermore, in the PC NPs a new peak at 287.7 eV representative of C=O group appears and a high increase in the component observed at 288.7 eV representing O=C–O is clear (pristine PC: 1.9%; ablated PC: 4.0% and PC NPs: 8.0%) [150]. **Figure 22** shows a graphical representation of the ratio of oxidized carbon bonds with the aliphatic/aromatic C-C bonds and it is clear the increase of their presence in the laser-ablated NPs compared with the

starting material. These relative abundances of different oxidized carbon bonds on the NPs surface qualitatively reflect oxidation chemistry, measured using a similar method, on plastic NPs proxies obtained via mechanical milling and fractionation from environmental plastic samples [151].

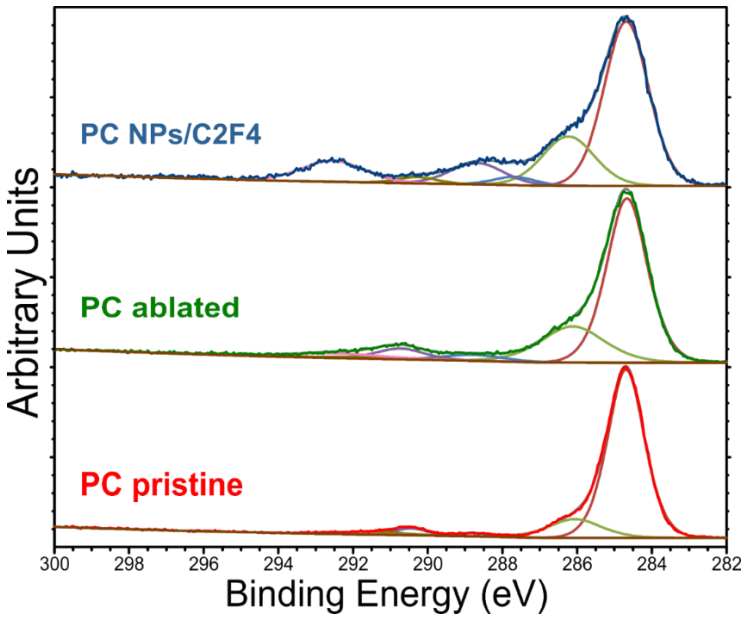

Figure 21. XPS C1s high resolution spectra of the pristine polymer and of the as-synthesized NPs with the corresponding deconvolutions. NP dispersion drop-casted on Teflon (C_2F_4) substrate.

C 1s	Binding Energy	PC pristine	PC ablated	PC NPs/C_2F_4
C-C, C-H (ar, al)	284.8 eV	83.5%	65.8%	58.38%
C-O-C, C-OH	286.3 eV	8.67%	19.22%	17.79%
C=O	287.7 eV			3.27%
O=C-O	288.7 eV	1.87%	4.01%	8.02%
$O=C(-O)_2$	290.4 eV	2.61%	3.73%	2.02%
C-C sh.-up (I)	291.3 eV	2.17%	2.27%	
C-C sh.-up (II)	292.5 eV	1.23%	4.94%	
C_2F_4	292.5 eV			10.52%

Table 7. Percentage of the areas of the deconvolution curves of the C1s spectra for the PC NPs, PC pristine films and PC ablated areas of the films. The C_2F_4 signal is attributed to Teflon substrate.

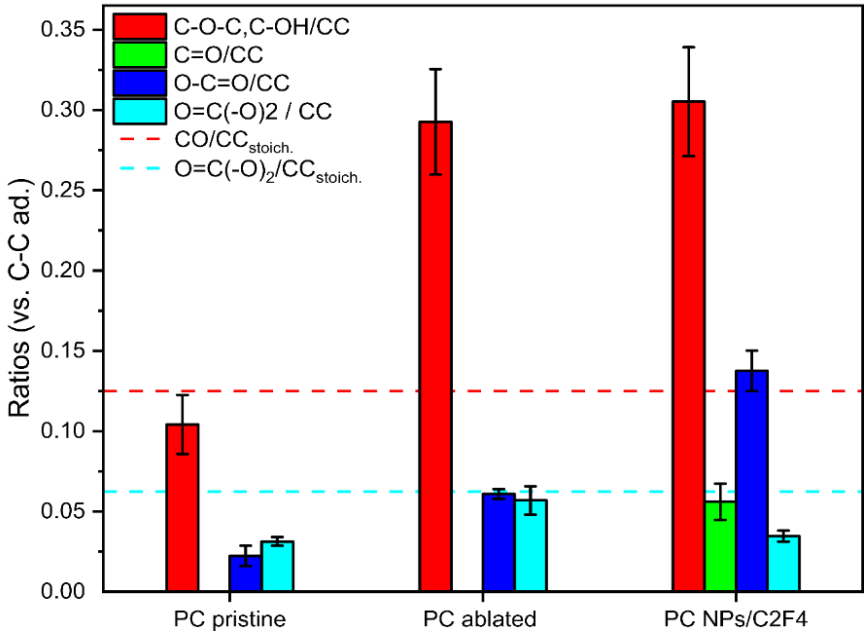

Figure 22. Atomic bonding distribution from XPS C1s spectra analysis of PC NPs in comparison with the pristine polymer (PC bulk film) and ablated PC polymer.

The analysis of the surface charge of the NPs dispersed in buffer media with different pH values by Z-Pot, have corroborated the presence of hydroxyl and carboxylic acid groups on the NPs surface [18]. In fact, as shown in **Figure 23**, NPs are negatively charged and show a behavior typically observed in colloidal systems with weak acid groups on their surface [152].

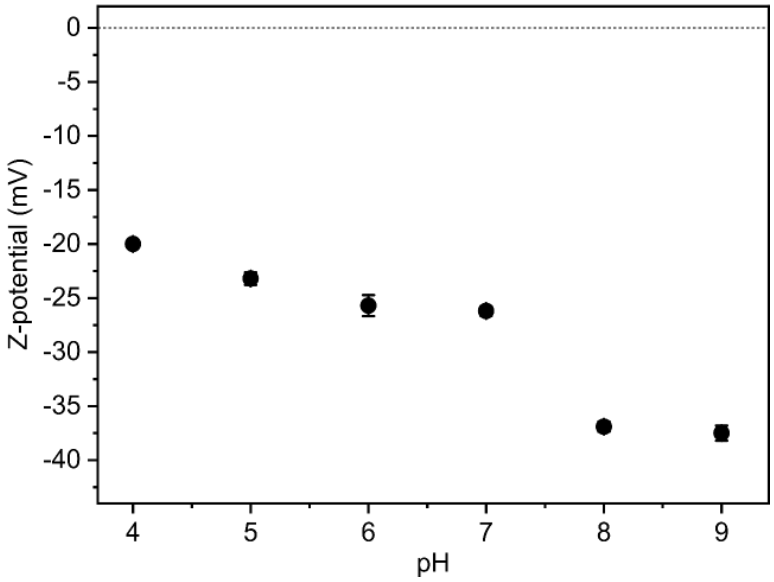

Figure 23. Z-Pot at different pH of PC NPs. The increasingly negative charge in the basic environment indicates the negative surface charge of the PC-NPs.

As shown above, the surface chemistry characterization of the NPs showed a net negative charge and a high oxidation degree with the exposure of carboxyl and hydroxyl groups on their surface, contrary to the pristine material. Such groups are characteristic oxidized functional end-groups of the degradation products formed following the thermo-oxidative and photodegradation pathways of PC in water [8,35]. In fact, such degradation products may be formed after the photodegradation of PC following the photo-Fries chemistry driven by UV with wavelengths < 300 nm and the photo-oxidation at longer wavelengths [125,153]. As already discussed in the beginning of this chapter, in the photo-Fries mechanism, the energy absorbed from UV radiation promotes the scission of the carbonate linkage, forming two primary free radicals. The free radicals then rearrange to form phenyl salicylates and dihydroxybenzophenones, and other groups such as dihydroxybiphenyl and hydroxydiphenyl ether groups [128,129,154]. Instead, the photo-oxidation occurs via a three stages reaction [129,130,154,155], the UV radiation is absorbed in the polymer, the hydrogen atoms are abstracted from the methyl groups, forming a free radical and thus initiating a chain scission reaction which propagates the reaction. In the presence of oxygen, the methyl side chains are photo-oxidized into hydroperoxide intermediates groups [127,153], which are transformed into carboxylic acid, ketone or hydroxyl end groups [8,156]. Based on these observations, it is possible to conclude that the PC NPs formed by laser ablation have the chemical composition as the PC fragments expected to be found in the natural environment.

Characterization of the leachate during the PC laser ablation

As discussed in the previous paragraphs, upon the photo-degradation of the PC NPs various low-molecular weight intermediates dropped from the polymer chain may be trapped in the particles or released to the leachate [8]. For this reason, the water medium in where the polymer film is ablated and therefore the water dispersant of the PC NPs is separated from the particles by an ultrafiltration column (cut-off 30 kD, [157]) and characterized, in order to identify possible molecular by-products. To verify the separation of the particulate population from the dispersant, DLS and UV Vis spectrophotometer analyses are performed. As shown by the DLS analysis (**Figure 24**), the dispersant's DLS spectrum does not show any peaks on the range of the NPs population, indicating the lack of particulate components. The represented peak at 1 nm is also present on the Milli-Q water, used ad control, where the laser ablation process occurs. On the other hand, the DLS characterization of the solution of the NPs recovered after the ultrafiltration process confirms the presence of NPs with similar D_H distribution as in the case of the PC NPs before any separation process. PC NPs complex is filtrated by a column with a cut-off of 30 kD and based on previous work, this column blocks particulate matter with dimensions < 30 kD, namely particles with a radius between 1.8 nm and 2.4 nm [157]. Particles with a diameter higher than 3.6 nm and 4.8 nm are blocked in the column. By these results, it cannot be excluded the presence of fragments lower than 2 nm in the dispersant, although this peak is also present in the Milli-Q water.

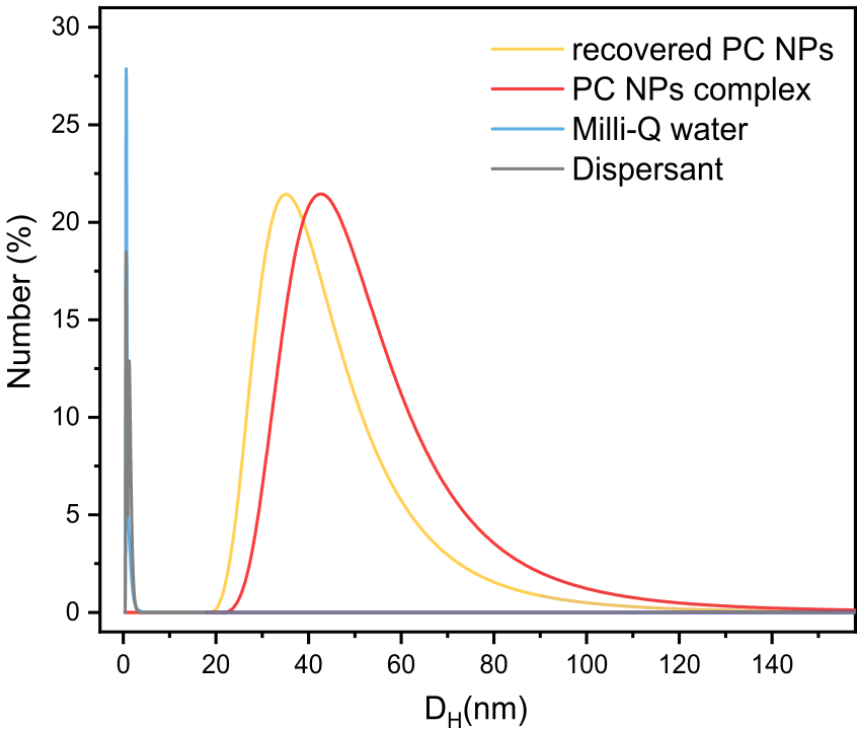

Figure 24. Hydrodynamic diameter (D_H) distribution of the starting PC NPs complex (solution before the ultrafiltration separation (red)) and the spectra of the two separated solutions: the dispersant (grey) and the recovered PC NPs (yellow). Milli-Q water spectrum is in blue.

The different samples are also analyzed by UV-vis spectrophotometer and the spectra are shown in **Figure 25**. As described in the Chapter II the 270–315 nm region of the PC UV vis spectra of PC is associated to the π - π* electronic transition [120,121] in the aromatic compounds. The strong π–π∗ peak at 290–300 nm is characteristic of aromatic compounds and is referred to as the peak of the phenyl group. The carbonyl group in PC is also a chromophore and the absorption peak at 280–290 nm is consistent with the PC carbonyl group n–π∗ transitions. The UV Vis spectrum of the dispersant shows the same curve of the starting solution, but the absorbance is significantly decreased (4-fold). On the top, the spectrum of the recovered NPs is very low. All this suggests that in the dispersant very small PC NPs, polymer fragments, or monomers detectable by the absorbance may be present, while the particulate population is significantly decreased during the filtration.

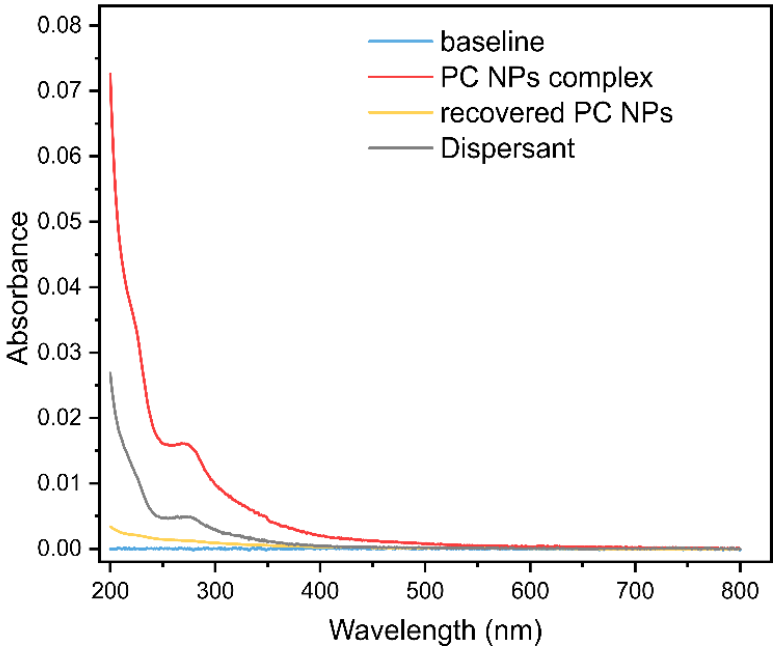

Figure 25. UV-vis spectra of the starting PC NPs complex (solution before the ultrafiltered separation (red)) and the spectra of the two separated solutions: the dispersant (grey) and the recovered PC NPs (yellow).

After that, high-resolution UPLC-MS analysis was performed to identify the molecular components detectable in the dispersant. Using as a reference the previous work on the identification of the photo-degradation by-products of the PC MPs [8], the obtained data are shown as representative examples in **Figure 26**. In particular, **Figure 26 a** shows the reference MS/MS spectrum of characterized compound P271 [8], while **Figure 26 b** shows the corresponding spectrum obtained for our sample. As indicated by the figure, four main diagnostic fragment ions (indicated by black arrows) are present in both the reference and test MS/MS spectra, unambiguously assigning P271 as structure for our representative degradation product. By comparing these two spectra it can be concluded that the by-products detected in the dispersant are also identified by the previous study (Shi et al., 2021) and are the result of the BPA leaching (peak 227.11) as also of the side-chain photo-oxidation of the PC. Specifically, the product by the carboxylation in the orthoposition of the rings is present (peak 271.09) [8]. In a similar way, the MS/MS spectra reported in **Figure 27**, also indicate that products P243a and/or P243b are likely present in our degradation mixture. In this case, the lack of available reference MS/MS spectra allows a structure assignment only based on manual interpretation of MS/MS fragmentation spectra. In both spectra, the intact species is clearly detectable (at 243.10 m/z), while the presence of “twin” ions at 227/228 (bottom spectrum) clearly indicate the presence of the bi-hydroxyphenyl rings in the molecule.

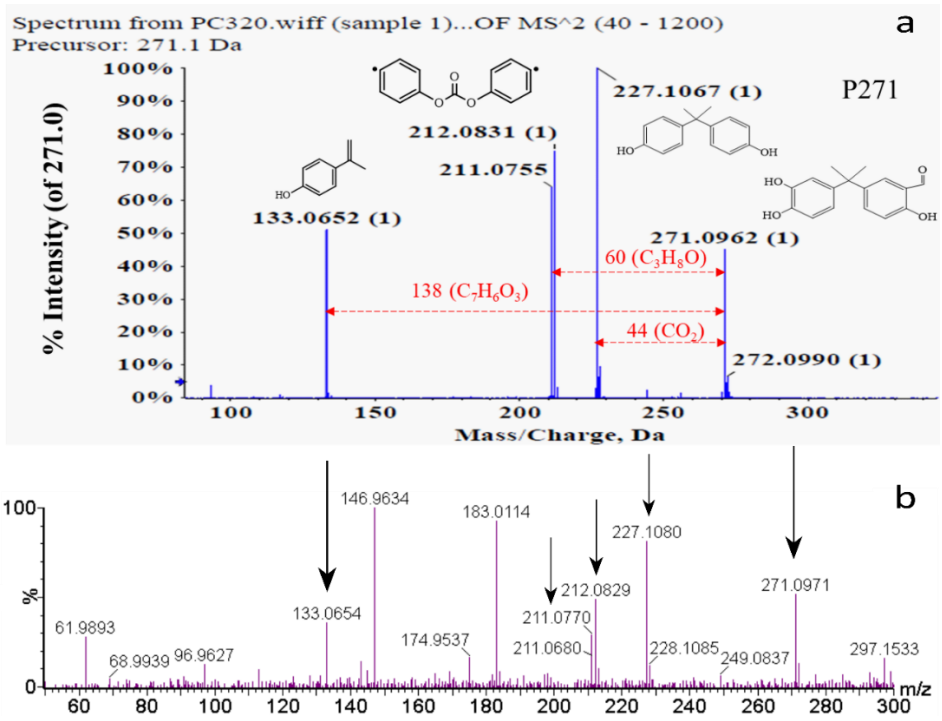

Figure 26. (a) MS/MS chromatogram of partial intermediates in the leachate detected by Shi et al. [8] P271 after the irradiation of PC MPs; (b) Corresponding MS/MS spectrum of one of the intermediates detected in the dispersant after the separation by the NPs population. The diagnostic MS/MS fragment ions, that confirm P271 structure for our unknown compound, are tagged by black arrows.

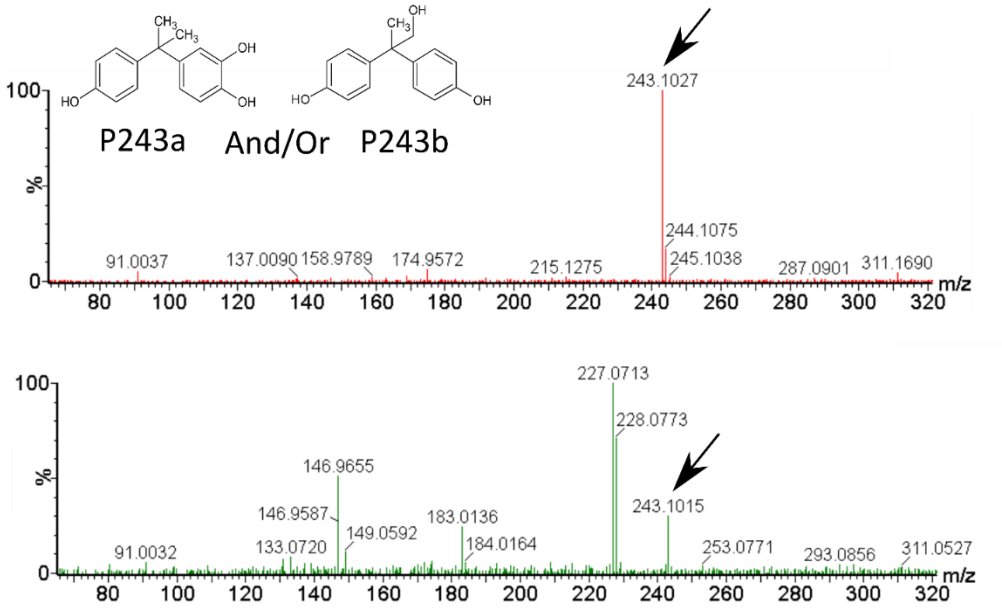

Figure 27. High-resolution MS/MS spectra of two isomeric species at 243.1 m/z, likely corresponding to degradation products P243a and P243b reported by Shi et al. 2021 [8].

In addition, the NMR analysis was performed. The NMR spectra of the dispersant showed very broad signals and some sharp peaks related to the chemical groups present on the NPs surface that are free to move and to different solvents originating from the ablation or from the purification process. Firstly, we try to identify the impurity that comes from the processes basing the analysis on the reported chemical shift and then adding these compounds to the sample as confirmation. For example, **Figure 28** shows the NMR spectra of the dispersant before (black) and after (red) the addition of different molecules that allow us to identify the presence of acetone, methanol, and acetic acid in the dispersant.

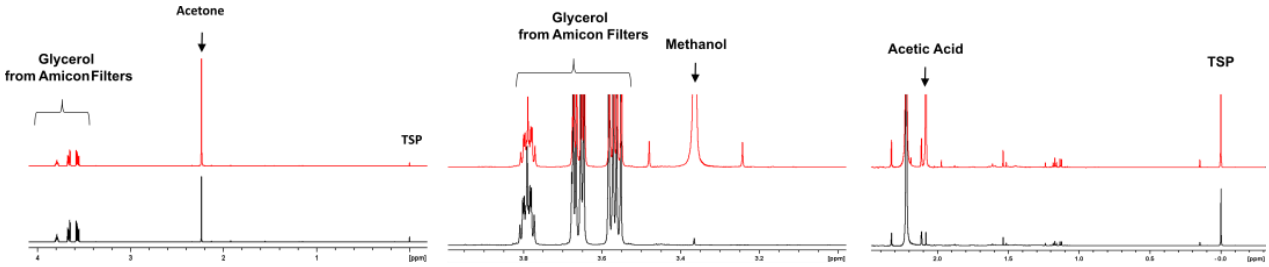

Figure 28. 1D ^{1}H spectra of the dispersant in black and the dispersant with adding of acetone, methanol and acetic acid in red to confirm the presence of these products in the dispersant.

The acetic acid is one of the ablation products also of the PET NPs produced by laser ablation[18]. Acetone and methanol are not associated with some products by the photo-degradation of the PC, so an assumption is that they are derived by one of the steps for the synthesis. Comparing the spectra of the dispersant before and after the ultrafiltration step, we can conclude that the glycerol observed in the final sample comes from the Amicon™ Ultra Centrifugal Filter. We then proceeded in the same way, we also identified the aromatic NMR signals in the spectra coming presumably from the PC ablation process. The intention was to test the compounds detected by the MS/MS spectrum (**Figures 26** and **27**), but they were not commercially available. Therefore, some other commercially available compounds previously defined as photo-degradation products of PC[8] were tested. **Table 8** shows the compounds taken into consideration, but unfortunately, the NMR analysis was able to confirm only the presence of BPA (**Figure 29**).

Identified by Shi et al., 2021	**Available in Sigma**	**CAS Number**
P135a	1-(4-Hydroxyphenyl)ethanone	99-93-4
P213	4,4'-Dihydroxybenzophenone	611-99-4
P151a	2-(4-hydroxyphenyl)acetic acid	156-38-7
P151b	Methyl 4-hydroxybenzoate	99-76-3
P93	Phenol	108-95-2
-	Bisphenol A	80-05-7

Table 8. Intermediates by the PC photo-degradation identified by Shi et al., 2021 [8], but not available to buy for the NMR analysis.

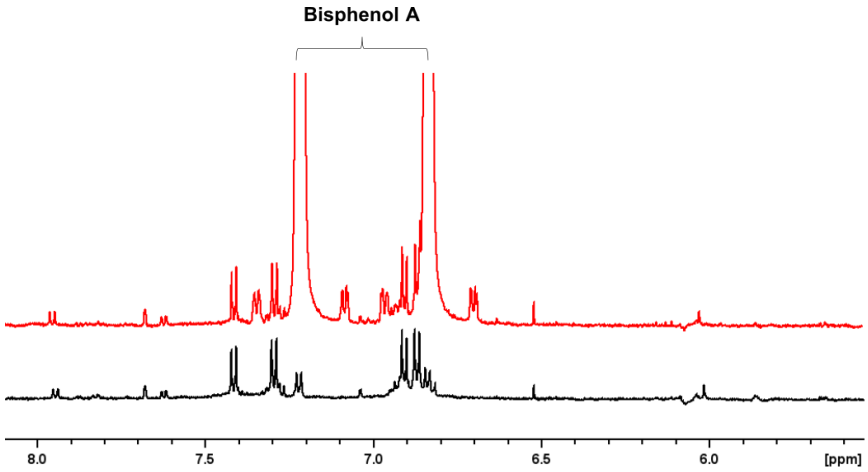

Figure 29. 1D ^{1}H spectra of the dispersant in black and the dispersant with adding of BPA in red to confirm the presence of these products in the dispersant.

By these results, it is possible to conclude that the ablation process offers the possibility to produce a PC NPs mixture, which contains compounds and NPs as in the natural photo-degradation process of the PC-based macroplastics. Indeed, during the degradation process of the PC plastic litter exposed to the environment, NPs are released as such together with many other degradation products, such as residual unpolymerized monomers, oligomers and other degradation products of the plastic polymer itself [39,158]. Therefore, with the herein proposed method, we offer the possibility to mimic this procedure and to obtain a NPs dispersion where are also present the photo-degradation by-products. This enables a more realistic exploration of the biological fate of PC and its degradation products.

Toxicological assessment of PC NPs in upcyte® hepatocytes

The herein presented study is performed in collaboration with the Nanoregulatory Group of D3-PharmaChemistry-IIT, leaded by Dr. Stefania Sabella. The study is still ongoing and the obtained results will soon be published (manuscript in preparation).

To evaluate the colloidal stability of the PC NPs in the cells culture medium, they were dispersed in complete HHPM (i.e. the culture medium of upcyte® hepatocytes) and their stability was assessed by monitoring the D_H variation as a function of the incubation time by performing a DLS study (data no shown). From this study it is concluded that upon a long incubation interval (48 hours), the size distribution profile analysis of the particles dispersed in complete HHPM was almost unvaried, indicating a temporal stability of the dispersion. After the confirmation that the NPs are stable in the culture medium of upcyte® hepatocytes, second-generation upcyte® hepatocytes were acutely treated for 24 or 48 hours with a range of PC NPs concentrations in the commonly applied range for nanomaterial toxicology studies (20-100 µg/mL) [18]. As shown in **Figure 30 a,c** for all concentrations tested no cytotoxic effects were observed upon 24 hours of exposure. Specifically, no significant alterations of cell viability (with respect to the control condition) and no statistic release of the cytosolic lactate dehydrogenase (LDH) were observed,

which indicates the absence of cell membrane damage. After 48 hours of treatment, only the highest concentration of PC NPs (100 µg/mL) affected the cell viability and cytotoxicity, with a dramatic decrease of the viability to 8% of the control condition ($p < 0.0001$) (**Figure 3 b**), along with a significantly increased release of LDH ($p = 0.0012$; **Figure 30 d**). When compared to the positive control, the release of LDH induced by PC NPs was equal to about 68% of the release obtained with 0.03% Triton X-100. Under the same condition, cells treated with PC NPs at all concentrations, after 24 hours appeared to be morphologically similar to the control cells (**Figure 31 a**). However, after 48 hours, the treated cells showed significant morphological changes and reduced dimensions with respect to the control cells (**Figure 31 b**). These results confirm previous investigation on the laser ablated PET NPs [18]. Focusing on the lower concentrations, it seems that PC NPs and PET NPs could exert no cytotoxicity. In support of such a negative impact at highest concentration of NPs, it has been reported that PS NPs (50-100 nm) were also cytotoxic on human colon adenocarcinoma Caco-2 cell line at nearly comparable concentration (200 µg/mL) and exposure time (starting from 24 hours) [159].

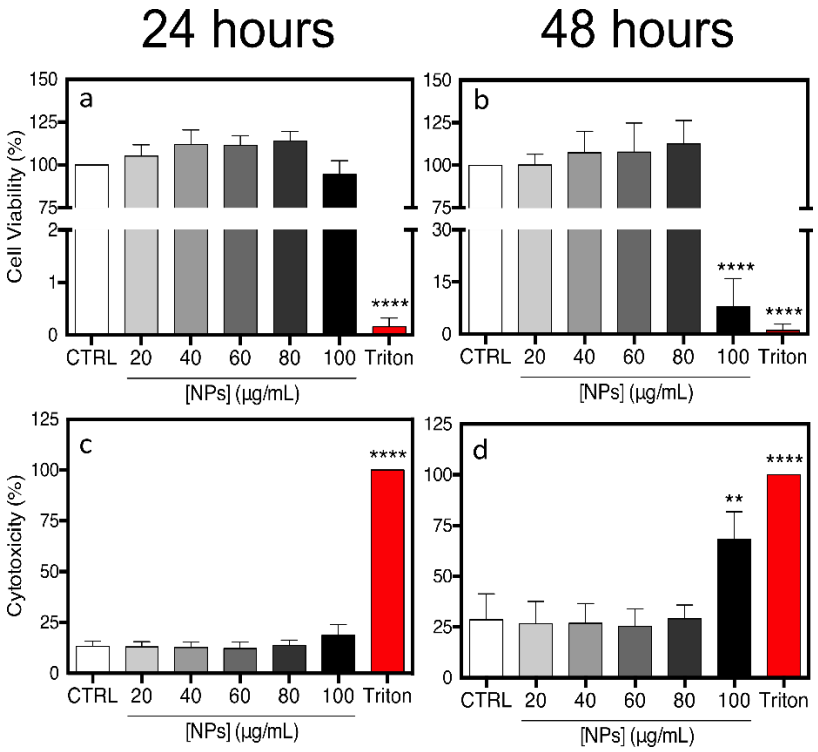

Figure 30. Cell viability by resazurin reduction assay upon (a) 24 and (b) 48 hour exposure and cell membrane integrity by cytotoxicity assay upon (c) 24 and (d) 48 hour exposure. "CTRL" refers to un-treated control cells and "Triton" to the positive control, represented by cells treated with 0.03% Triton X-100. Results are means ± SD of three independent experiments. The symbols ** and **** refer to $p = 0.0012$ and $p < 0.0001$, respectively, calculated *versus* CTRL (ordinary one-way ANOVA). Data courteously provided by Dr. Alessio Romaldini, Nanoregulatory Group of D3-PharmaChemistry-IIT.

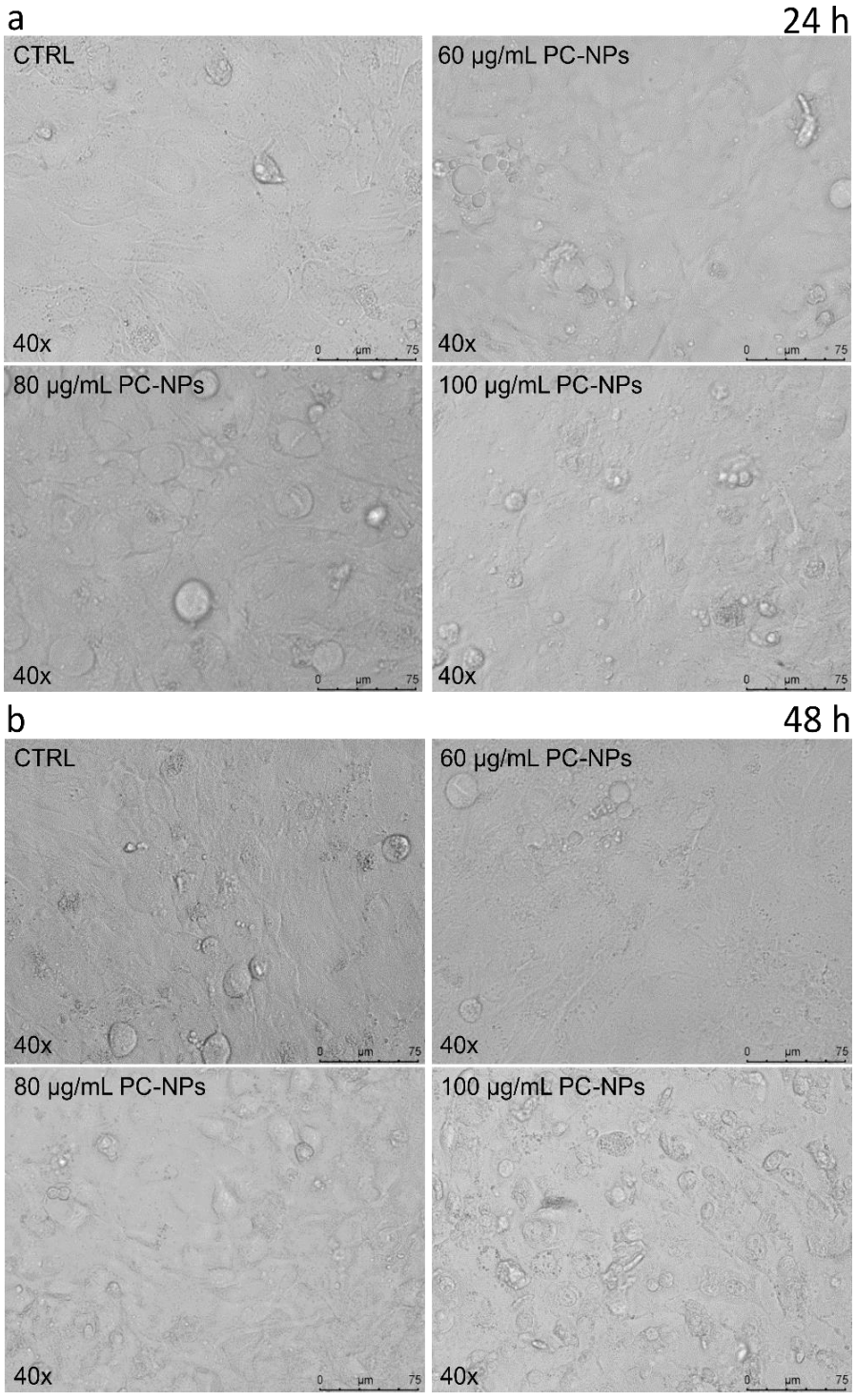

Figure 31. Representative images by optical microscope relative to cells treated with different PC NPs concentrations or un-treated for 24 (a) or 48 hours (b). All the images are 40x magnifications (scale bar = 75 µm). Data courteously provided by Dr. Alessio Romaldini, Nanoregulatory Group of D3-PharmaChemistry-IIT.

As previously shown, during the PC NPs fabrication process apart from the NPs formation, also other by-products are formed. Therefore, together with the evaluation of the effect of the PC NPs suspension to the hepatocytes, also the effect of the NPs dispersant is evaluated. To do so, a specific concentration of PC NPs was chosen (40 µg/mL) which does not affect the cells viability (**Figures 30,31**) and is more realistically close to the environmental possible *in vivo* acute exposure on liver, and after the separation from the NPs, the effect of the dispersant on the cell viability is also analysed (**Figure 32**). In particular, the second-generation upcyte® hepatocytes were treated for 24 or 48 hours with the equal volume, used for 40 µg/mL of PC NPs, of the dispersant separated by the PC suspension. The isolated dispersant showed no cytotoxic effect, as also the complete PC NPs suspension. In fact, no significant alterations of cell viability with respect to the control condition is shown.

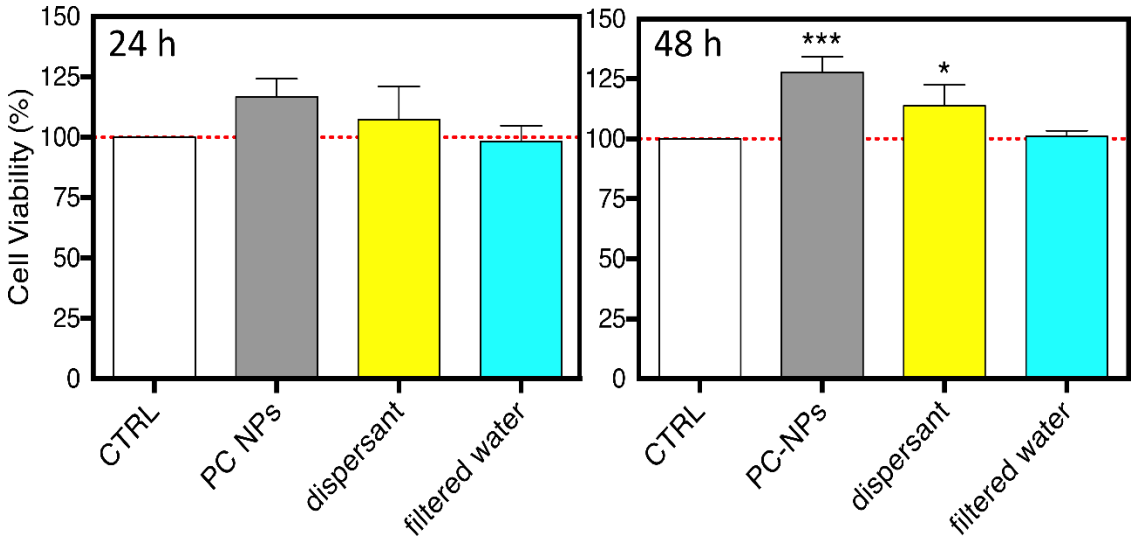

Figure 32. Cell viability by resazurin reduction assay upon 24 and 48 hour exposure. The cells are treated with PC NPs at 40 µg/mL and an equal volume of dispersant and filtered water (pure water subjected to the ultrafiltration process using the same type of filter and conditions). "CTRL" refers to un-treated control cells. Results are means ± SD of three independent experiments. The symbols ** and **** refer to $p = 0.0012$ and $p < 0.0001$, respectively, calculated *versus* CTRL (ordinary one-way ANOVA). Data courteously provided by Dr. Alessio Romaldini, Nanoregulatory Group of D3-PharmaChemistry-IIT.

To assess the PC-NPs impact on the hepatic functionality, CYP3A4 (one of the most abundant hepatic CYPs [160]) and Albumin were chosen as hepatocyte-specific markers [141–144]. Albumin is chosen because it is mainly synthesized *in vivo* by the hepatocytes and is the most abundant plasmatic protein involved in the maintenance of blood colloid pressure and in the binding and transport of endogenous molecules, xenobiotics and drugs [161,162]. The PC-NPs concentration used for the treatment (40 µg/mL) was chosen to be lower than the toxic exposure limit to the cells, in order to safely validate any possible effect observed as a result of the interaction with the

suspension and not due to a global cell impairment. The corresponding dispersant after the ultrafiltration process and the removal of the PC-NPs was also evaluated in order to better evaluate the results. As shown in **Figure 33 a**, after 24 hours of stimulation the CYP3A4 gene expression was down-regulated, reaching a level equal to 0.25-fold with respect to the control for both, the PC NPs suspension and for the isolated dispersant. In a longer stimulation time period (48 hours), the impact of PC NPs and dispersant on CYP3A4 causes a further significant downregulation compared to the 24 hours, having transcript levels equal to 0.10-fold lower than the control condition (**Figure 33 b**). **Figure 33 c,d**, shows the effects of the studied dispersion in the production of Albumin. As shown, the treatment with both, the PC NPs at 40 µg/mL and the respective dispersant resulted in the attenuation of the Albumin gene expression by ca 0.5-fold compared to the control level after 24 and 48 hours of treatment.

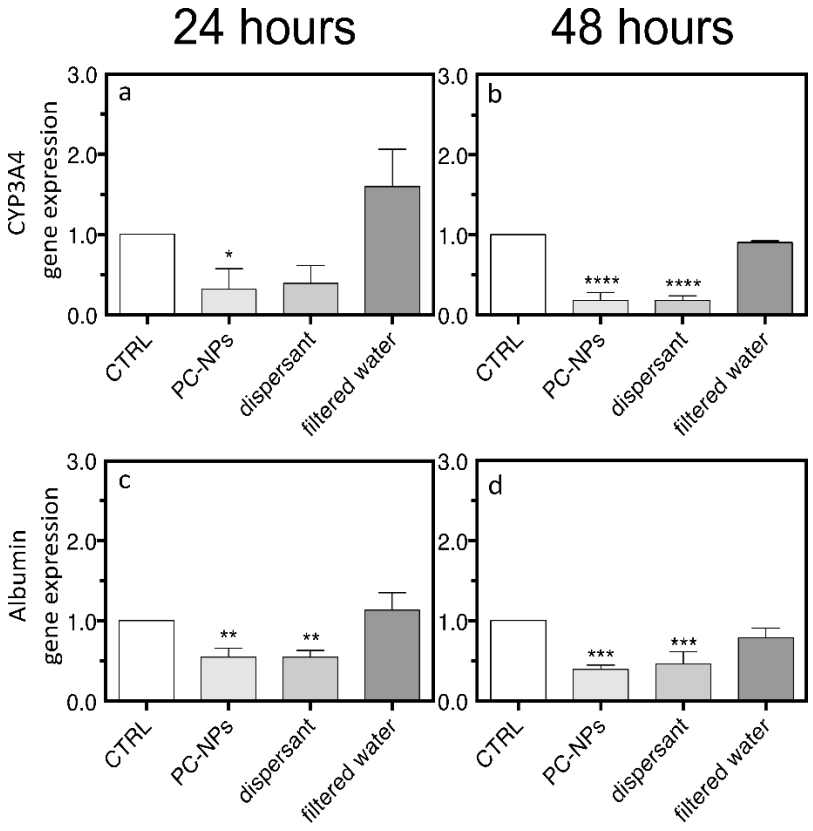

Figure 33. Relative gene expression of (a, b) CYP3A4 and (c, d) Albumin in cells treated for 24 and 48 hours with PC NPs at 40 µg/mL and an equal volume of dispersant and filtered water. "CTRL" refers to un-treated control cells. Results are means ± SD of three independent experiments. The symbols *, **, *** and **** refer to $p \leq 0.0495$, $p \leq 0.0078$, $p \leq 0.0004$ and $p < 0.0001$, respectively, calculated *versus* CTRL (ordinary one-way ANOVA). Data courteously provided by Dr. Alessio Romaldini, Nanoregulatory Group of D3-PharmaChemistry-IIT.

All these results indicate that there is not a great difference between the entire suspensions of PC NPs and the dispersant separated from the particulate. Both of them have no effect on the cell viability, but show a downregulation on both markers. Since CYP3A4 is the most abundant

CYP in the human liver and is involved in the metabolism of the majority of marketed drugs [145,160], a down-regulated gene expression, with a possible translation into a reduced amount of the corresponding protein, could determine undesired drug-drug interactions or impaired xenobiotic/drug detoxification. As far as Albumin is concerned, a severe effect of the PC NPs suspension could induce hypoalbuminemia (i.e. pathologically low levels of Albumin in the blood), which may cause nutrition deficits or altered pharmacokinetics of bound drugs and, in extreme circumstances, may lead to abnormal accumulation of fluids into extravascular spaces [163,164]. In a next step of this work, a study on the effects of the purified NPs population is also performed, in order to explore if the negative impact could be associated only to the dispersant or also to the NPs (confidential data not shown, manuscript in preparation).

Conclusions

The production of a realistic model of PC NPs was achieved through a top-down laser ablation technique. Chemical analysis demonstrates that the composition of the NPs is in accordance with what has been observed in environmental PC MPs and NPs. The identity of the by-products formed during the fabrication process is similar to the ones produced during the photo-degradation process of PC materials when exposed to the environment. Taking into account that PC NPs are formed in the environment by the photo-degradation of bigger PC fragments, the specific fabrication method it is offered the opportunity to fabricate an environmentally relevant sample that contains not only the PC NPs but also the byproducts released in the environment during their formation. Although many studies of toxicity and uptake have been dedicated to a wide variety of polymeric nanoparticles, mostly polystyrene has been used to model NPs and to investigate the effects to biological systems. Published data on the cytotoxicity have shown high variability mainly depending on the particles size, surface properties, and on the in vitro models adopted. Therefore, in order to clarify the biological fate of environmental NPs, it is necessary to consider the importance of the NP nature and composition, so all the conclusions based on studies using only synthetic polystyrene nanoparticle models have to be taken with caution. In this study, although the results obtained in vitro did not show any lethal or short-term toxic effects, they caused a significant alteration of the expression of the Cytochrome P450, and also an impaired Albumin production, concluding that the PC NPs dispersions can be toxic towards hepatic functionality even though they would not provoke direct damage of hepatocyte population.

Chapter IV

Exploration of different toxicological evaluation methods for the biological fate of NPs

Abstract

The work shown in this chapter is in collaboration with the Nanobiotechnology Laboratory in the European Commission Science Centre, Joint Research Centre (JRC) in the F2 Unit in Ispra (Italy). In this chapter, the comparison in terms of toxicity between three different types of NPs on two different cell models was investigated. Two types of laser-ablated NPs (polycarbonate (PC) and polyethylene terephthalate (PET1)) were studied in comparison with PET NPs (PET2) made by nanoprecipitation. In comparison to the particles made by nanoprecipitation, the Laser-ablated NPs were generally smaller, had broader size distributions and had a higher degree of oxidation on their surface. A toxicological evaluation was performed on HePG2 and Caco-2 cells by different *in vitro* techniques. Starting to the conventional colorimetric assays, the impact of NPs is also evaluated by high throughput screening (HCS) and electric cell-substrate impedance sensing (ECIS) technology. PC NPs were found to be more toxic than PET1 NPs, whereas the PET2 NPs showed no toxicity. Interestingly, on a model of the intestinal barrier none of the NPs induced any measurable toxicity.

State of art

Toxicological assessment methods

As mentioned in the previous chapter, apart from the size, also other physicochemical characteristics of the NPs such as shape, surface properties, and chemical composition can influence their behavior in the environment and their interactions with biological systems. An important aspect when assessing the effect of NPs on biological systems is the evaluation of their toxicity. In particular, *in vitro* cytotoxicity testing is an integral part of the identification of the hazardous potential of different chemical compounds and nanoparticles, also used in the early phase of drug development providing initial insights into the toxic potential of drugs at low costs and in a short timeframe. Generally, safety data for nanoparticulate materials can be obtained by testing their cytotoxicity in accordance with guidelines published by international standards development organizations such as the International Organization for Standardization (ISO) or the American Society for Testing and Materials (ASTM) [165]. A limitation to the applicability of the standardized *in vitro* cytotoxicity test methods for nanoparticles assessment is the possible interference of the nanomaterial with the test reagents or at the assay readout that can lead to false predictions as reported in several publications [165–168]. Similarly, the recently released guidelines state that the various assays described in the ISO 10993 series are not always appropriate in the testing of nanomaterials [169]. Therefore, it is important to explore different *in*

vitro evaluation methods, also in combination with advanced methodologies such as omics or new imaging technologies [19,170], in order to explore the NPs adverse effects in humans. Having in mind these considerations, the *in vitro* cytotoxicity of 3 different types of NPs is evaluated using different technologies in order to have a more representative view of the effects of the NPs on human cells. In this chapter, two types of laser-ablated NPs (PC and PET) were studied in comparison with PET NPs synthesized by nanoprecipitation (PC, PET1 and PET2 respectively). Already performed studies on these NPs (Chapter III for PC NPs, Magrì et al. 2018 [18] for PET1 NPs, and Johnson et al. 2021 [96] for PET2 NPs) show no effects on the cell viability. However, results on the cellular membrane permeability by LDH assay are different between laser ablated NPs and colloidal PET NPs. In particular, Johnson et al. 2021 detect a significant increase of LDH release, indicating the PET2 NPs have a negative impact on the permeability of the cellular membrane, but this is justified by the interference of PET NPs by their internalization [96], as the mitochondrial activity does not change at all concentrations tested. For this reason, in this work the toxicological assessment was performed by means of a combination of common *in vitro* assays, as the lactate dehydrogenase (LDH) release and the 3-(4,5-Dimethylthiazolyl-2)-2,5-diphenyltetrazolium bromide (MTT) reduction test, with more advanced high content screening (HCS) techniques. Moreover, for a more realistic model to assess NPs interaction, differentiated Caco-2 cells have been also used for analyzing the possible impact on the barrier function by electric cell-substrate impedance sensing (ECIS) technology. In the next paragraphs, each of the adopted methods will be discussed in order to demonstrate the importance of the followed methodologies for the cytotoxic assessment study performed herein. Another impediment to the development of reliable *in vitro* screening methods is the need for accurate dosimetry. In most *in vitro* studies, the initial concentrations of particles dispersed in the culture medium were considered as the effective concentrations, as it is normally done for water soluble chemicals. But, chemical dosimetry *in vitro* is a problem of two dimensions: amount and time (duration and timing), dosimetry for nanoparticles is a problem of multiple dimensions, adding to amount and time, there are physical characteristics of the particles (size, shape, and agglomeration state), core particle, and surface chemistry. Furthermore, dynamic modifications of the particles may occur upon mixing with biological media resulting in agglomeration, aggregation, and formation of the protein corona. These alterations might change the size and apparent density of NPs. This in turn may directly influence their transport towards the cell monolayer [171]. Consequently, the number of NPs effectively reaching the cell monolayer may differ drastically from the nominal dose, the transport of the NPs towards the cell monolayers, the NP affinities with the cells and the capacity of the cells to take up the NPs [172]. Several studies have been focused on the effects of the dosimetry on the nano-toxicity, Wittmaack, 2011 confirmed the height of the cell culture medium, the mass concentration, the mean particle size, and the time of exposure are fundamental in the *in vitro* assessment of NPs [173]. Moreover, Rischitor et al., 2016 demonstrated the importance of the choice of the NPs concentration. The presence of the protein corona increased the diameter of the NP complex and because the proteins have a lower density than the NPs, this results in a decrease in the overall apparent density of the complex. Moreover, the increase on the sedimentation time of the NP complex shows that the decrease of the mass

density has more influence than the increase of diameter. This effect is relevant for the small and dense particles [174]. In this case, the densities of the different materials, which are shown in **Table 3** (Chapter II), are similar. For this reason, has been expected that the NPs amount that reaches the cells are the same and the used concentrations are chosen based on the previous works (Magrì et al. 2018 [18] and Johnson et al. 2021 [96]).

High content screening (HCS)

HCS is a technology successfully used in the field of drug discovery [175] and toxicology [176] as it provides the opportunity to rapidly analyze a large number and variety of biological assays that may include several substances in each assay in the same experiment [177], and recently it has been suggested as a powerful technology to assess the potential toxicity of nanomaterials [178]. Nonetheless, the first to employ high-content image analysis, in conjunction with high-throughput analysis, to study the cytotoxicity of nanomaterials was Zhang et al. who investigated the cellular and molecular effect of high doses of Quantum dots QDs on human lung and skin [179]. HCS is a relatively recent advance in the integration and automation of quantitative fluorescence microscopy and image analysis. Combining automated image acquisition and powerful algorithms designed to quantify and extract the maximum amount of information from a population of cells, HCS generates great quantities of data for a large number of cellular characteristics, such as cell proliferation, cellular morphology, membrane permeability, lysosomal mass/pH, DNA and chromosome damage, activation of transcription factors, mitochondrial membrane potential changes, oxidative stress monitoring and post-translational modification [177]. Therefore, this versatile multi-parametric platform enables the user to analyze multiple parameters for a high number of samples, minimizing input while maximizing the experimental output [180]. Advanced technologies, such as HCS, have the advantage of providing reliable data in terms of statistics, and in parallel to its applications in assessing basic information on the toxicity of the NPs, it could also indicate the interaction of the nanomaterial with the various cell compartments and contribute to the clarification of the mode of action of the xenobiotic candidate [175,181,182]. Moreover, HCS has now been demonstrated to be applicable to cells in suspension as well as to adherent cells [183] and to peripheral blood cells as well as to cell cultures [184]. The HCS results to be a fundamental tool for this typology of study.

Electric cell-substrate impedance sensing (ECIS) technology

ECIS is a real-time and label-free, impedance-based method. It allows the assessment of various attributes of cell behavior such as cell adhesion and barrier strength by measuring the impedance across a confluent cell monolayer. To do so, the cells can be grown on gold-plated electrodes which apply an AC current through the cells. The potential created can be used to calculate the impedance, which typically increases and then plateaus as the cells become confluent and form a barrier or a monolayer, restricting current flow. Applying on the cellular monolayer various stimuli may result in the alteration of the impedance obtained. This may occur if a given stimulus disrupts the barrier integrity, creating a path of lower resistance, which allows easier current flow (increasing permeability as shown in **Figure 34**) [185].

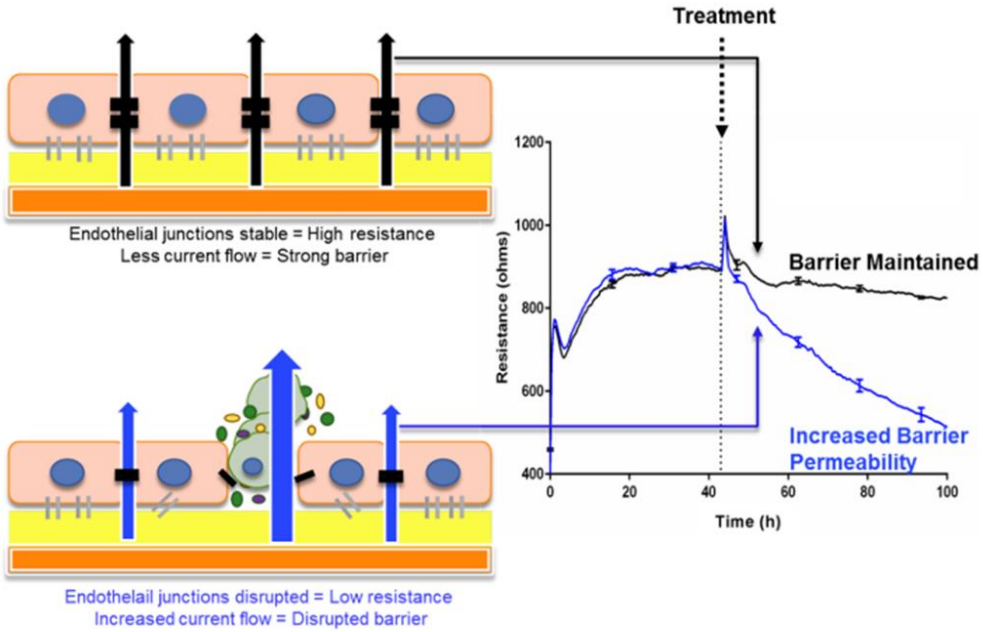

Figure 34. Schematic explaining ECIS theory. This shows endothelial cells growing on gold electrodes which are coated with rat tail collagen I. The endothelial cells form a monolayer by forming junctions with each other and the collagen substrate, shown by black and grey bars respectively. Once these junctions are formed, less current, supplied by the electrode, can flow through the cell junctions. This increases the electrical resistance as seen on the graph (right). As the cells become confluent, maximum resistance is achieved and the resistance plateaus. Upon treatment with factors that disrupt the endothelial barrier, the junctions weaken, current flows more freely between the cells and the electrical resistance decreases (blue trace, right).

With this method, a decrease in impedance or "barrier resistance" suggests a loss of barrier strength, as the current can freely flow through the disrupted cell monolayer. The ECIS electrodes can measure acute temporal changes in barrier resistance across the cell layer, and then model the collected data to provide information on separate components of the cell barrier. The basis for the measurement of the electrical impedance of biological objects is Ohm's law, a basic electro-technical principle, which describes the relation between resistance (R), current (I) and voltage (U) in an electrical circuit at a given time (t) [186].

Applicable in DC circuit: $R(t) = \frac{U(t)}{I(t)}$ (2)

When working in the AC system, current and voltage not only differ in their amplitude, but also in their phase (φ) and the resistance is no longer sufficient to describe these relations. Therefore, the complex impedance (Z) or in most cases the magnitude of the impedance (|Z|) are used, containing the previously described ohmic resistance plus reactance (X), which results from AC flow through capacitors and inductors driving the phase shift between voltage and current [187].

Applicable in AC circuit: $|Z(f)| = \sqrt{R^2 + X(f)^2}$ (3)

$$\varphi = \arctan\frac{X}{R} \quad (4)$$

When performing impedance measurements on intact cells, due to the characteristics of their membrane, cells act as a parallel connection of resistor and capacitor. Here, resistance represents the opposition to current flow, whereas capacitance (C) describes the separation of electric carriers at the insulating bi-layer of the cell membrane that causes polarization of the cell. Thereby X is dominated by the capacitive properties of the cell membrane.

$$X(f) \approx (2 * Pi * f * C_{cell})^{-1} \quad (5)$$

Since X is frequency dependent, variation of the measurement frequency enables study of different functional and structural properties of the cell. The ECIS device measures both R and X, allowing calculation of |Z|, C and φ. In this chapter, ECIS technology is used to real-time monitor and measure the effects of the different NPs dispersions on differentiated Caco-2 cells and cellular monolayer of HePG2 cells. These results allow to extract conclusions on the effects of these NPs on more complex cellular systems.

Materials and Methods

NPs synthesis

Details on the fabrication and physicochemical characterization of PC NPs are described in the previous chapters. PET1 NPs are fabricated following the method described by Magrì et al. [18]. For both cases, the dispersants were separated from the NPs through the filtration process as described in Chapter III. For the fabrication of PET2 NPs, PET powder from milled plastic water bottles was treated with hydrochloric acid 50% v/v in Milli-Q® water. The dried powder was dissolved in 1,1,1,3,3,3-Hexafluoro-2-propanol (HFIP) at the concentration of 2 mg/mL, and then the NPs were developed through a modified flash nanoprecipitation protocol [96]. Briefly, 5 ml of HFIP solution of PET (2 mg/mL) was added dropwise to 50 mL of a water solution of sodium cholate 10 mg/mL under mild stirring. HFIP was removed through rotary evaporation and then NPs were washed twice with Milli-Q® water to remove the excess of sodium cholate. For the washing steps, centrifugation was performed at 13000 g for 3 min. The NPs suspension in Milli-Q® water was stored at 4 °C. A solution of sodium cholate hydrate 1 mg/mL was used as respective “dispersant”.

Morphological and chemical characterization of NPs

DLS, TEM and XPS analysis of the PET2 NPs are performed following the same procedure previously described for the PC NPs. PET1 NPs were amply characterized by Magrì et al. [18].

Cell culture conditions

Human hepatocellular carcinoma cells (HePG2) were purchased from LGC standards (Cat HB-8065™, lot number 62591368) and cultured in complete culture medium, composed of Roswell

Park Memorial Institute (RPMI) 1640 medium supplemented with 10% (v/v) Fetal Bovine Serum (FBS, North America Origin), 0.5% (v/v) penicillin/streptomycin and 6 mM L-glutamine. Human colon adenocarcinoma Caco-2 cells were purchased from Sigma-Aldrich (Cat 86010202, lot number 09C004) and cultured in complete culture medium, composed of Dulbecco's Modified Eagle Medium (DMEM) high glucose (4500 g/L) supplemented with 10% (v/v) Fetal Bovine Serum (FBS, North America Origin), 0.5% (v/v) penicillin/streptomycin, 12 mM L- glutamine and 1% (v/v) non-essential amino acids. All cell culture reagents were purchased from Life Technologies, Italy. For routine culture, cells were maintained in a sub-confluent state under standard cell culture conditions in a humidified incubator (37 °C, 5% CO_2, 95% humidity) (Heraeus Thermo Fisher®, Belgium). For HCS experiments, RPMI and DMEM were used without phenol red.

Cytotoxicity Evaluation by colorimetric assays

Cell culture and NPs exposure

NPs cytotoxicity was firstly evaluated *in vitro* using two colorimetric assays, the lactate dehydrogenase (LDH) release and the 3-(4,5-Dimethylthiazolyl-2)-2,5-diphenyltetrazolium bromide (MTT) reduction test, on HepG2 cells. Cells were plated in 96-well cell culture plates (Corning Inc., Corning, NY, USA) at a density of 5 x 10^4 cells/well and allowed to adhere for 24 h. Cells were then exposed to the NPs (1, 10, 20, 40 or 80 µg/mL) for 24 or 48 h. A negative control (medium) and a positive control (Triton 0.1%) were included. For each type of NP dispersion (80 µg/mL), the dispersant was also assessed and tested. At the end of the exposure time, images of cell morphology were taken with an Aziovision Microspcope (at 10x).

Lactate dehydrogenase (LDH) release assay

After each time point, 50 µL of supernatant was transferred in a new plate for measuring LDH release, using the BioVision LDH-cytotoxicity colorimetric kit (cat. K311, BioVision, Inc., Milpitas, CA, USA) according to the manufacturer's instruction. The absorbance was measured at 490 nm by the EnSpire® Multimode plate reader (Perkin Elmer) using a reference wavelength of 680 nm. Data are expressed as % of total LDH release and reported as mean ±SD. Three independent experiments were performed in triplicates.

Cell viability assay

After the removal of the supernatant for LDH assay, MTT [3-(4,5-dimethylthiazol-2-yl)-2,5-diphenyl-2H tetrazolium bromide] (Sigma-Aldrich, Inc.) was added to the cells in fresh complete culture medium at a final concentration of 250 µg/mL. After 4 h of incubation at 37 °C the supernatant was removed, the precipitated formazan crystals were dissolved in 200 µL RPMI (Sigma-Aldrich, Inc.) followed by 50 µL of glycine buffer (0.1 M glycine with 0.1 M NaCl in MilliQ water). The absorbance was measured at 570 nm by the EnSpire® Multimode plate reader (Perkin Elmer) using a reference wavelength of 680 nm. Data are expressed as % of mitochondrial activity and reported as mean ±SD. Three independent experiments were performed in triplicates.

HCS assay

Cell culture and NPs exposure

HepG2 and Caco-2 cells were plated in Corning® 96-well black plates at a density of 1 x 10^4 cells/well and 5 x 10^3 cells/well respectively allowing adhering for 24 h. For experiments with differentiated Caco-2 cells, a seeding density of 8 x 10^4 cell/well was used. Cells were maintained for 21 days in phenol red free complete medium and the medium was replaced three times/week. After complete differentiation at day 21 [188], cells were exposed to NPs (10, 20, 40 or 80 µg/mL) for 24 or 48 h. Negative control (medium), two different positive controls (Valinomycin 900 nM, $CdCl_2$ 50 µM) and the NPs dispersants (obtained as previously described) were also included in the study. Three independent experiments have been performed and each condition was run in triplicate.

Incubation of fluorescent staining and HCS imaging

The cells were exposed to NPs at the concentrations of 10, 20, 40 or 80 µg/mL and compared to negative and positive controls. After each time point, cell staining and fixation according to the Mitochondrial Health Kit (Invitrogen, Thermo Fisher) protocol were performed, allowing for simultaneous quantitative measurements by high content analysis of two cell health parameters in the same cell: mitotoxicity and cytotoxicity. In particular, the Mitochondrial Health Kit was used to stain the nuclei (Hoechst 33342), the cell membrane (Image-iT® DEAD Green™ viability stain) and the mitochondrial membrane (MitoHealth stain). After the staining and fixation the imaging analysis is performed by the IN Cell analyzer 2200 (GE Healthcare, Boston, MA, USA) to acquire image in high-throughput mode. Nine fields per well were imaged with a 10x objective and an average of 2000 objects/field was counted for the analysis. To better understand the information obtained using this staining kit, the study on the effect of the Valinomycin treatment of HeLa cells is presented in **Figure 35**. In particular, the MitoHealth stain accumulates in mitochondria in live cells proportionally to the mitochondrial membrane potential (**Figure 35**, bottom panels). Cytotoxicity is measured with the Image-iT® DEAD Green™ viability stain. The Image-iT® DEAD Green™ viability stain has a high affinity for DNA and forms highly fluorescent and stable dye-nucleic acid complexes; it is non-fluorescent when not bound to DNA. Staining of nuclear DNA cannot occur in live cells due to the impermeability of the cell membrane for the stain. Treatments leading to serious cell injuries, including cell membrane permeability, allow entry of the stain. This property enables the discrimination of dead cells with Image-iT® DEAD Green™ viability stain (**Figure 35**, centre panels). Hoechst 33342 stains nuclear DNA in live and dead cells (**Figure 35**, top panels) (HCS Mitochondrial Health Kit Protocol (Invitrogen)).

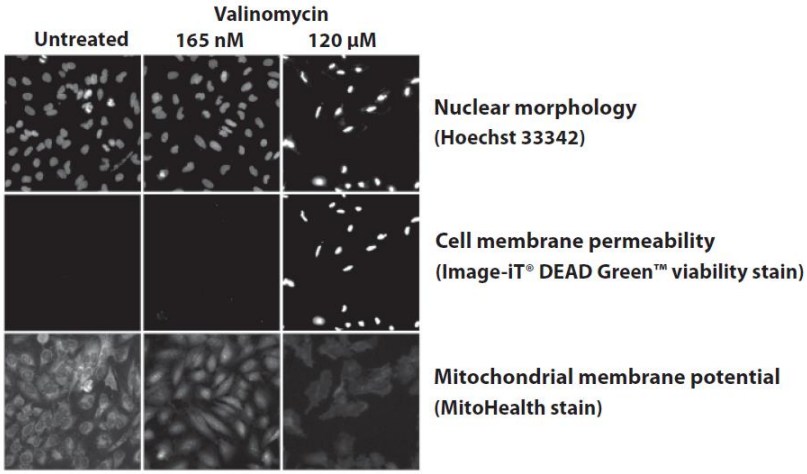

Figure 35. Imaging of mitotoxicity and cytotoxicity of valinomycin in HeLa cells using the HCS Mitochondrial Health Kit (HCS Mitochondrial Health Kit Protocol (Invitrogen)).

HCS data analysis

IN Cell Developer Toolbox 1.9.2 from GE Healthcare (Boston, MA, USA) was used for data analysis. Data were normalized to the negative control (untreated cells) and expressed as average of three independent experiments ± SD. Data were graphical represented using Origin Pro version (2018).

ECIS set up procedure

The monolayer of HePG2 cells and differentiated Caco-2 cells were obtained after plating HePG2 and Caco-2 cells in 96-wells ECIS disposable arrays at a density of 8 x 104 cells/well and maintaining them for 21 days in complete medium, which is exchanged three times/week [188]. The Electric Cell-substrate Impedance Sensing (ECIS, Applied BioPhysics, Inc, NY) was used to monitor in real-time electrical changes. At complete cellular differentiation, the medium was replaced with fresh medium (controls) or with medium containing NPs at the concentrations of 10, 20, 40 or 80 µg/mL. Dispersants were also included as for the highest NP dose tested (80 µg/mL). Each experimental condition was tested in triplicate. After 48 h, treatments were removed and cells were maintained for 12 days in fresh complete culture medium for recovery, during which medium was regularly replaced every 3 days. Cells were then exposed to a second treatment as previously described. As last, Triton (0.1%) was added to each well and used as reference (positive control). The data were collected and analysed by ECIS Zθ software (ECISTM v1.2). Origin Pro version (2018) was used for data representation.

Immunocytochemistry analysis

8×10^3 HePG2 and Caco-2 cells were seeded on a BD FalconTM Chamber polystyrene Vessel (Bedford, USA). Thus, cells were exposed to PC, PET1 and PET2 NPs at 10 µg/mL for 24 h and 48 h. At the end of the incubation time, cells were washed twice in PBS, fixed with 4% (v/v) paraformaldehyde and permeabilised with 0.05% (v/v) Triton-X (Sigma–Aldrich) in PBS (v/v) for 20 min at 25°C. After that the permeabilizing solution is removed and cells are washed 3 times with 0.05% Tween-20 PBS (v/v) and stained. Staining was done with antibody against SNX5 (Rb

Cat. AB83750, Italy, dilution 1:1000). Antibody was diluted in 3% (w/v) BSA in PBS. After removal of the primary antibody, cells were washed three times with 0.05% (v/v) Tween-20 in PBS and stained with the second Ab Alexa Fluor® 546. In addition cells were also stained with Alexa Fluor® 488 phalloidin (Invitrogen, Cat A12379, Italy) for F-actin staining. The nuclei were counterstained with a Hoechst 33342 dye (Dako, Italy). Images were acquired with an Axiovert 200 M inverted microscope equipped with ApoTome slide module and Axiovision 4.8.2 software (Carl Zeiss; Jena, Germany), using 40×/1.0 objective lens.

Statistical Analysis

Data are reported as means ± standard deviations (SD) of three independent experiments. Statistical significance of differences is indicated by p values, calculated using one-way ANOVA, Origin 2018. EC_{50} values were calculated to Graph Pad Prism by fitting a sigmoid curve (log (inhibitor) v.s. normalised response – variable slope).

Results and discussion

Physical and morphological characterization of NPs

In this study, the toxicological evaluation of three different types of NPs are performed: PC and PET1 NPs obtained by laser ablation and PET2 NPs by chemical synthesis. The NPs formed by laser ablation were previously characterized (Chapter III for PC NPs, and Magrì et al., 2018 [18] for PET1 NPs). In this paragraph, the characterization of the colloidal PET2 NPs is performed following the same methodologies previous reported (Chapter II and Chapter III) and presented in comparison with the other two types of NPs in order to show the difference in terms of size, dispersion and chemical properties. As shown in **Figure 36**, the particle size distribution and PDI, performed by DLS, show that the PET2 NPs D_H is of 88.9 ± 2.0 nm with a PDI of 0.080, showing a higher monodispersity and slightly higher mean size than the laser ablated NPs (PC NPs: D_H =47.4 ± 3.0, PDI = 0.190; PET1 NPs 57.7 ± 9.0 nm, PDI = 0.196). Batch-mode DLS was repeated over time during the whole study to monitor NPs stability, proving the all types of NPs remained stable for more than 6 months in Milli-Q® water. In addition, all NPs resulted stable in complete RPMI and DMEM media for up to 48 hours. TEM images (**Figure 37**) corroborate in terms of size evolution the DLS results, showing an almost spherical shape for all the NPs, with an irregular surface in case of the laser ablated ones.

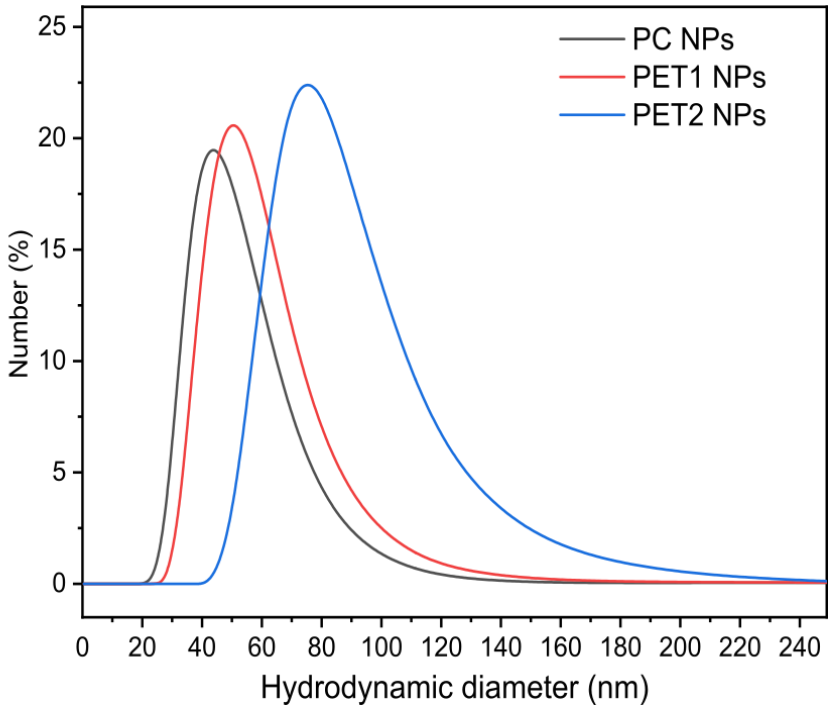

Figure 36. D_H distribution of PC NPs (black), PET1 NPs (red) and PET2 NPs (blue).

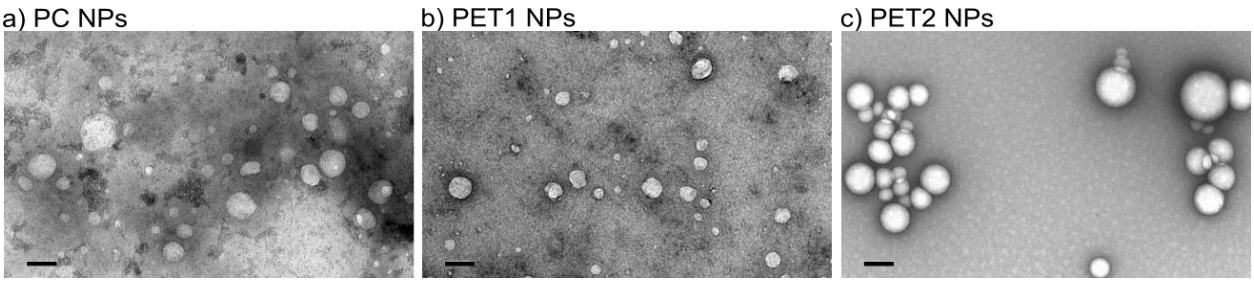

Figure 37. Morphology of the a) PC NPs, b) PET1 NPs and c) PET2 NPs by TEM. Scale bar is the same in each panel and represents 100 nm.

Moreover, the surface chemistry characterization performed by XPS showed for PET2 NPs a less relevant oxidation on the surface than the laser ablated NPs. By the survey spectra analysis (**Figure 38**), the O/C ratio is lower in the PET2 NPs (O/C= 0.31 ± 0.03) compared to the PET1 NPs (O/C= 0.58 ± 0.10) and PC NPs (O/C= 1.53 ± 0.04) demonstrating also a lower presence of the oxygen element on the surface of both PET NPs compared to the PC NPs (stoichiometric ratios for bulk PC: $O/C_{PC\ stoich}$= 0.19 and for bulk PET: $O/C_{PET\ stoich}$= 0.40). The percentage of the respective elemental compositions of survey spectra are represented in the **Table 9**.

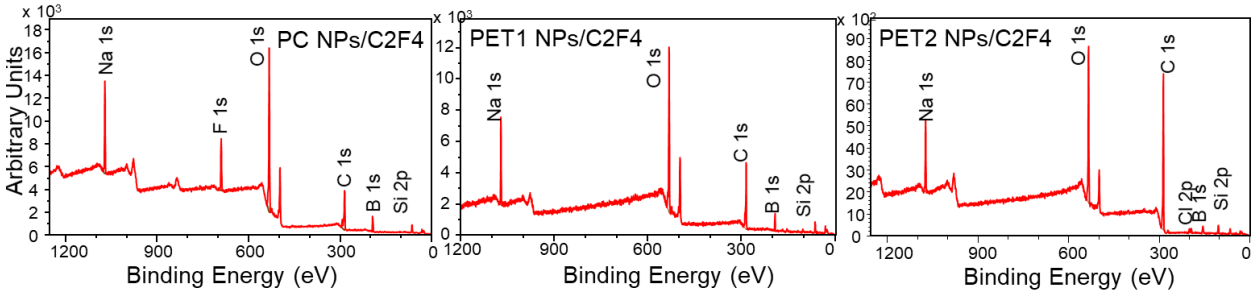

Figure 38. Survey XPS spectra of the three different NPs with the respective elemental composition.

	Binding Energy	**PC NPs/C_2F_4**	**PET1 NPs/C_2F_4**	**PET2 NPs/C_2F_4**
C 1s	284.7 eV	29.66%	57.59%	66.71%
O 1s	532.2 eV	45.37%	33.72%	20.70%
Si 2p	102.2 eV	0.40%	2.87%	3.29%
B 1s	192.7 eV	14.52%	10.39%	2.94%
Cl 2p	197.8 eV			0.75%
Ca 2p	347.3 eV			
F 1s	689.7 eV	8.9%		
Na 1s	1071.16 eV	10.05%	3.49%	5.61%

Table 9.Percentage of respective elemental composition of survey spectra for the three types of NPs. F and Na signals are attributed to fluorine and sodium respectively.

The deconvolution of the C1s spectrum (**Figure 39**) shows the different carbon based chemical components present in the three NPs, and their corresponding percentage is presented in **Table 10**. The contributions located at 284.6 eV and 285.1 eV, which correspond respectively to the aromatic and aliphatic C–H/C–C groups, are higher in the PET2 NPs (82.9%) compared to both laser ablated NPs (PC NPs: 58.4% and PET1 NPs: 58.9%). The peak at 286.3 eV is due to the presence of the C–O–C/ C–OH, and is higher in the PC NPs (17.8%) and PET1 NPs (16.8%) compared to colloidal PET2 NPs (12.8%). Furthermore, in the PET2 NPs a decrease of the O=C–O component (represented by the peak at 288.7 eV) is clear (PET2 NPs: 4.3%; PET1 NPs: 10.9% and PC NPs: 8.0%). The peak at 287.7 eV representative of the C=O group appears only in the laser ablated NPs (PET1 NPs: 3.9% and PC NPs: 3.3%). The main difference between the two laser ablated NPs are the contribution of the $O=C(-O)_2$ group in the PC NPs at binding energy 290.4 eV and the satellite shakeup feature (related to delocalized C-C bonds in aromatic rings) at 291.3 eV in PET1 NPs.

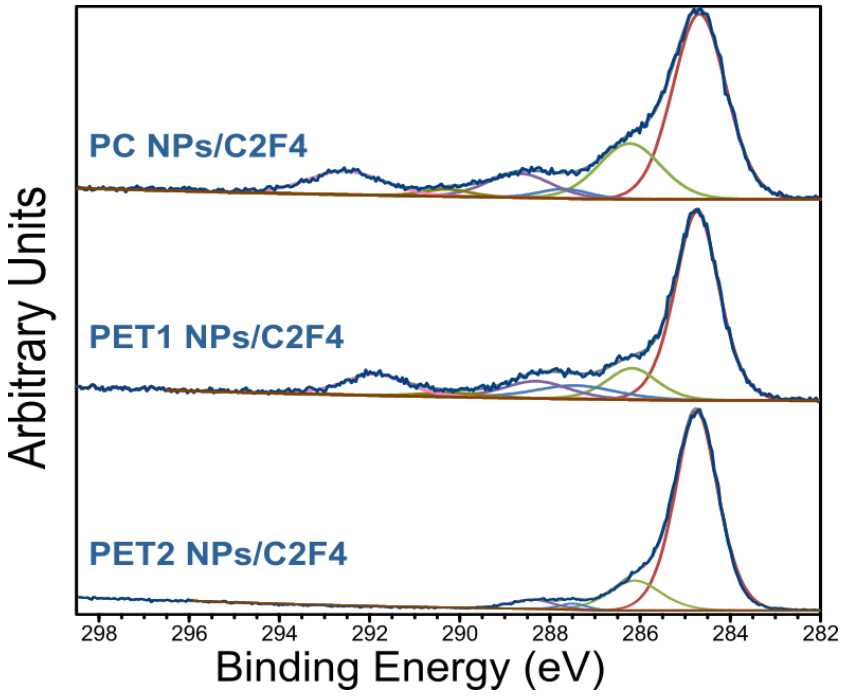

Figure 39. XPS C1s high resolution spectra of the three different NPs with the corresponding deconvolutions. NP dispersion drop-casted on Teflon (C_2F_4) substrate.

C 1s	Binding Energy	PC NPs/C_2F_4	PET1 NPs/C_2F_4	PET2 NPs/C_2F_4
C-C (ar)	284.6 eV	58.38%	58.92%	82.94%
C-C (al)	285.1 eV			
C-O-C, C-OH	286.3 eV	17.79%	16.84%	12.81%
C=O	287.7 eV	3.27%	3.96%	
O=C-O	288.7 eV	8.02%	10.92%	4.25%
O=C(-O)2	290.4 eV	2.02%		
C-C sh.-up (I)	291.3 eV		2.84%	
C_2F_4	292.5 eV	10.52%		

Table 10. Percentage of the corresponding deconvolutions of the C1s spectra. The C_2F_4 signal is attributed to Teflon substrate.

The **Figure 40** gives an overview of the main difference of the NPs compared with the starting material (pristine PC and PET). The ratio of the oxidized carbon bonds with the aliphatic/aromatic C-C bonds, increases in the laser ablated NPs, (more significant increase at the PC NPs), compared with the starting material. On the other hand, chemical synthetized NPs show a drastic decrease on this ratio compared with pristine PET, indicating that the chemical synthesis does not introduce additional oxidized species on PET2 NPs surface. Moreover, in both types of ablated NPs, a new oxidized functionality (C=O bond) is created and the C-C shakeup features decrease in PET1 NPs compared to the pristine bulk film.

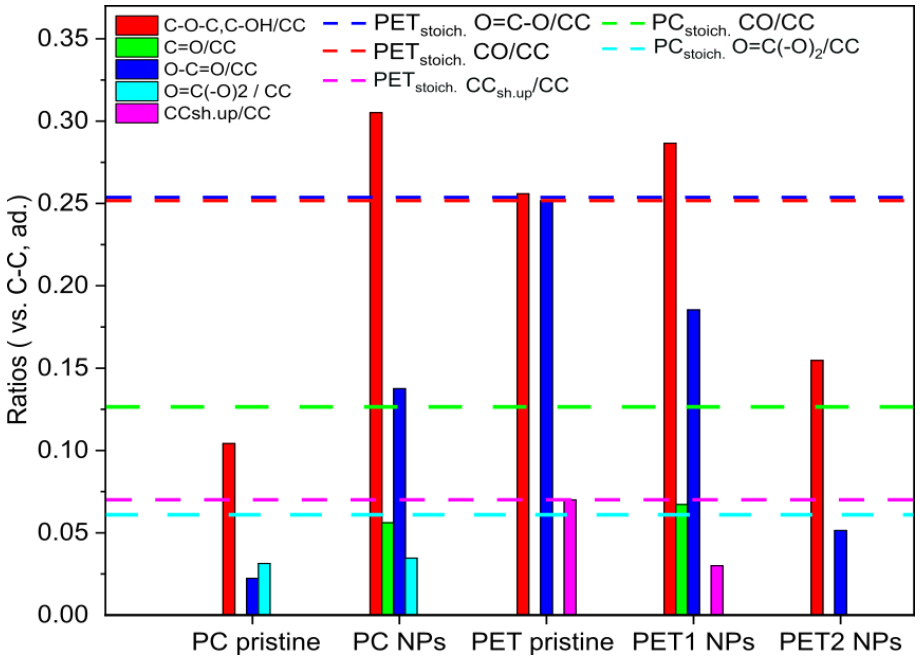

Figure 40. Atomic bonding distribution from XPS C1s spectra analysis for all NPs types, and comparison with the pristine polymers (PC and PET bulk films).

As shown in the previous chapter, the pulsed laser ablation of solid polymeric films in water results in the formation of NPs with similar characteristics as the ones expected to exist in the environment, in terms of surface and shape irregularity, broad size distribution and chemistry. On the other hand, colloidal PET2 NPs are more monodispersed and are slightly bigger, with spherical shape, smooth and homogeneous surface while their surface chemistry is indicative of the bulk PET chemical composition, in contrary to the more oxidized character of the laser ablated NPs, and far away from the characteristics of the NPs expected to be found in the environment. For this reason, it is interesting to investigate the toxicological effects of these three different NP dispersions. To do so, three different in vitro technologies are adopted as previously discussed.

Toxicological assessment by colorimetric assays

The NPs toxicological assessment was performed on *in vitro* models, which allows the identification of the hazardous potential of xenobiotic materials. Considering that diet is the main route of human exposure to NPs [189], the biological impact was initially studied by investigating NPs interactions on HePG2 cells, which mimic the hepatic system (excretion route), and Caco-2 cells, which mimic the intestinal epithelial cells. Toxicological assessment was performed according to ISO guide ISO 10993-22 (*Biological evaluation of medical devices – Part 22: Guidance on nanomaterials*), which indicates LDH release and MTT reduction as the standard methods to address the biological evaluation of nanoparticulate materials. Cells were exposed to NPs at different concentrations spanning from 10 to 80 µg/mL, for 24 or 48 h. In addition, the supernatant of Caco-2 cells, after different treatments, on ECIS experiment (shown in the last

paragraph) is also analyzed by LDH assays. The LDH negative results, shown in the **Figure 41**, indicate that this typology of LDH assay is not suitable to assess the toxicity of the NPs under investigation. This is most probably due to interferences between the NPs and the LDH assay reagents or with the assay readout, as already reported in literature [165–168].

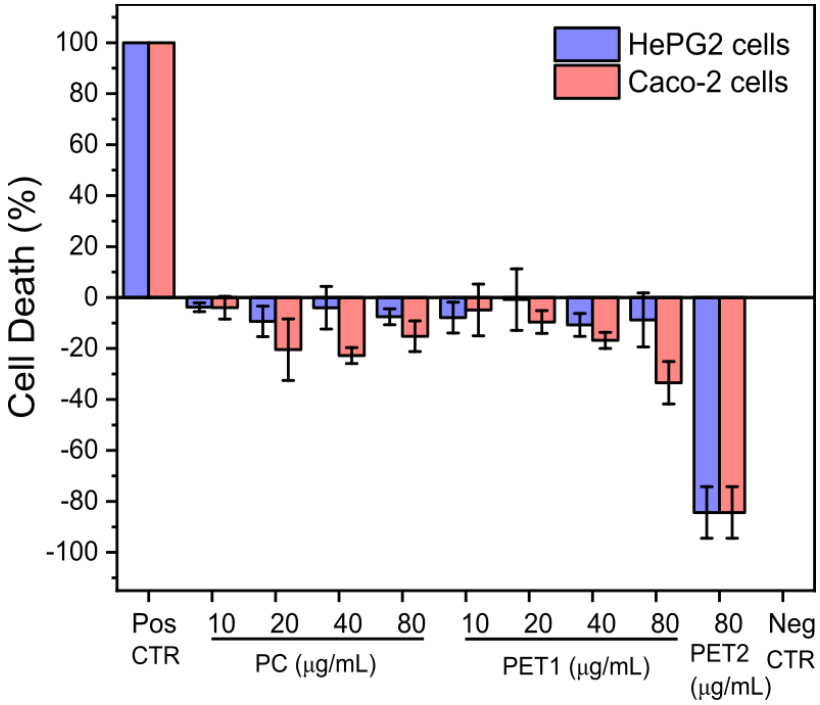

Figure 41. HepG2 and Caco-2 cell viability after exposure to NPs at the concentration of 10, 20, 40, 80 µg/mL for 24 or 48 h. In the case of PET2 data are represented only at 80 µg/mL (LDH assay). Data are reported as % of cell death (average of three independent experiments ± SD).

On the contrary, MTT assay showed to work despite the high variability across replicates. In fact, MTT results on HePG2 cells exposed to the different NPs are reported in **Figure 42**. Statistical analysis did not indicate significant toxicity for PC NPs at all doses and time points tested, although a high standard deviation was observed among replicas. Furthermore, PET1 and PET2 resulted toxic only at the highest dose (80 µg/ml) and only at 24 h, confirmed by the morphological analysis (**Figure 43**). Studying the effect of the dispersant, obtained after the removal of NPs through ultrafiltration, it is shown that there is a significant toxic effect of the PC dispersant at both time points considered, while in the PET cases no effects on the cell viability were observed (**Figure 42**). On the other hand, no morphological changes were evident in the case of PET2 exposed cells at all doses tested at both time points considered (**Figure 43**).

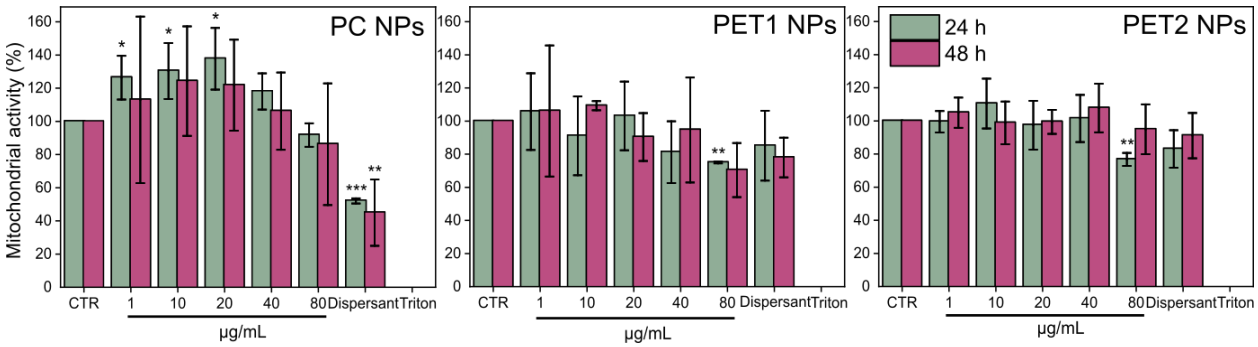

Figure 42. Mitochondrial activity of HePG2 cells after exposure to NPs at the concentrations of 1, 10, 20, 40, 80 µg/mL for 24 or 48 h (MTT assay). Data are reported as average of three independent experiments ± SD. $p < 0.001$, $p < 0.01$ and $p < 0.05$ are reported (***, ** and * respectively), calculated versus CTRL (one-way ANOVA).

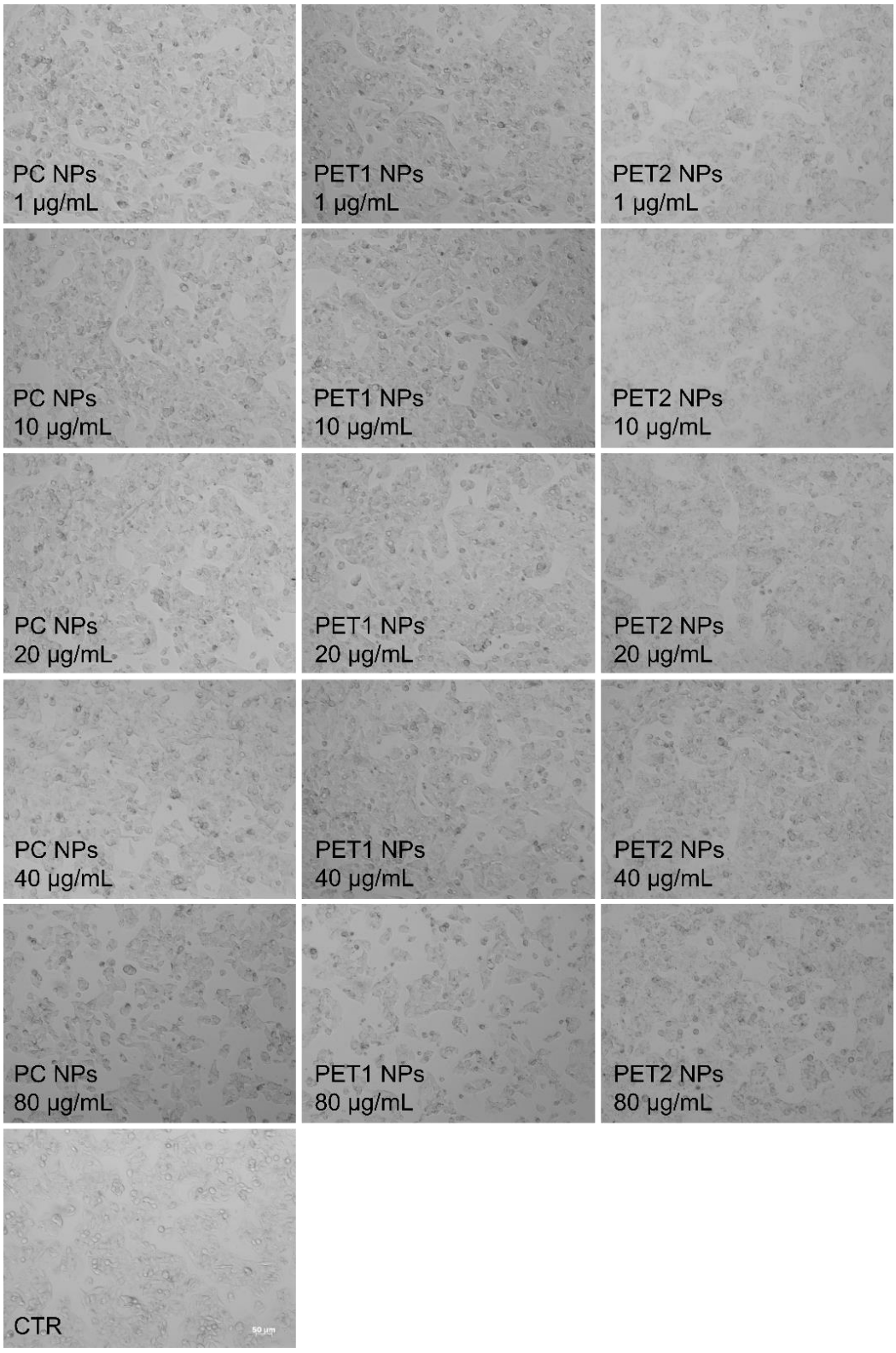

Figure 43. Representative morphological images of HePG2 cells after different treatments for 24 h. Scale bar at 50 µm for all images.

Cytotoxicity evaluation by high content screening (HCS)

To overcome the limitations of the classical colorimetric methods that we observed in the case of this LDH assay, as well as the high variability observed for MTT experiments, cytotoxicity was also evaluated by HCS analysis on two *in vitro* cell models. For this, the nuclei, the cell membrane and the mitochondrial membrane were stained in order to evaluate changes in cell viability, cell membrane permeability and mitochondrial membrane potential, respectively. **Figure 44** and **Figure 45** illustrate the HePG2 and Caco-2 cells viability after exposure to different doses of NPs or to the dispersant. As shown, the reduction of cell viability is significant for both PC and PET1 NPs at nearly all doses tested, with PC resulting more toxic than PET1. On the other hand, PET2 did not affect the cell viability, except the case of HePG2 cell line, after 48 h of treatment with the highest NPs dose (**Figure 44**). Concerning the dispersant component, it is observed a significant toxicity of the PC and PET1 dispersants at both time points considered, while no toxicity was observed in the case of PET2 dispersant. **Table 11** reports EC50 values for each type of NPs at 24 and 48 h.

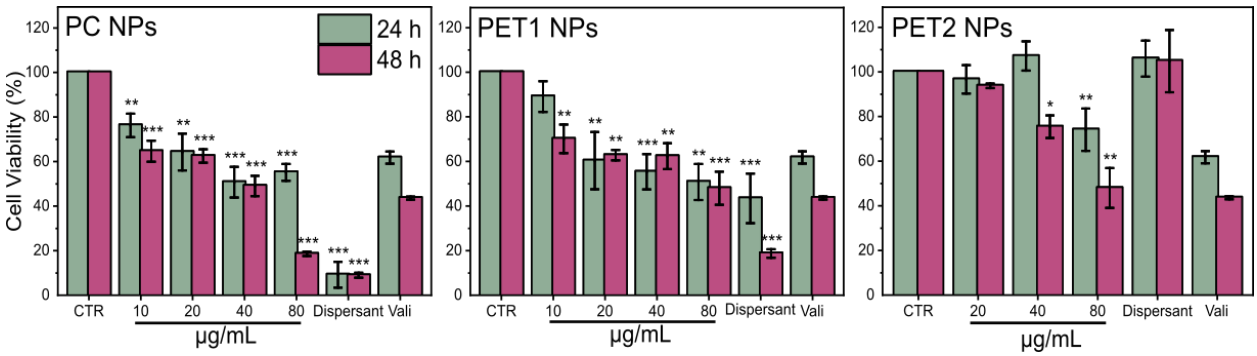

Figure 44. Cell viability of HePG2 cells exposed to different NPs concentrations or to the PC and PET NPs dispersants at 24 or 48 h. Results are expressed as % cell viability compared to the untreated cells. Data are reported as average of three independent experiments ± SD. Valinomycin (900nM) was used as positive controls. $p < 0.001$, $p < 0.01$ and $p < 0.05$ are reported (***, ** and * respectively), calculated versus CTRL (one-way ANOVA).

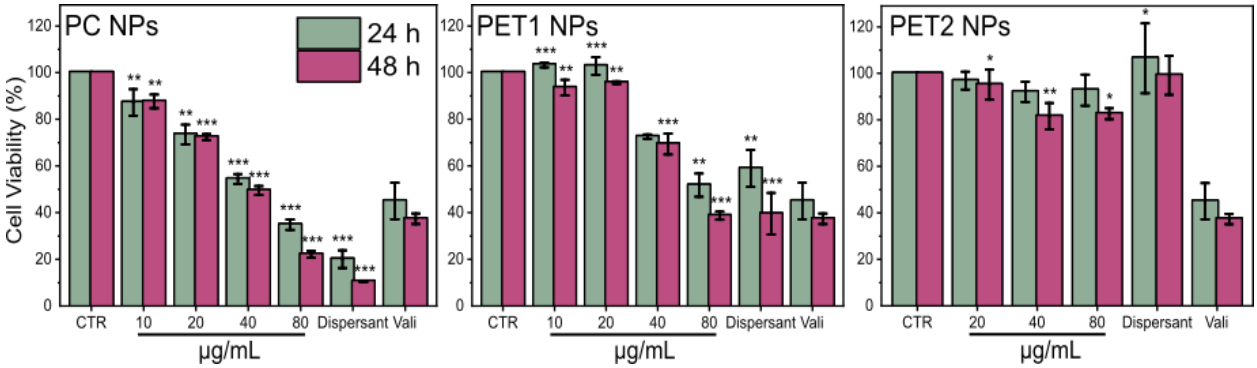

Figure 45. Cell viability of Caco-2 cells exposed to different NPs concentrations or to the PC and PET NPs dispersants at 24 or 48 h. Results are expressed as % cell viability compared to the untreated cells. Data are reported as average of three independent experiments ± SD. Valinomycin (900 nM) was used as positive controls. $p < 0.001$, $p < 0.01$ and $p < 0.05$ are reported (***, ** and * respectively), calculated versus CTRL (one-way ANOVA).

	24 hours	**48 hours**
HePG2 cells	**EC_{50} (µg/mL)**	**EC_{50} (µg/mL)**
PC NPs	73.12	38.15
PET1 NPs	69.03	68.86
PET2 NPs	74.15	48
Caco-2 cells	**EC_{50} (µg/mL)**	**EC_{50} (µg/mL)**
PC NPs	55.31	44.62
PET1 NPs	79.41	40.06
PET2 NPs	92.45	82.12

Table 11. The table reports EC_{50} values (µg/mL) of PC, PET1 and PET2 NPs for HePG2 and Caco-2 cells at 24 or 48 h of exposure.

Results of the effects on the mitochondrial activity on HepG2 cells are reported in **Figure 46** and on Caco-2 cells in **Figure 47.** A reduction of the mitochondrial activity was evident for HePG2 cells exposed to PC NPs at all time points analyzed, whereas on Caco-2 cells, PC NPs resulted significantly toxic only at the highest dose tested. To a lesser extent PET1 NPs, also synthetized by laser ablation, showed a significant reduction of mitochondrial activity at all doses tested on HePG2 cells. In the case of PET2 NPs, reduction of mitochondrial activity was observed on HePG2 cells at 80 µg/mL at both time points, and at 40 µg/mL only at 48h (**Figure 46**). Again, reduction of mitochondrial activity was more limited when PET2 NPs where exposed to Caco-2 cells (**Figure 47**). NPs dispersant was found for HePG2 significantly toxic in the case of PC NPs at both time points considered, whereas PET1 NPs dispersant was found significantly toxic only at 48 h. PET2 dispersant did not result toxic at all conditions tested.

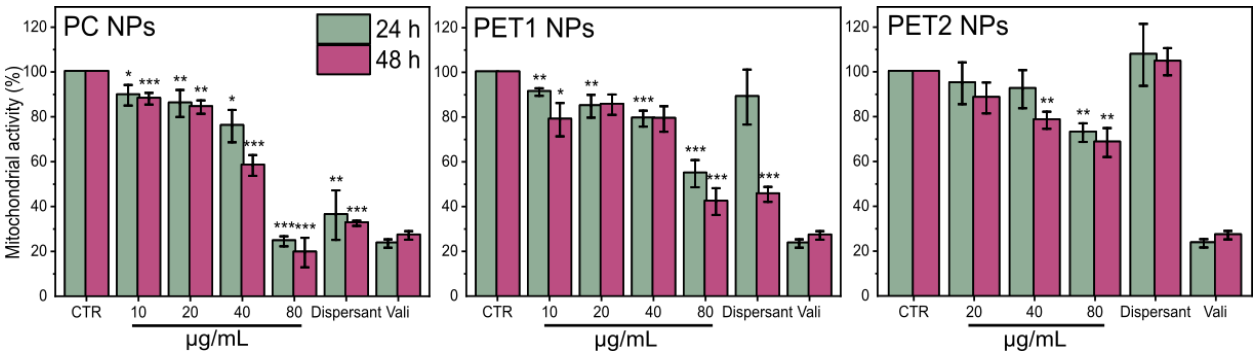

Figure 46. Mitochondrial activity of HePG2 cells exposed to different concentration of PC and PET NPs for 24 or 48 h, measured by HCS. Results are expressed as % mitochondrial activity compared to the untreated cells. Valinomycin (900 nM) was used as positive controls. Data are reported as average of three independent experiments ± SD. $p < 0.001$, $p < 0.01$ and $p < 0.05$ are reported (***, ** and * respectively), calculated versus CTRL (one-way ANOVA).

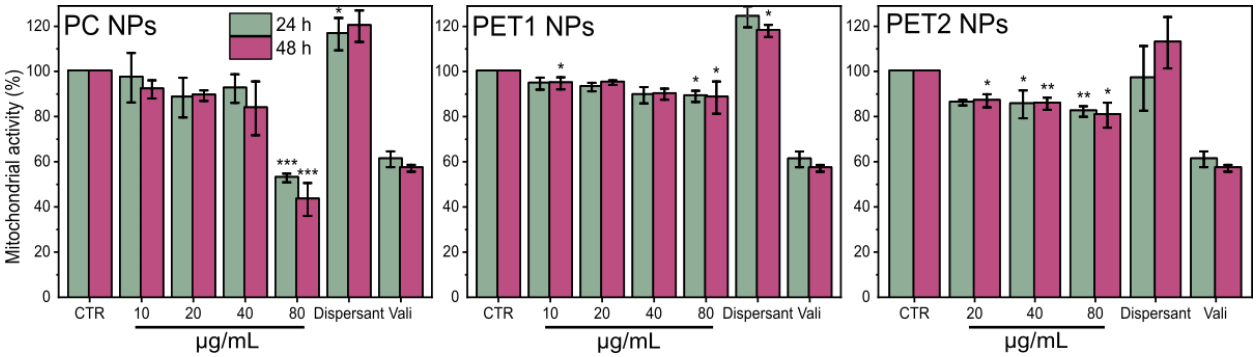

Figure 47. Mitochondrial activity of Caco-2 cells exposed to different concentration of PC and PET NPs for 24 or 48 h, measured by HCS. Results are expressed as % mitochondrial activity compared to the untreated cells. Valinomycin (900nM) was used as positive controls. Data are reported as average of three independent experiments ± SD. $p < 0.001$, $p < 0.01$ and $p < 0.05$ are reported (***, ** and * respectively), calculated versus CTRL (one-way ANOVA).

Data on nuclear size and nuclear intensity were also extrapolated. **Figure 48** shows the effect in HePG2 cells, and **Figure 49** shows Caco-2 cells effect. No notable changes were observed for all NPs and doses tested for both cell lines and at all time points considered. The solid line represents the nuclear size and the dash dot line indicates the nuclear intensity trend.

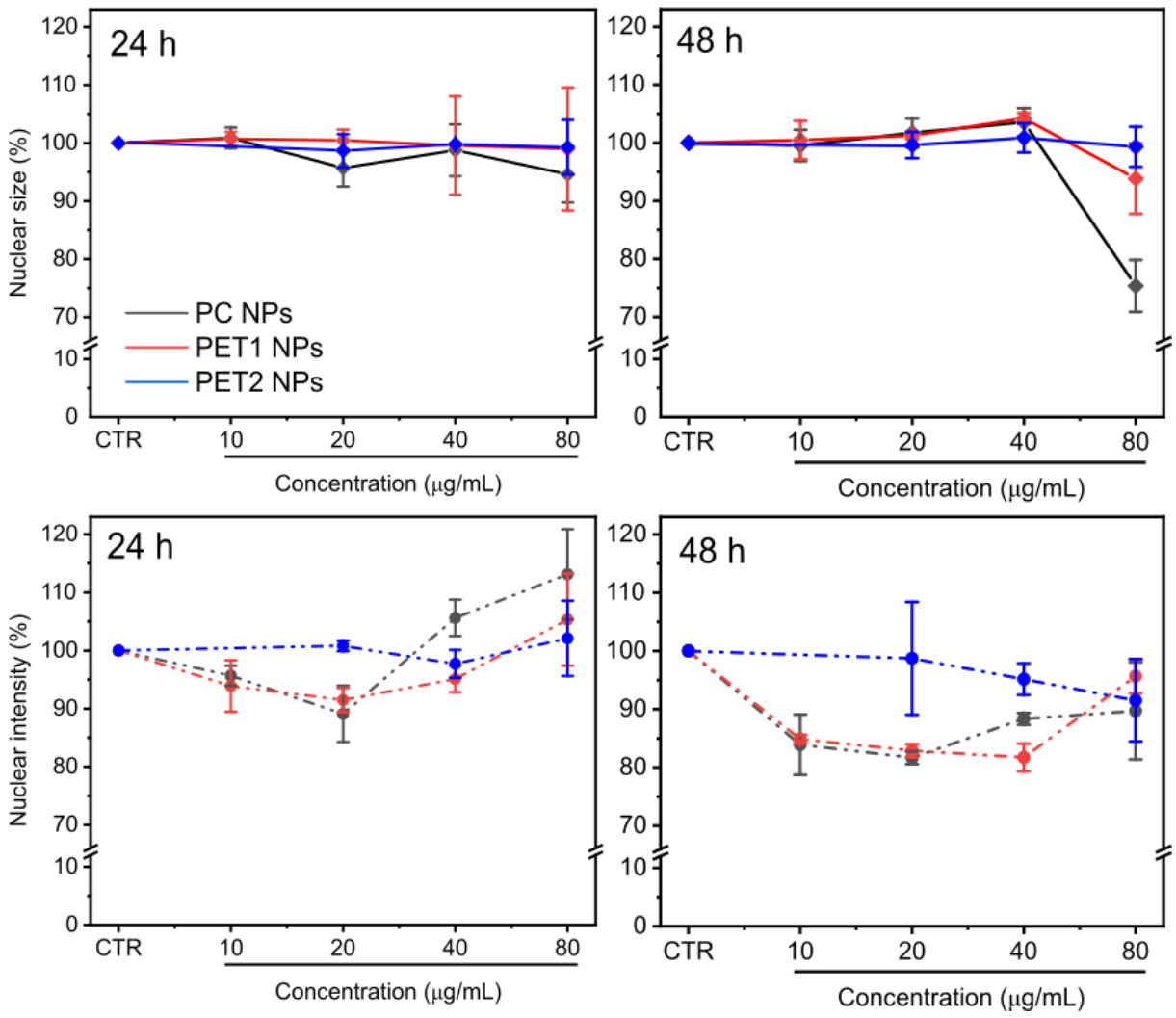

Figure 48. NPs effects on HePG2 cells on nuclear size (top of the panel) and nuclear intensity (bottom of the panel). Cells were exposed to PC, PET1 or PET2 NPs at concentrations between 10 and 80 µg/mL for 24 or 48 h, stained with Hoechst 33342 and analyzed by HCI. Data are expressed as % nuclear effect normalized to the control (untreated cells) and reported as mean of three independent experiments ± SD.

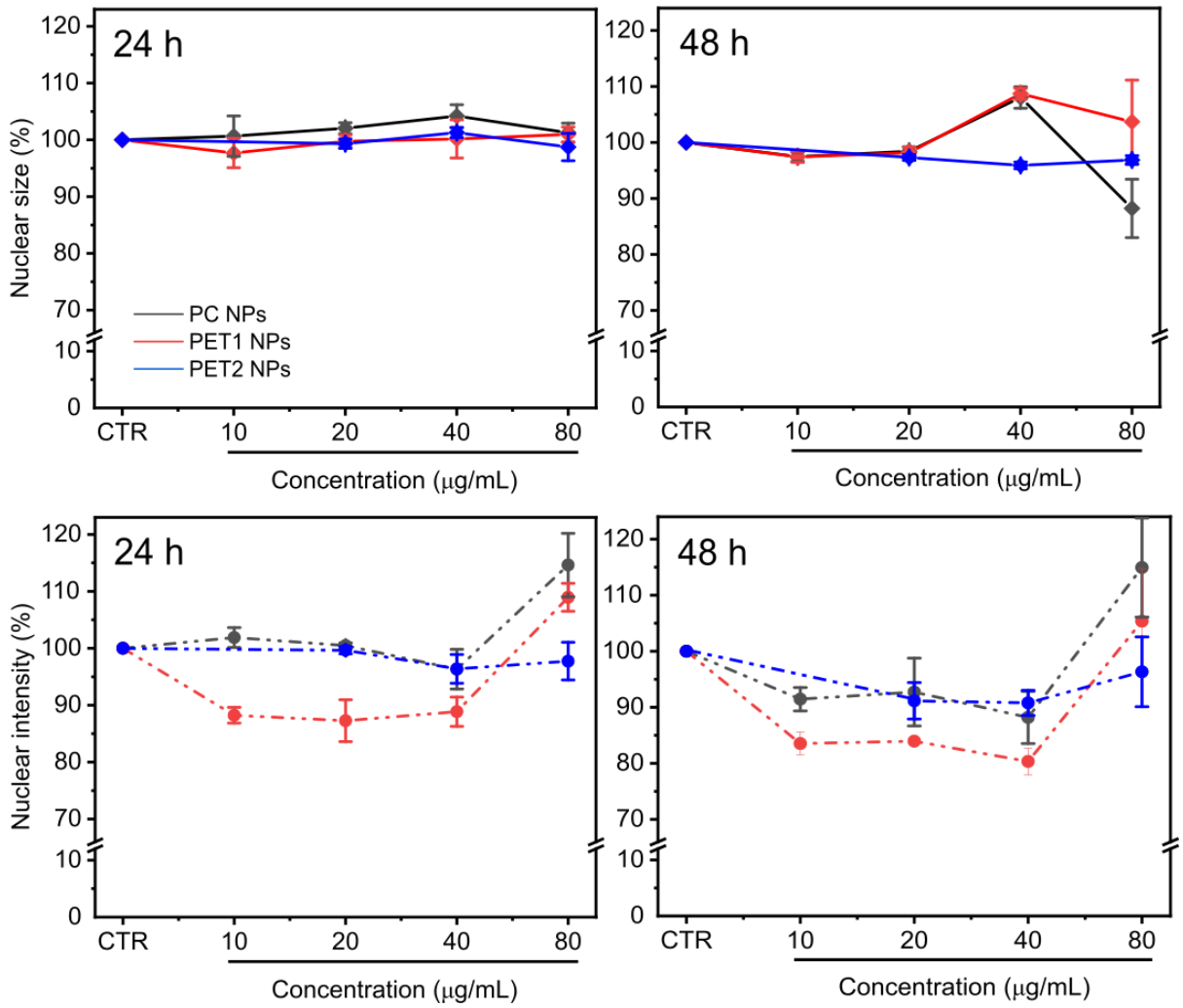

Figure 49. NPs effects on Caco-2 cells on nuclear size (top of the panel) and nuclear intensity (bottom of the panel). Cells were exposed to PC, PET1 or PET2 NPs at concentrations between 10 and 80 μg/mL for 24 or 48 h, stained with Hoechst 33342 and analyzed by HCI. Data are expressed as % nuclear effect normalized to the control (untreated cells) and reported as mean of three independent experiments ± SD.

Moreover, a two-way analysis was performed to monitor simultaneously two different parameters related to cell viability: mitochondrial activity and cell membrane damage. **Figure 50** reports the case of HePG2 cells. As expected, the negative and positive controls are placed on the two opposite sides in the graph, whereas the different NPs concentrations are distributed with a dose response trend between these extremis, especially for PC, indicating an increase of the toxicity at increasing NPs doses. PET2 treatment has not a significant effect. The two-way analysis for Caco-2 cells is reported in **Figure 51**. Data shows that PC NPs at the highest dose tested (80 μg/mL) and PC dispersant has a significant toxicity, with a strong effect on membrane damage and loss of cell mitochondrial activity. PET1 and PET2 treatments have not a significant

effect on mitochondrial activity and cell membrane integrity rather, at low NPs doses, the mitochondrial activity was higher compared to the control.

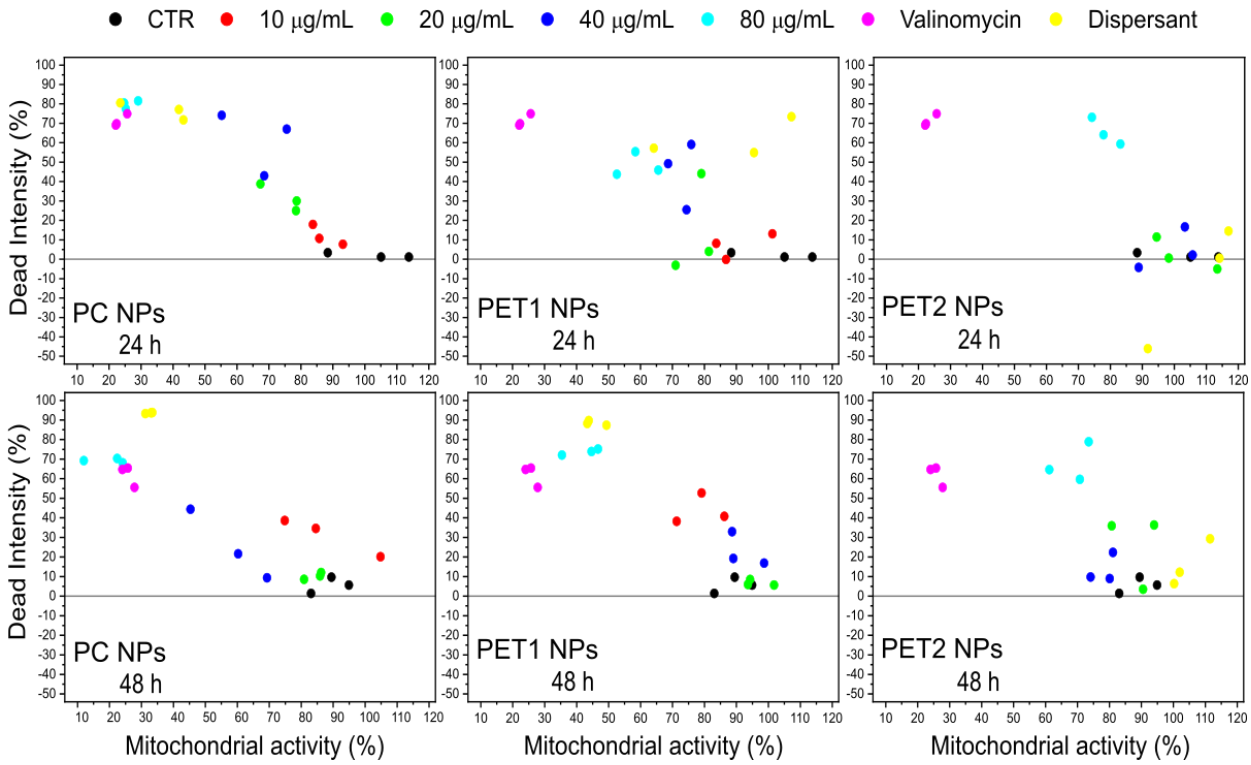

Figure 50. Two-way analysis of HePG2 cells exposed to PC, PET1 or PET2 NPs concentrations between 10 and 80 μg/mL for 24 or 48 h. Valinomycin was used as positive control. Results are expressed in function of two different parameters: mitochondrial activity and cellular membrane damage. Data are reported as average of three independent experiments.

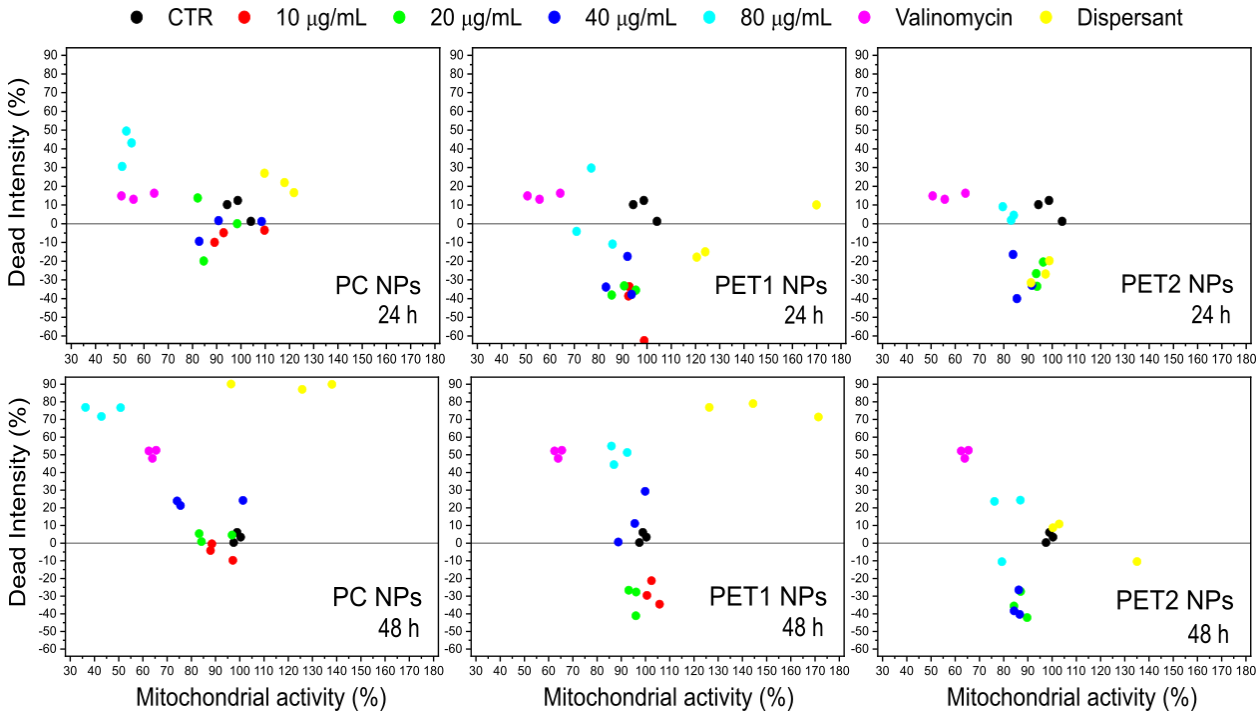

Figure 51. Two-way analysis of Caco-2 cells exposed to PC, PET1 or PET2 NPs concentrations between 10 and 80 μg/mL for 24 or 48 h. Valinomycin was used as positive control. Results are expressed in function of two different parameters: mitochondrial activity and cellular membrane damage. Data are reported as average of three independent experiments.

To conclude, PET1 NPs synthetized by laser ablation have a stronger effect on cell viability, mitochondrial activity, and cellular membrane integrity than the chemically synthetized PET (PET2 NPs). The higher toxicity might be associated with the smaller fragments obtained by the laser ablation method which are not formed in the chemical synthesis. These fragments cause the increase of the polydispersity in the laser ablated NPs, as described in the previous chapter for the PC NPs [190–192]. Overall, PC NPs resulted the most toxic material, showing a stronger effect on the cell viability, mitochondrial activity and on cell membrane damage than laser ablated PET1 NPs, despite having a similar polydispersity. Analysing the NPs dispersant, after separation from the laser ablated NPs, we observed that the PC NPs dispersant is more toxic than the PET1 NPs dispersant. This can be explained considering that the PET1 dispersant does not contain any substances that may affect significant the toxicity results [18]. Specifically, the acetic and formic acids traces present in the water suspension during laser ablation are reduced by Rotavapor treatment. The concentrations result negligible on the cellular effects. On the other hand, these results corroborate with the previous on the HPLC of the PC NPs medium, which contain the low-molecular weight intermediate components deriving from the photo-degradation process of the PC (Chapter III), but also to some smaller NPs fragments that may pass to the dispersant through the filtration process.

To better understand the effects of NPs on a system closer to the intestinal barrier, the effect of the NPs on differentiated Caco-2 cells, a suitable model of the intestinal barrier for *in vitro* toxicology studies, has been studied [188]. Differentiated Caco-2 cells are morphologically similar to enterocytes of the small intestine. They polarize, form a brush border, and show functional tight junctions[170]. Caco-2 cells contribute to a better understanding on perturbations of basic cellular functions. These cells can also mimic the epithelial barrier in vitro. In this case, they allow to investigate the permeability and cellular uptake of xenobiotic as well as the role of transport proteins and metabolism in these processes[170]. For this reason, the toxicological assessment, using differentiated Caco-2 cells, allows having added information on the effects of these typologies of NPs on a system more complex and closed to the tissues in the body. Results are shown in **Figure 52** and **53**, where also the data of undifferentiated Caco-2 cells are also reported for comparison reasons. In the case of differentiated Caco-2 cells, no effects on cell viability and mitochondrial activity were found for all NPs and at all conditions tested. Respective NPs dispersants were also assessed and resulted also no toxic. This result was also confirmed using another orthogonal method: the ECIS, which is based on measuring changes of electrical current on small gold-film electrodes [185,186,193].

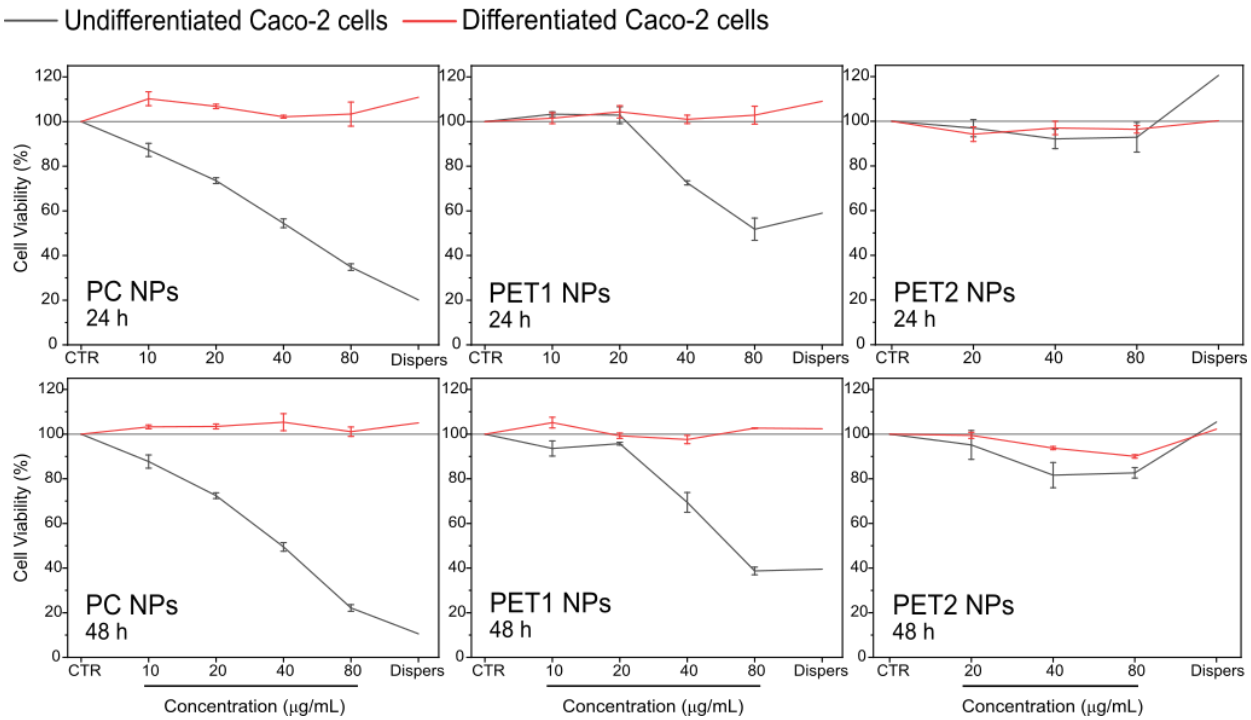

Figure 52. Cell viability of undifferentiated and differentiated Caco-2 cells exposed to different doses of PC, PET1 or PET2 NPs for 24 or 48 h. Data are expressed as % cell viability normalized to the control (untreated cells), and reported as mean of three independent experiments ± SD.

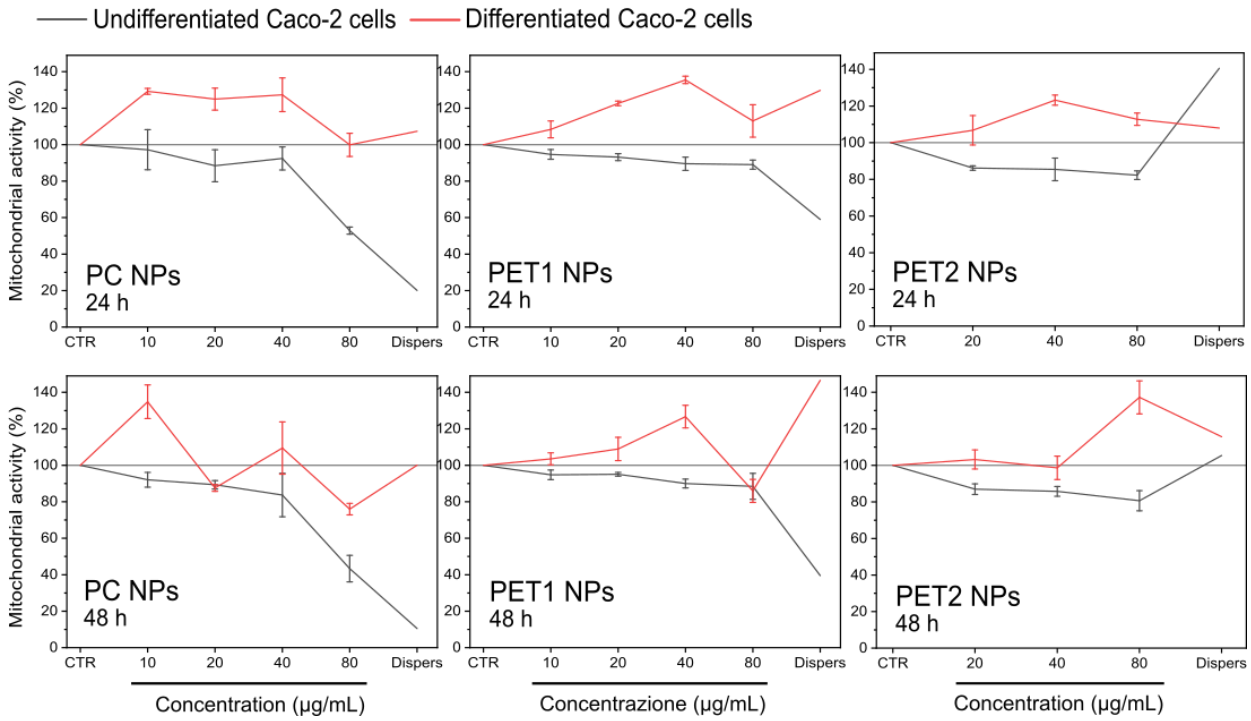

Figure 53. Mitochondrial activity of undifferentiated and differentiated Caco-2 cells exposed to different doses of PC, PET1 or PET2 NPs for 24 or 48 h. Data are expressed as % mitochondrial activity normalized to the control (untreated cells), and reported as mean of three independent experiments ± SD.

Electric cell-substrate impedance sensing (ECIS) technology

To evaluate the toxicity of all three NPs upon long-term exposure, ECIS measurements were performed on monolayers of HePG2 cells and differentiated Caco-2 cells. The cells were exposed twice to NPs dispersions for 48 h, with a recovery period of 12 days between the two treatments. **Figure 54** shows the results obtained for the different doses tested and for each treatment duration (24 and 48 hours). Results indicate that exposure of differentiated Caco-2 cells to NPs does not cause any significant effect in all three monitored parameters. No changes in electrical impedance, which is an indication of cell confluence and tight junctions development, was reported during the whole time monitored (**Figure 54 a**). No effects also on the resistance are shown (**Figure 54 b**) indicating that the NPs do not affect the barrier quality and function. In fact the resistance parameter describes better barrier quality and function, because it neglects capacitive components from membrane, electrode and medium. The capacitance allows monitoring the adhesion, spreading, and proliferation of the cells on the electrode. This component decreases directly proportional to the electrode coverage by the cells and the **Figure 54 c** shows that all the treatments have no effect on the adhesion, spreading, and proliferation of differentiated Caco-2 cells [186,193].

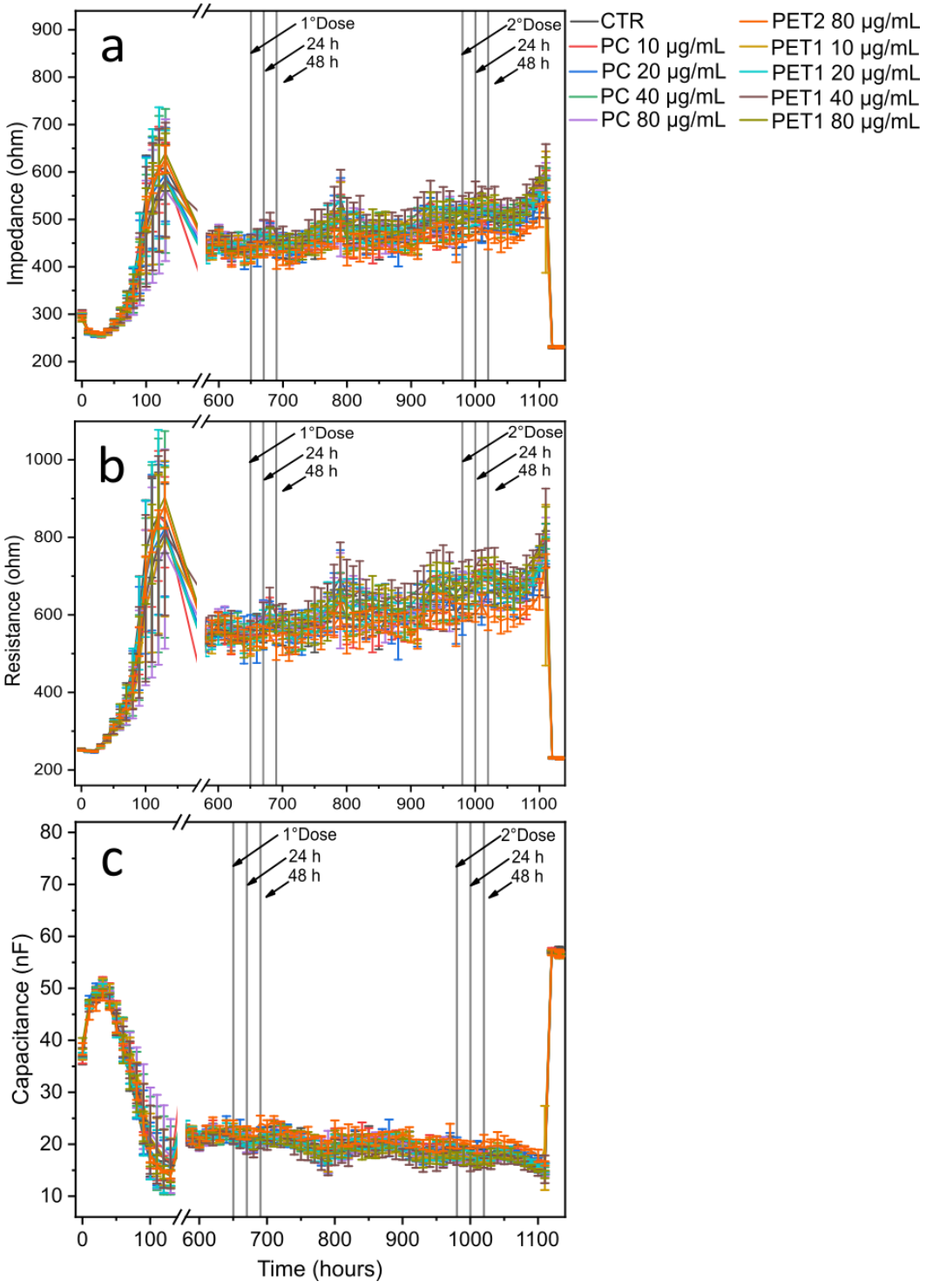

Figure 54. Electrical a) impedance, b) resistance and c) capacitance in differentiated Caco-2 cells. After a recovery period of 12 days, cells were re-exposed for others 48 h to the treatments. At the end of the second treatment, medium was given to the cells and maintained for an additional 48 h. Triton X-100 (0.1%) was then added as positive control.

Similar behaviors were observed also for the HePG2 cells (**Figure 55 a,b,c**), but also after the treatment of the cell monolayers only with the corresponding NPs dispersants as shown in **Figure 56,** where the resistance trend after the different treatments compared to the negative and positive control (untreated and Valinomycin, respectively) are shown. Overall, it is possible to conclude that all the tested NPs do not cause any toxic effects on both types of the differentiated cells. This can be easily explained as on differentiated cells tissue-like system, therefore on a cellular model more resistant to external stress, the NPs do not provoke any effects on the barrier integrity [159,194].

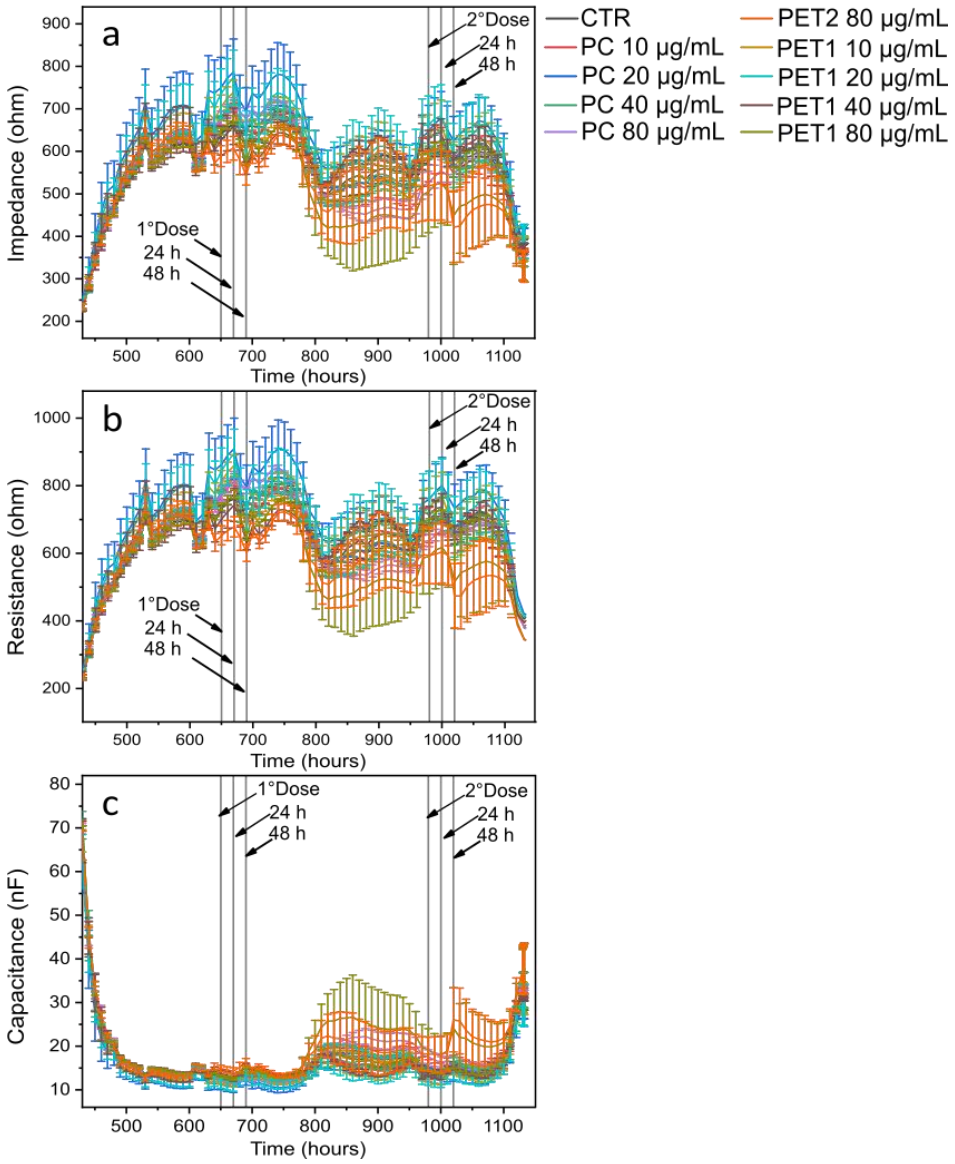

Figure 55. Electrical a) impedance, b) resistance and c) capacitance of the HePG2 cells monolayer. After a recovery period of 12 days, cells were re-exposed for others 48 h to the treatments. At the end of the second treatment, medium was given to the cells and maintained for an additional 48 h. Triton X-100 (0.1%) was then added as positive control.

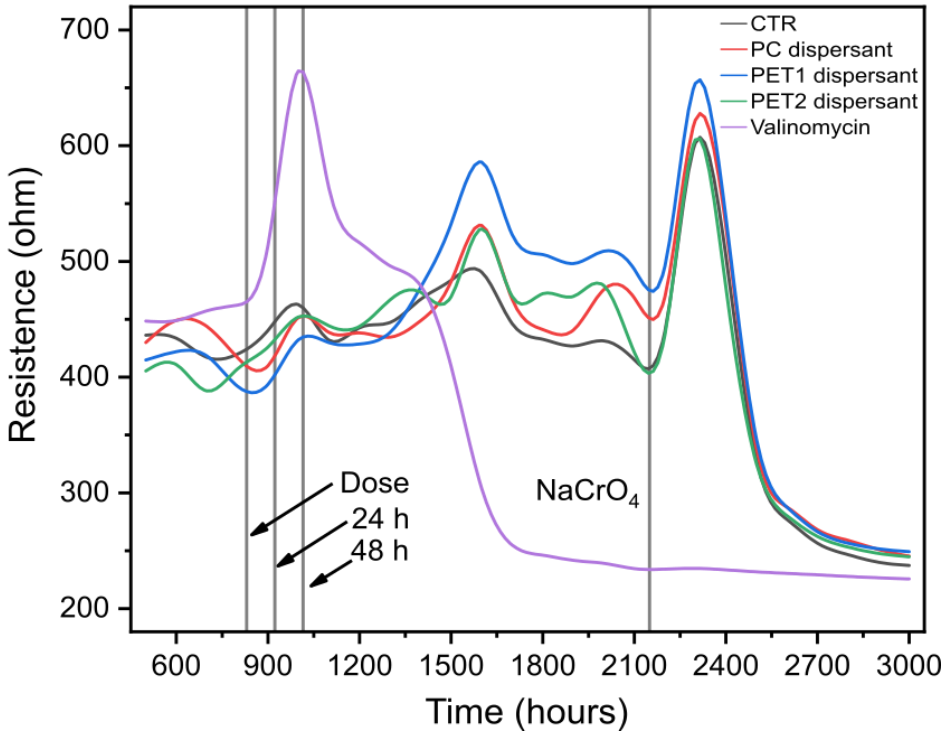

Figure 56. Electrical resistance. Differentiated Caco-2 were exposed to PC, PET1 or PET2 dispersants for 48 h. At the end of each treatment, the medium was given to the cells and then the recovery period is also analyzed. Valinomycin was used as a positive control. $NaCrO_4$ was then added as a second positive control to conclude the experiment.

Immunocytochemistry

Immunocytochemistry analysis of HePG2 (**Figure 57**) and Caco-2 (**Figure 58**) cells, exposed to the three NPs for 48h, was used to investigate possible alteration of the cytoskeleton (green staining) and of the nuclei intensity and shape (blue staining). The cytoskeleton plays an important role in multiple cellular events including determination of cell shape, adhesion, motility, intracellular transport and cellular division [195,196]. In our microscopy investigation, actin filaments were labelled by fluorescent phalloidin. Representative images reveal that, for all treatments and for both cell lines, the F-actin fibres do not lose their normal structure of well-organized stretch fibres even at 48 h of exposure to all types of NPs. Also the nuclei of all treated cells, stained with Hoechst 33258, do not show significant alterations in terms of shape, size or intensity, if compared with the untreated controls.

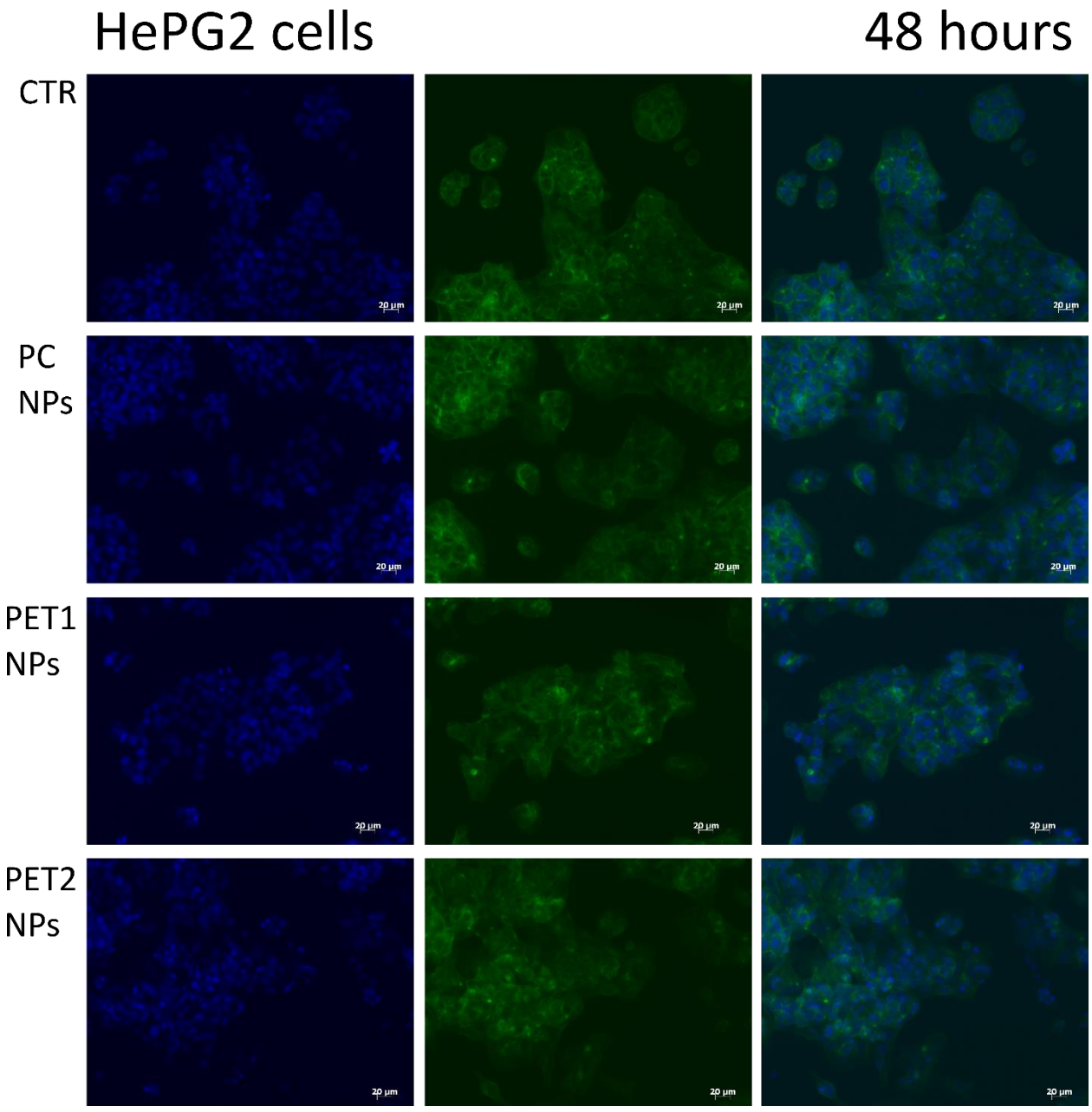

Figure 57. Representative images of HePG2 cells incubated with 10 µg/mL of the three different NPs for 48 h and stained with phalloidin (Alexa 488, F-actin green staining) and Hoechst 33258 (DAPI, nuclei blue staining). Scale bar is represented 20 µm.

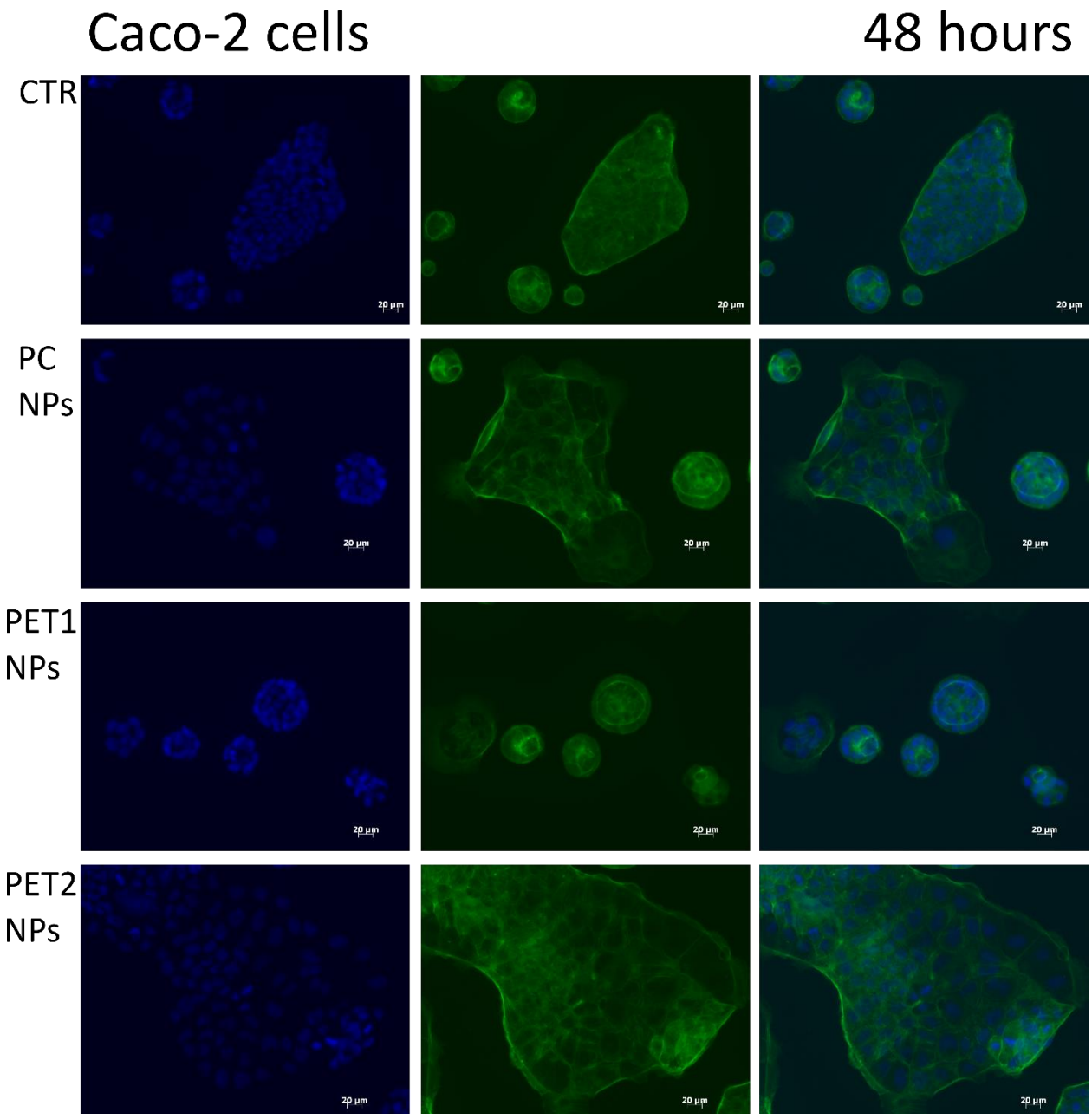

Figure 58. Representative images of Caco-2 cells incubated with 10 µg/mL of the three different NPs for 48 h and stained with phalloidin (Alexa 488, F-actin green staining) and Hoechst 33258 (DAPI, nuclei blue staining). Scale bar is represented 20 µm.

Conclusions

NPs of different chemical nature (PC or PET) and synthetized by different methods (laser ablation and chemical synthesis) are assessed for their toxicological behaviour following conventional and advanced methodologies. The two synthesis methods resulted in the formation of NPs with different polydispersity and surface morphology and chemistry. Laser ablation approach allows to obtain nano-fragments with broad size distribution and a chemical composition and polydispersity more similar to what has been observed in UV-exposed plastic materials in the environment, as the degree of oxidation of their surface is high. On the other hand, the composition of the chemically synthesized NPs resemble to the pure polymer. The toxicological assessment was performed by HCS using as *in vitro* models, HePG2 and Caco-2 cells. Results obtained indicated that the toxicity effects observed are mainly visible at very high (unrealistic) concentrations of NPs or are linked to the dispersant of the laser ablated NPs, which contains molecular products of the photo-degradation and possibly smaller NPs fragments, and is mostly observed to the PC NPs dispersions. PET1 NPs show an intermediate impact on the cells. When NPs were assessed on differentiated Caco-2 cells, a more relevant model, all NPs investigated did not show any effects in terms of toxicity. The same was observed by TEER experiments, where the absence of any damage to the Caco-2 cell monolayer confirms barrier integrity and that differentiated (polarized) cells are more resistant to NPs exposure and stress, compared to undifferentiated cells. The application of different orthogonal methods, including high throughput approaches, the use of different NPs types and production methods, and the use of different cell models are the basis for an adequate assessment of the biological response to NPs present in the environment.

Final conclusions

Managing the problem of global water pollution requires the implementation of new policies, technologies, and scientific advances. Persistent contaminants such as plastic nanofragments, capable of infiltrating the food chain and accumulating, are the greatest risk to the health of the ecosystem and of humans, principally because scientific data proving or disproving acute or long-term toxicity of NPs and MPs are scarce. Owing to the fact that it is extremely difficult to isolate and (chemically) identify micro- and, more particular, nanoparticles from environmental and biological samples, precise numbers about the human exposure towards these pollutants via the supposedly main uptake routes of ingestion and inhalation have not been determined yet. Therefore, effects on human health remain elusive and this research field needs new NPs models more representative of these pollutants in order to evaluate the impact of widespread and persistent NPs to the environments and to provide an effective risk assessment. The application of different orthogonal methods, including the use of different NPs types, different production methods, different cell models, and high throughput approaches, is the basis for an adequate assessment of the biological response to NPs present in the environment and, in this sense, this thesis contributes to developing validated methods and reference materials to contribute to advance in the risk assessment of NPs.

- Pulsed Laser ablation in water is a versatile top-down approach to synthesize NPs without the use of other reagents. Chemical analysis demonstrated the validity of PC NP model, since, in accordance with what has been observed in UV-exposed plastic materials in the environment, organic acid groups are exposed on the surface of laser-ablated NPs. The by-products obtained are the result of the photo degradation of PC. Therefore, following this approach it is offered the possibility to obtain a fully integrated product composed by components that are expected to be released in the environment during the photo-degradation of the PC plastic litter: NPs and by-products attributed to the photo-degradation.

- Biological effect of the NPs assessed *in vitro* on more complex cellular models is evaluated by different technologies. To evaluate the potential effects to the human liver, studies on PC NPs exposure to the second-generation upcyte® hepatocytes were performed. Results do not show toxicity in terms of cell viability and membrane permeability but the altered levels of albumin and CYP3A4 gene expression reveal potential toxicity towards the hepatic functionality, without provoking direct damage to the hepatocyte population. To simulate the digestive system, studies on differentiated Caco-2 cells reveals no toxicity in term of cell viability and membrane permeability and barrier integrity. Studies on the monolayer of HePG2 cells confirm these results.

- The typology of the NPs models has been proved to be fundamental for the study of the cytotoxicity of the NPs. In fact, the fabrication method adopted and the type of polymer of the NPs has a significant impact on the evaluation of the toxicity of the models.

Thereby, procedures and reference materials must be highly standardized, well defined and characterized, to allow well-grounded conclusions and safe risk assessment evaluations based on scientifically sound data.

Future perspectives

The next steps are focused on the study of the laser ablation approach on other typologies of materials, for example other type of polymers, or also biodegradable plastics and bioplastics. This typology of study allows to confirm the versatility and feasibility of this method on the NPs synthesis. Moreover, the effects of the dosimetry on the toxicological assessment may be an interesting aspect to improve considering that the laser-ablated NPs are smaller than the commercial NPs model. Previous studies have demonstrated the internalization of the NPs in the cells [18], but the amount of the NPs that reach the cells is not generally studied. Finally, an analysis of the stability and toxicological assessment of a mix of the different typologies of NPs synthesized by laser ablation may be interesting and also in combination with other pollutants.

List of publications

- ✓ Magrì, D., Veronesi M., Sànchez-Moreno P., **Tolardo V.,** Bandiera T., Pompa P., Athanassiou A., Fragouli D. PET nanoplastics interactions with water contaminants and their impact on human cells. Environ. Pollut. 271, 116262 (2020).

- ✓ **Tolardo, V.,** Magrì, D., Fumagalli, F., Cassano, D., Athanassiou, A., Fragouli, D., Gioria, S. In Vitro High-Throughput Toxicological Assessment of Nanoplastics. Nanomaterials, 12, 1947 (2022).

- ✓ **Tolardo, V.**, Romaldini, A., Fumagalli, F., Armirotti, A., Magrì, D., Athanassiou, A., Sabella S., Fragouli D. Polycarbonate nanoplastics and *in vitro* assessment of their toxicological impact on liver functionality. (To be submitted) (2022).

Other activities

- ✓ School "5th NIC at IIT practical workshop", IIT (Genova, IT), December 3rd-6th, 2018.
- ✓ Winter School "Nanoparticles from fundamentals to applications in Life Sciences" (Kandersteg, CH), February 2nd-7th, 2020.
- ✓ Visiting scientist from April 2021 to June 2021 in the Nanobiotechnology laboratory, F2 Unit, JRC (Ispra (VA), IT) to investigate on the toxicological assessment of NPs by High Content Screening (HCS).
- ✓ Oral presentation "Macrogiovani 2021", Associazione Italiana di Scienza e Tecnologia delle macromolecole (Genova, IT), July 22nd-23rd 2021.

References

1. Plastic Europe - Association of Plastics Manufactures. Plastics - the Facts 2021. *Plast. Eur.* (2021).

2. Blettler, M. C. M., Abrial, E., Khan, F. R., Sivri, N. & Espinola, L. A. Freshwater plastic pollution: Recognizing research biases and identifying knowledge gaps. *Water Research* **143**, 416–424 (2018).

3. Cózar, A. *et al.* Plastic debris in the open ocean. *Proc. Natl. Acad. Sci. U. S. A.* **111**, 10239–10244 (2014).

4. Huerta Lwanga, E. *et al.* Field evidence for transfer of plastic debris along a terrestrial food chain. *Sci. Rep.* **7**, 1–7 (2017).

5. Wayman, C. & Niemann, H. The fate of plastic in the ocean environment-a minireview. *Environmental Science: Processes and Impacts* **23**, 198–212 (2021).

6. Redondo-Hasselerharm, P. E., Gort, G., Peeters, E. T. H. M. & Koelmans, A. A. Nano- And microplastics affect the composition of freshwater benthic communities in the long term. *Sci. Adv.* **6**, (2020).

7. Shruti, V. C., Pérez-Guevara, F., Elizalde-Martínez, I. & Kutralam-Muniasamy, G. First study of its kind on the microplastic contamination of soft drinks, cold tea and energy drinks - Future research and environmental considerations. *Sci. Total Environ.* **726**, 138580 (2020).

8. Shi, Y. *et al.* Insight into chain scission and release profiles from photodegradation of polycarbonate microplastics. *Water Res.* **195**, 116980 (2021).

9. Dick Vethaak, A. & Legler, J. Microplastics and human health: Knowledge gaps should be addressed to ascertain the health risks of microplastics. *Science* **371**, 672–674 (2021).

10. Brachner, A. *et al.* Assessment of human health risks posed by nano-and microplastics is currently not feasible. *Int. J. Environ. Res. Public Health* **17**, 1–10 (2020).

11. Rahman, A., Sarkar, A., Yadav, O. P., Achari, G. & Slobodnik, J. Potential human health risks due to environmental exposure to nano- and microplastics and knowledge gaps: A scoping review. *Science of the Total Environment* **757**, 143872 (2021).

12. Cho, Y. M. & Choi, K. H. The current status of studies of human exposure assessment of microplastics and their health effects: A rapid systematic review. *Environ. Health Toxicol.* **36**, 1–8 (2021).

13. Rubio, L., Marcos, R. & Hernández, A. Potential adverse health effects of ingested micro- and nanoplastics on humans. Lessons learned from in vivo and in vitro mammalian models. *J. Toxicol. Environ. Heal. - Part B Crit. Rev.* **23**, 51–68 (2020).

14. Sarau, G. *et al.* Correlative Microscopy and Spectroscopy Workflow for Microplastics. *Appl. Spectrosc.* **74**, 1155–1160 (2020).

15. Oßmann, B. E. *et al.* Development of an optimal filter substrate for the identification of small microplastic particles in food by micro-Raman spectroscopy. *Anal. Bioanal. Chem.* **409**, 4099–4109 (2017).

16. Sobhani, Z. *et al.* Identification and visualisation of microplastics/nanoplastics by Raman imaging (i): Down to 100 nm. *Water Res.* **174**, 115658 (2020).

17. Wang, J. *et al.* Characterization, occurrence, environmental behaviors, and risks of nanoplastics in the aquatic environment: Current status and future perspectives. *Fundamental Research* **1**, 317–328 (2021).

18. Magrì, D. *et al.* Laser ablation as a versatile tool to mimic polyethylene terephthalate nanoplastic pollutants: Characterization and toxicology assessment. *ACS Nano* **12**, 7690–7700 (2018).

19. Magrì, D. *et al.* PET nanoplastics interactions with water contaminants and their impact on human cells. *Environ. Pollut.* **271**, 116262 (2020).

20. Sheldon, R. A. & Norton, M. Green chemistry and the plastic pollution challenge: Towards a circular economy. *Green Chemistry* **22**, 6310–6322 (2020).

21. Amaral-Zettler, L. A., Zettler, E. R. & Mincer, T. J. Ecology of the plastisphere. *Nature Reviews Microbiology* **18**, 139–151 (2020).

22. Zalasiewicz, J. *et al.* The geological cycle of plastics and their use as a stratigraphic indicator of the Anthropocene. *Anthropocene* **13**, 4–17 (2016).

23. Borrelle, S. B. *et al.* Predicted growth in plastic waste exceeds efforts to mitigate plastic pollution. *Science (80-.).* **369**, 1515–1518 (2020).

24. Oliveri Conti, G. *et al.* Micro- and nano-plastics in edible fruit and vegetables. The first diet risks assessment for the general population. *Environ. Res.* **187**, 109677 (2020).

25. Geyer, R., Jambeck, J. R. & Law, K. L. Production, use, and fate of all plastics ever made. *Sci. Adv.* **3**, (2017).

26. Lau, W. W. Y. *et al.* Evaluating scenarios toward zero plastic pollution. *Science (80-.).* **369**, (2020).

27. Peng, L. *et al.* Micro- and nano-plastics in marine environment: Source, distribution and threats — A review. *Science of the Total Environment* **698**, 134254 (2020).

28. Jambeck, J. R. *et al.* Plastic waste inputs from land into the ocean. *Science (80-.).* **347**, 768–771 (2015).

29. Kooi, M. & Koelmans, A. A. Simplifying Microplastic via Continuous Probability Distributions for Size, Shape,and Density. *Environ. Sci. Technol. Lett.* **6**, 551–557 (2019).

30. Ter Halle, A. *et al.* Understanding the Fragmentation Pattern of Marine Plastic Debris. *Environ. Sci. Technol.* **50**, 5668–5675 (2016).

31. Van Sebille, E. *et al.* The physical oceanography of the transport of floating marine debris. *Environmental Research Letters* **15**, 023003 (2020).

32. Wang, L. *et al.* Environmental fate, toxicity and risk management strategies of nanoplastics in the environment: Current status and future perspectives. *J. Hazard. Mater.* **401**, 123415 (2021).

33. Everaert, G. *et al.* Risks of floating microplastic in the global ocean. *Environ. Pollut.* **267**, 115499 (2020).

34. Besseling, E., Redondo-Hasselerharm, P., Foekema, E. M. & Koelmans, A. A. Quantifying ecological risks of aquatic micro- and nanoplastic. *Crit. Rev. Environ. Sci. Technol.* **49**, 32–80 (2019).

35. Chamas, A. *et al.* Degradation Rates of Plastics in the Environment. *ACS Sustain. Chem. Eng.* **8**, 3494–3511 (2020).

36. Pathak, V. M. & Navneet. Review on the current status of polymer degradation: a microbial approach. *Bioresources and Bioprocessing* **4**, 1–31 (2017).

37. Thompson, R. C., Swan, S. H., Moore, C. J. & Vom Saal, F. S. Our plastic age. *Philosophical Transactions of the Royal Society B: Biological Sciences* **364**, 1973–1976 (2009).

38. Greven, A. C. *et al.* Polycarbonate and polystyrene nanoplastic particles act as stressors to the innate immune system of fathead minnow (Pimephales promelas). *Environ. Toxicol. Chem.* **35**, 3093–3100 (2016).

39. Arp, H. P. H. *et al.* Weathering Plastics as a Planetary Boundary Threat: Exposure, Fate, and Hazards. *Environmental Science and Technology* **55**, 7246–7255 (2021).

40. Cai, L., Wang, J., Peng, J., Wu, Z. & Tan, X. Observation of the degradation of three types of plastic pellets exposed to UV irradiation in three different environments. *Sci. Total Environ.* **628**–**629**, 740–747 (2018).

41. Gewert, B., Plassmann, M. M. & MacLeod, M. Pathways for degradation of plastic polymers floating in the marine environment. *Environ. Sci. Process. Impacts* **17**, 1513–1521 (2015).

42. Kalogerakis, N. *et al.* Microplastics generation: Onset of fragmentation of polyethylene films in marine environment mesocosms. *Front. Mar. Sci.* **4**, 84 (2017).

43. Garnai Hirsch, S., Barel, B. & Segal, E. Characterization of surface phenomena: probing early stage degradation of low-density polyethylene films. *Polym. Eng. Sci.* **59**, E129–E137 (2019).

44. Enfrin, M. *et al.* Release of hazardous nanoplastic contaminants due to microplastics fragmentation under shear stress forces. *J. Hazard. Mater.* **384**, (2020).

45. Ekvall, M. T. *et al.* Nanoplastics formed during the mechanical breakdown of daily-use polystyrene products. *Nanoscale Adv.* **1**, 1055–1061 (2019).

46. Garvey, C. J. *et al.* Molecular-Scale Understanding of the Embrittlement in Polyethylene

Ocean Debris. *Environ. Sci. Technol.* **54**, 11173–11181 (2020).

47. Ter Halle, A. *et al.* To what extent are microplastics from the open ocean weathered? *Environ. Pollut.* **227**, 167–174 (2017).

48. Galloway, T. S., Cole, M. & Lewis, C. Interactions of microplastic debris throughout the marine ecosystem. *Nature Ecology and Evolution* **1**, 1–8 (2017).

49. Harrison, J. P., Schratzberger, M., Sapp, M. & Osborn, A. M. Rapid bacterial colonization of low-density polyethylene microplastics in coastal sediment microcosms. *BMC Microbiol.* **14**, 1–15 (2014).

50. Zettler, E. R., Mincer, T. J. & Amaral-Zettler, L. A. Life in the 'plastisphere': Microbial communities on plastic marine debris. *Environ. Sci. Technol.* **47**, 7137–7146 (2013).

51. McGivney, E. *et al.* Rapid Physicochemical Changes in Microplastic Induced by Biofilm Formation. *Front. Bioeng. Biotechnol.* **8**, 205 (2020).

52. Oberbeckmann, S., Loeder, M. G. J., Gerdts, G. & Osborn, M. A. Spatial and seasonal variation in diversity and structure of microbial biofilms on marine plastics in Northern European waters. *FEMS Microbiol. Ecol.* **90**, 478–492 (2014).

53. MacLeod, M., Arp, H. P. H., Tekman, M. B. & Jahnke, A. The global threat from plastic pollution. *Science (80-.).* **373**, 61–65 (2021).

54. Hartmann, N. B. *et al.* Are We Speaking the Same Language? Recommendations for a Definition and Categorization Framework for Plastic Debris. *Environ. Sci. Technol.* **53**, 1039–1047 (2019).

55. Allan, J. *et al.* Regulatory landscape of nanotechnology and nanoplastics from a global perspective. *Regul. Toxicol. Pharmacol.* **122**, 104885 (2021).

56. da Costa, J. P., Santos, P. S. M., Duarte, A. C. & Rocha-Santos, T. (Nano)plastics in the environment - Sources, fates and effects. *Sci. Total Environ.* **566**–**567**, 15–26 (2016).

57. International Organization for Standardization (ISO). Plastics — Environmental aspects — State of knowledge and methodologies. ISO/TR 21960:2020 (2020). Available at: https://www.iso.org/standard/72300.html. (Accessed: 16th March 2022)

58. Gigault, J. *et al.* Current opinion: What is a nanoplastic? *Environ. Pollut.* **235**, 1030–1034 (2018).

59. Fendall, L. S. & Sewell, M. A. Contributing to marine pollution by washing your face: Microplastics in facial cleansers. *Mar. Pollut. Bull.* **58**, 1225–1228 (2009).

60. Wardrop, P. *et al.* Chemical Pollutants Sorbed to Ingested Microbeads from Personal Care Products Accumulate in Fish. *Environ. Sci. Technol.* **50**, 4037–4044 (2016).

61. Gigault, J., Pedrono, B., Maxit, B. & Ter Halle, A. Marine plastic litter: The unanalyzed nano-fraction. *Environ. Sci. Nano* **3**, 346–350 (2016).

62. Lambert, S. & Wagner, M. Characterisation of nanoplastics during the degradation of polystyrene. *Chemosphere* **145**, 265–268 (2016).

63. EFSA Panel on Contaminants in the Food Chain (CONTAM). Presence of microplastics and nanoplastics in food, with particular focus on seafood. *EFSA J.* **14**, (2016).

64. Alimi, O. S., Farner Budarz, J., Hernandez, L. M. & Tufenkji, N. Microplastics and Nanoplastics in Aquatic Environments: Aggregation, Deposition, and Enhanced Contaminant Transport. *Environmental Science and Technology* **52**, 1704–1724 (2018).

65. Clark, J. R. *et al.* Marine microplastic debris: a targeted plan for understanding and quantifying interactions with marine life. *Frontiers in Ecology and the Environment* **14**, 317–324 (2016).

66. Suhrhoff, T. J. & Scholz-Böttcher, B. M. Qualitative impact of salinity, UV radiation and turbulence on leaching of organic plastic additives from four common plastics - A lab experiment. *Mar. Pollut. Bull.* **102**, 84–94 (2016).

67. Wright, S. L., Thompson, R. C. & Galloway, T. S. The physical impacts of microplastics on marine organisms: a review. *Environmental pollution (Barking, Essex : 1987)* **178**, 483–492 (2013).

68. Carbery, M., Connor, W. O. & Thavamani, P. Trophic transfer of microplastics and mixed contaminants in the marine food web and implications for human health. *Environ. Int.* **115**, 400–409 (2018).

69. Rowenczyk, L. *et al.* Microstructure Characterization of Oceanic Polyethylene Debris. *Environ. Sci. Technol.* **54**, 4102–4109 (2020).

70. Li, Z. *et al.* Combined effect of polystyrene microplastics and dibutyl phthalate on the microalgae Chlorella pyrenoidosa. *Environ. Pollut.* **257**, 113604 (2020).

71. Ng, E. L. *et al.* An overview of microplastic and nanoplastic pollution in agroecosystems. *Science of the Total Environment* **627**, 1377–1388 (2018).

72. Cedervall, T., Hansson, L. A., Lard, M., Frohm, B. & Linse, S. Food chain transport of nanoparticles affects behaviour and fat metabolism in fish. *PLoS One* **7**, e32254 (2012).

73. Cole, M. *et al.* Microplastic ingestion by zooplankton. *Environ. Sci. Technol.* **47**, 6646–6655 (2013).

74. Browne, M. A., Dissanayake, A., Galloway, T. S., Lowe, D. M. & Thompson, R. C. Ingested microscopic plastic translocates to the circulatory system of the mussel, Mytilus edulis (L.). *Environ. Sci. Technol.* **42**, 5026–5031 (2008).

75. Graham, E. R. & Thompson, J. T. Deposit- and suspension-feeding sea cucumbers (Echinodermata) ingest plastic fragments. *J. Exp. Mar. Bio. Ecol.* **368**, 22–29 (2009).

76. Setälä, O., Norkko, J. & Lehtiniemi, M. Feeding type affects microplastic ingestion in a coastal invertebrate community. *Mar. Pollut. Bull.* **102**, 95–101 (2016).

77. Eriksson, C. & Burton, H. Origins and Biological Accumulation of Small Plastic Particles in Fur Seals from Macquarie Island. *Ambio* **32**, 380–384 (2003).

78. Bouwmeester, H., Hollman, P. C. H. & Peters, R. J. B. Potential Health Impact of Environmentally Released Micro- and Nanoplastics in the Human Food Production Chain: Experiences from Nanotoxicology. *Environmental Science and Technology* **49**, 8932–8947 (2015).

79. Bhattacharjee, S. *et al.* Role of membrane disturbance and oxidative stress in the mode of action underlying the toxicity of differently charged polystyrene nanoparticles. *RSC Adv.* **4**, 19321–19330 (2014).

80. Bhargava, S. *et al.* Fate of Nanoplastics in Marine Larvae: A Case Study Using Barnacles, Amphibalanus amphitrite. *ACS Sustain. Chem. Eng.* **6**, 6932–6940 (2018).

81. Ferreira, G. V. B. *et al.* High intake rates of microplastics in a Western Atlantic predatory fish, and insights of a direct fishery effect. *Environ. Pollut.* **236**, 706–717 (2018).

82. Fonte, E., Ferreira, P. & Guilhermino, L. Temperature rise and microplastics interact with the toxicity of the antibiotic cefalexin to juveniles of the common goby (Pomatoschistus microps): Post-exposure predatory behaviour, acetylcholinesterase activity and lipid peroxidation. *Aquat. Toxicol.* **180**, 173–185 (2016).

83. Li, J., Green, C., Reynolds, A., Shi, H. & Rotchell, J. M. Microplastics in mussels sampled from coastal waters and supermarkets in the United Kingdom. *Environ. Pollut.* **241**, 35–44 (2018).

84. Liebezeit, G. & Liebezeit, E. Non-pollen particulates in honey and sugar. *Food Addit. Contam. - Part A Chem. Anal. Control. Expo. Risk Assess.* **30**, 2136–2140 (2013).

85. Liebezeit, G. & Liebezeit, E. Synthetic particles as contaminants in German beers. *Food Addit. Contam. - Part A Chem. Anal. Control. Expo. Risk Assess.* **31**, 1574–1578 (2014).

86. He, D., Zhang, Y. & Gao, W. Micro(nano)plastic contaminations from soils to plants: human food risks. *Current Opinion in Food Science* **41**, 116–121 (2021).

87. Schwabl, P. *et al.* Detection of various microplastics in human stool: A prospective case series. *Ann. Intern. Med.* **171**, 453–457 (2019).

88. Revel, M., Châtel, A. & Mouneyrac, C. Micro(nano)plastics: A threat to human health? *Curr. Opin. Environ. Sci. Heal.* **1**, 17–23 (2018).

89. Barbosa, F., Adeyemi, J. A., Bocato, M. Z., Comas, A. & Campiglia, A. A critical viewpoint on current issues, limitations, and future research needs on micro- and nanoplastic studies: From the detection to the toxicological assessment. *Environmental Research* **182**, 109089 (2020).

90. Jacob, H., Besson, M., Swarzenski, P. W., Lecchini, D. & Metian, M. Effects of Virgin Micro- and Nanoplastics on Fish: Trends, Meta-Analysis, and Perspectives. *Environ. Sci. Technol.* **54**, 4733–4745 (2020).

91. Balakrishnan, G., Déniel, M., Nicolai, T., Chassenieux, C. & Lagarde, F. Towards more realistic reference microplastics and nanoplastics: preparation of polyethylene micro/nanoparticles with a biosurfactant. *Environ. Sci. Nano* **6**, 315–324 (2019).

92. Rodríguez-Hernández, A. G., Muñoz-Tabares, J. A., Aguilar-Guzmán, J. C. & Vazquez-Duhalt, R. A novel and simple method for polyethylene terephthalate (PET) nanoparticle production. *Environ. Sci. Nano* **6**, 2031–2036 (2019).

93. Pessoni, L. *et al.* Soap- and metal-free polystyrene latex particles as a nanoplastic model. *Environ. Sci. Nano* **6**, 2253–2258 (2019).

94. Cassano, D., La Spina, R., Ponti, J., Bianchi, I. & Gilliland, D. Inorganic Species-Doped Polypropylene Nanoparticles for Multifunctional Detection. *ACS Appl. Nano Mater.* **4**, 1551–1557 (2021).

95. Mitrano, D. M. *et al.* Synthesis of metal-doped nanoplastics and their utility to investigate fate and behaviour in complex environmental systems. *Nat. Nanotechnol.* **14**, 362–368 (2019).

96. Johnson, L. M. *et al.* Fabrication of polyethylene terephthalate (PET) nanoparticles with fluorescent tracers for studies in mammalian cells. *Nanoscale Adv.* **3**, 339–346 (2021).

97. Astner, A. F. *et al.* Mechanical formation of micro- and nano-plastic materials for environmental studies in agricultural ecosystems. *Sci. Total Environ.* **685**, 1097–1106 (2019).

98. El Hadri, H., Gigault, J., Maxit, B., Grassl, B. & Reynaud, S. Nanoplastic from mechanically degraded primary and secondary microplastics for environmental assessments. *NanoImpact* **17**, 1–20 (2020).

99. Garwin, L. & Lincoln, T. *A Century of Nature: Twenty-One Discoveries that Changed Science and the World*. *A Century of Nature* **2003**, (University of Chicago Press, 2013).

100. Ravi-Kumar, S., Lies, B., Zhang, X., Lyu, H. & Qin, H. Laser ablation of polymers: a review. *Polymer International* **68**, 1391–1401 (2019).

101. Yang, G. W. & Wang, J. B. Carbon nitride nanocrystals having cubic structure using pulsed laser induced liquid-solid interfacial reaction. *Appl. Phys. A Mater. Sci. Process.* **71**, 343–344 (2000).

102. Yang, G. W. Laser ablation in liquids: Applications in the synthesis of nanocrystals. *Progress in Materials Science* **52**, 648–698 (2007).

103. Kanitz, A. *et al.* Review on experimental and theoretical investigations of the early stage, femtoseconds to microseconds processes during laser ablation in liquid-phase for the synthesis of colloidal nanoparticles. *Plasma Sources Science and Technology* **28**, 103001 (2019).

104. Deutsch, T. F. & Geis, M. W. Self-developing UV photoresist using excimer laser exposure. *J. Appl. Phys.* **54**, 7201–7204 (1983).

105. Mahan, G. D., Cole, H. S., Liu, Y. S. & Philipp, H. R. Theory of polymer ablation. *Appl. Phys. Lett.* **53**, 2377–2379 (1988).

106. Cain, S. R. A photothermal model for polymer ablation: Chemical modification. *J. Phys. Chem.* **97**, 7572–7577 (1993).

107. Urech, L. & Lippert, T. *Photoablation of polymers*. *Photochemistry and Photophysics ofPolymer Materials* (2010). doi:10.1016/0169-4332(92)90051-X

108. Martínez-Tong, D. E. *et al.* Formation of polymer nanoparticles by UV pulsed laser ablation of poly (bisphenol A carbonate) in liquid environment. *Appl. Surf. Sci.* **418**, 522–529 (2017).

109. Elaboudi, I., Lazare, S., Belin, C., Talaga, D. & Labrugère, C. From polymer films to organic nanoparticles suspensions by means of excimer laser ablation in water. *Appl. Phys. A Mater. Sci. Process.* **93**, 827–831 (2008).

110. Chang, T. C. & Molian, P. A. Excimer pulsed laser ablation of polymers in air and liquids for micromachining applications. *J. Manuf. Process.* **1**, 1–17 (1999).

111. Zhang, J., Wang, L., Halden, R. U. & Kannan, K. Polyethylene Terephthalate and Polycarbonate Microplastics in Sewage Sludge Collected from the United States. *Environ. Sci. Technol. Lett.* **6**, 650–655 (2019).

112. Zhang, J., Wang, L. & Kannan, K. Polyethylene Terephthalate and Polycarbonate Microplastics in Pet Food and Feces from the United States. *Environ. Sci. Technol.* **53**, 12035–12042 (2019).

113. Zhang, J., Wang, L., Trasande, L. & Kannan, K. Occurrence of Polyethylene Terephthalate and Polycarbonate Microplastics in Infant and Adult Feces. *Environ. Sci. Technol. Lett.* **8**, 989–994 (2021).

114. Migahed, M. D. & Zidan, H. M. Influence of UV-irradiation on the structure and optical properties of polycarbonate films. *Curr. Appl. Phys.* **6**, 91–96 (2006).

115. Webb, H. K., Arnott, J., Crawford, R. J. & Ivanova, E. P. Plastic degradation and its environmental implications with special reference to poly(ethylene terephthalate). *Polymers (Basel).* **5**, 1–18 (2013).

116. Ling, X. Y., Phang, I. Y., Vancso, G. J., Huskens, J. & Reinhoudt, D. N. Stable and transparent superhydrophobic nanoparticle films. *Langmuir* **25**, 3260–3263 (2009).

117. Kramer, T., Remund, S., Jäggi, B., Schmid, M. & Neuenschwander, B. Ablation dynamics – from absorption to heat accumulation / ultra-fast laser matter interaction. *Adv. Opt. Technol.* **7**, 129–144 (2018).

118. Baudach, S., Bonse, J., Krüger, J. & Kautek, W. Ultrashort pulse laser ablation of polycarbonate and polymethylmethacrylate. *Appl. Surf. Sci.* **154**, 555–560 (2000).

119. Jellinek, H. H. G. & Srinivasan, R. Theory of etching of polymers by far-ultraviolet, high-intensity pulsed laser and long-term irradiation. *J. Phys. Chem.* **88**, 3048–3051 (1984).

120. Calcagno, L., Compagnini, G. & Foti, G. Structural modification of polymer films by ion irradiation. *Nucl. Inst. Methods Phys. Res. B* **65**, 413–422 (1992).

121. Betz, N. *et al.* A FTIR study of PVDF irradiated by means of swift heavy ions. *J. Polym. Sci. Part B Polym. Phys.* **32**, 1493–1502 (1994).

122. Kumar, R. *et al.* Physico-chemical modifications induced in Makrofol-N polycarbonate by swift heavy ions. *Nucl. Instruments Methods Phys. Res. Sect. B Beam Interact. with Mater. Atoms* **251**, 163–166 (2006).

123. Bahniwal, S. *et al.* Changes in structural and optical properties of polycarbonate induced by Ag+ Ion implantation. *J. Macromol. Sci. Part B Phys.* **49**, 259–268 (2010).

124. Chen, C. *et al.* Organotin Release from Polyvinyl Chloride Microplastics and Concurrent Photodegradation in Water: Impacts from Salinity, Dissolved Organic Matter, and Light Exposure. *Environ. Sci. Technol.* **53**, 10741–10752 (2019).

125. Lemaire, J., Gardette, J. L., Rivaton, A. & Roger, A. Dual photo-chemistries in aliphatic polyamides, bisphenol A polycarbonate and aromatic polyurethanes-A short review. *Polym. Degrad. Stab.* **15**, 1–13 (1986).

126. Diepens, M. & Gijsman, P. Photodegradation of bisphenol A polycarbonate. *Polym. Degrad. Stab.* **92**, 397–406 (2007).

127. Rivaton, A. Recent advances in bisphenol-A polycarbonate photodegradation. *Polym. Degrad. Stab.* **49**, 163–179 (1995).

128. Andrady, A. L., Searle, N. D. & Crewdson, L. F. E. Wavelength sensitivity of unstabilized and UV stabilized polycarbonate to solar simulated radiation. *Polym. Degrad. Stab.* **35**, 235–247 (1992).

129. Clark, D. T. & Munro, H. S. Surface and bulk aspects of the natural and artificial photo-ageing of Bisphenol A polycarbonate as revealed by ESCA and difference UV spectroscopy. *Polym. Degrad. Stab.* **8**, 195–211 (1984).

130. Clark, D. T. & Munro, H. S. Surface aspects of the photodegradation of bisphenol a polycarbonate in oxygen and nitrogen atmospheres as revealed by ESCA. *Polym. Degrad. Stab.* **4**, 441–457 (1982).

131. Factor, A., Ligon, W. V. & May, R. J. The Role of Oxygen in the Photoaging of Bisphenol A Polycarbonate. *Macromolecules* **20**, 2461–2468 (1987).

132. Rivaton, A., Sallet, D. & Lemaire, J. The photo-chemistry of bisphenol-A polycarbonate reconsidered: Part 3-Influence of water on polycarbonate photo-chemistry. *Polym. Degrad. Stab.* **14**, 23–40 (1986).

133. Mattsson, K. *et al.* Brain damage and behavioural disorders in fish induced by plastic nanoparticles delivered through the food chain. *Sci. Rep.* **7**, (2017).

134. Toussaint, B. *et al.* Review of micro- and nanoplastic contamination in the food chain. *Food*

Additives and Contaminants - Part A Chemistry, Analysis, Control, Exposure and Risk Assessment **36**, 639–673 (2019).

135. Barboza, L. G. A. *et al.* Microplastics in wild fish from North East Atlantic Ocean and its potential for causing neurotoxic effects, lipid oxidative damage, and human health risks associated with ingestion exposure. *Sci. Total Environ.* **717**, 134625 (2020).

136. Kumar, R. *et al.* Impacts of plastic pollution on ecosystem services, sustainable development goals, and need to focus on circular economy and policy interventions. *Sustain.* **13**, 1–40 (2021).

137. Ockenden, A., Tremblay, L. A., Dikareva, N. & Simon, K. S. Towards more ecologically relevant investigations of the impacts of microplastic pollution in freshwater ecosystems. *Sci. Total Environ.* **792**, 148507 (2021).

138. Jani, P., Halbert, G. W., Langridge, J. & Florence, A. T. Nanoparticle Uptake by the Rat Gastrointestinal Mucosa: Quantitation and Particle Size Dependency. *J. Pharm. Pharmacol.* **42**, 821–826 (1990).

139. Chae, Y., Kim, D., Kim, S. W. & An, Y.-J. Trophic transfer and individual impact of nano-sized polystyrene in a four-species freshwater food chain. *Sci. Rep.* **8**, 284 (2018).

140. Brandts, I. *et al.* Effects of polymethylmethacrylate nanoplastics on Dicentrarchus labrax. *Genomics* **110**, 435–441 (2018).

141. Levy, G. *et al.* Long-term culture and expansion of primary human hepatocytes. *Nat. Biotechnol.* **33**, 1264–1271 (2015).

142. Tolosa, L. *et al.* Long-term and mechanistic evaluation of drug-induced liver injury in Upcyte human hepatocytes. *Arch. Toxicol.* **93**, 519–532 (2019).

143. Burkard, A. *et al.* Generation of proliferating human hepatocytes using upcyte® technology: Characterisation and applications in induction and cytotoxicity assays. *Xenobiotica* **42**, 939–956 (2012).

144. Tolosa, L. *et al.* Human upcyte hepatocytes: Characterization of the hepatic phenotype and evaluation for acute and long-term hepatotoxicity routine testing. *Toxicol. Sci.* **152**, 214–229 (2016).

145. Anzenbacher, P. & Anzenbacherová, E. Cytochromes P450 and metabolism of xenobiotics. *Cellular and Molecular Life Sciences* **58**, 737–747 (2001).

146. Chomczynski, P. A reagent for the single-step simultaneous isolation of RNA, DNA and proteins from cell and tissue samples. *Biotechniques* **15**, 532–537 (1993).

147. Pfaffl, M. W. A new mathematical model for relative quantification in real-time RT–PCR. *Nucleic Acids Res.* **29**, E45 (2001).

148. Goyal, P. K. *et al.* Modification of polycarbonate surface by Ar + ion implantation for various opto-electronic applications. *Vacuum* **86**, 1087–1091 (2012).

149. Resta, V., Quarta, G., Lomascolo, M., Maruccio, L. & Calcagnile, L. Raman and Photoluminescence spectroscopy of polycarbonate matrices irradiated with different energy 28Si+ ions. *Vacuum* **116**, 82–89 (2015).

150. Jia, Y., Asahara, H., Hsu, Y. I., Asoh, T. A. & Uyama, H. Surface modification of polycarbonate using the light-activated chlorine dioxide radical. *Appl. Surf. Sci.* **530**, 147202 (2020).

151. Blancho, F., Davranche, M., Fumagalli, F., Ceccone, G. & Gigault, J. A reliable procedure to obtain environmentally relevant nanoplastic proxies. *Environ. Sci. Nano* **8**, 3211–3219 (2021).

152. Monopoli, M. P. *et al.* Physical-Chemical aspects of protein corona: Relevance to in vitro and in vivo biological impacts of nanoparticles. *J. Am. Chem. Soc.* **133**, 2525–2534 (2011).

153. Rivaton, A., Sallet, D. & Lemaire, J. The photochemistry of bisphenol-A polycarbonate reconsidered. *Polym. Photochem.* **3**, 463–481 (1983).

154. Jahnke, L., White, A. & Sampath-Wiley, P. The Effects of Ultraviolet Radiation on Dunaliella. in *The Alga Dunaliella* 231–272 (2009). doi:10.1201/b10300-11

155. Clark, D. T. & Munro, H. S. Surface aspects of the photo-degradation of bisphenol A polycarbonate, in oxygen and air as a function of relative humidity, as revealed by ESCA. *Polym. Degrad. Stab.* **5**, 227–236 (1983).

156. Pankasem, S., Kuczynski, J. & Thomas, J. K. Photochemistry and Photodegradation of Polycarbonate. *Macromolecules* **27**, 3773–3781 (1994).

157. Erickson, H. P. Size and shape of protein molecules at the nanometer level determined by sedimentation, gel filtration, and electron microscopy. *Biol. Proced. Online* **11**, 32–51 (2009).

158. Gewert, B., Plassmann, M., Sandblom, O. & Macleod, M. Identification of Chain Scission Products Released to Water by Plastic Exposed to Ultraviolet Light. *Environ. Sci. Technol. Lett.* **5**, 272–276 (2018).

159. Cortés, C. *et al.* Nanoplastics as a potential environmental health factor: Effects of polystyrene nanoparticles on human intestinal epithelial Caco-2 cells. *Environ. Sci. Nano* **7**, 272–285 (2020).

160. Achour, B., Barber, J. & Rostami-Hodjegan, A. Expression of hepatic drug-metabolizing cytochrome P450 enzymes and their intercorrelations: A meta-analysis. *Drug Metab. Dispos.* **42**, 1349–1356 (2014).

161. Chojkier, M. Inhibition of albumin synthesis in chronic diseases: Molecular mechanisms. *Journal of Clinical Gastroenterology* **39**, (2005).

162. Merlot, A. M., Kalinowski, D. S. & Richardson, D. R. Unraveling the mysteries of serum albumin-more than just a serum protein. *Front. Physiol.* **5 AUG**, 299 (2014).

163. Gatta, A., Verardo, A. & Bolognesi, M. Hypoalbuminemia. *Internal and Emergency*

Medicine **7**, 193–199 (2012).

164. Chojkier, M. Inhibition of albumin synthesis in chronic diseases: Molecular mechanisms. *Journal of Clinical Gastroenterology* **39**, (2005).

165. Gioria, S. *et al.* Are existing standard methods suitable for the evaluation of nanomedicines: Some case studies. *Nanomedicine* **13**, 539–554 (2018).

166. Monteiro-Riviere, N. A., Inman, A. O. & Zhang, L. W. Limitations and relative utility of screening assays to assess engineered nanoparticle toxicity in a human cell line. *Toxicol. Appl. Pharmacol.* **234**, 222–235 (2009).

167. Han, X. *et al.* Validation of an LDH assay for assessing nanoparticle toxicity. *Toxicology* **287**, 99–104 (2011).

168. Guadagnini, R. *et al.* Toxicity screenings of nanomaterials: Challenges due to interference with assay processes and components of classic in vitro tests. *Nanotoxicology* **9**, 13–24 (2015).

169. International Organization for Standardization (ISO). Biological evaluation of medical devices - Part 22: guidance on nanomaterials (ISO/TR 10993–22). ISO/TR 10993–22:2017 (2017).

170. Bredeck, G., Halamoda-Kenzaoui, B., Bogni, A., Lipsa, D. & Bremer-Hoffmann, S. Tiered testing of micro- and nanoplastics using intestinal in vitro models to support hazard assessments. *Environ. Int.* **158**, 106921 (2022).

171. Cohen, J. M., Deloid, G. M. & Demokritou, P. A critical review of in vitro dosimetry for engineered nanomaterials. *Nanomedicine* **10**, 3015–3032 (2015).

172. Wilhelm, C., Gazeau, F., Roger, J., Pons, J. N. & Bacri, J. C. Interaction of anionic superparamagnetic nanoparticles with cells: Kinetic analyses of membrane adsorption and subsequent internalization. *Langmuir* **18**, 8148–8155 (2002).

173. Wittmaack, K. Excessive delivery of nanostructured matter to submersed cells caused by rapid gravitational settling. *ACS Nano* **5**, 3766–3778 (2011).

174. Rischitor, G. *et al.* Quantification of the cellular dose and characterization of nanoparticle transport during in vitro testing. *Part. Fibre Toxicol.* **13**, 1–16 (2016).

175. Lang, P., Yeow, K., Nichols, A. & Scheer, A. Cellular imaging in drug discovery. *Nat. Rev. Drug Discov.* **5**, 343–356 (2006).

176. Ramery, E. & O'Brien, P. J. Evaluation of the cytotoxicity of organic dust components on THP1 monocytes-derived macrophages using high content analysis. *Environ. Toxicol.* **29**, 310–319 (2014).

177. Collins, A. R. *et al.* High throughput toxicity screening and intracellular detection of nanomaterials. *Wiley Interdiscip. Rev. Nanomedicine Nanobiotechnology* **9**, (2017).

178. Lin, S. *et al.* High content screening in zebrafish speeds up hazard ranking of transition

metal oxide nanoparticles. *ACS Nano* **5**, 7284–7295 (2011).

179. Zhang, T. *et al.* Cellular effect of high doses of silica-coated quantum dot profiled with high throughput gene expression analysis and high content cellomics measurements. *Nano Lett.* **6**, 800–808 (2006).

180. Anguissola, S., Garry, D., Salvati, A., O'Brien, P. J. & Dawson, K. A. High content analysis provides mechanistic insights on the pathways of toxicity induced by amine-modified polystyrene nanoparticles. *PLoS One* **9**, 108025 (2014).

181. Bickle, M. The beautiful cell: High-content screening in drug discovery. *Analytical and Bioanalytical Chemistry* **398**, 219–226 (2010).

182. Zanella, F., Lorens, J. B. & Link, W. High content screening: Seeing is believing. *Trends in Biotechnology* **28**, 237–245 (2010).

183. Rawlinson, L. A. B., O'Brien, P. J. & Brayden, D. J. High content analysis of cytotoxic effects of pDMAEMA on human intestinal epithelial and monocyte cultures. *J. Control. Release* **146**, 84–92 (2010).

184. O'Brien, P. J. High-content analysis in toxicology: Screening substances for human toxicity potential, elucidating subcellular mechanisms and in vivo use as translational safety biomarkers. *Basic Clin. Pharmacol. Toxicol.* **115**, 4–17 (2014).

185. Anchan, A. *et al.* Real-time measurement of melanoma cell-mediated human brain endothelial barrier disruption using electric cell-substrate impedance sensing technology. *Biosensors* **9**, (2019).

186. Szulcek, R., Bogaard, H. J. & van Nieuw Amerongen, G. P. Electric cell-substrate impedance sensing for the quantification of endothelial proliferation, barrier function, and motility. *J. Vis. Exp.* (2014). doi:10.3791/51300

187. Pänke, O., Balkenhohl, T., Kafka, J., Schäfer, D. & Lisdat, F. Impedance spectroscopy and biosensing. *Adv. Biochem. Eng. Biotechnol.* **109**, 195–237 (2007).

188. Natoli, M., Leoni, B. D., D'Agnano, I., Zucco, F. & Felsani, A. Good Caco-2 Cell Culture Practices. *Toxicol. Vitr.* **26**, 1243–1246 (2012).

189. Pitt, J. A. *et al.* Uptake, tissue distribution, and toxicity of polystyrene nanoparticles in developing zebrafish (Danio rerio). *Aquat. Toxicol.* **194**, 185–194 (2018).

190. Laaksonen, T. *et al.* Failure of MTT as a toxicity testing agent for mesoporous silicon microparticles. *Chem. Res. Toxicol.* **20**, 1913–1918 (2007).

191. Liu, H., Tian, L., Wang, S. & Wang, D. Size-dependent transgenerational toxicity induced by nanoplastics in nematode Caenorhabditis elegans. *Sci. Total Environ.* **790**, 148217 (2021).

192. Ji, Y. *et al.* Realistic polyethylene terephthalate nanoplastics and the size- And surface coating-dependent toxicological impacts on zebrafish embryos. *Environ. Sci. Nano* **7**, 2313–2324 (2020).

193. Anwer, S. & Szászi, K. Measuring Cell Growth and Junction Development in Epithelial Cells Using Electric Cell-Substrate Impedance Sensing (ECIS). *BIO-PROTOCOL* **10**, (2020).

194. Domenech, J., Hernández, A., Rubio, L., Marcos, R. & Cortés, C. Interactions of polystyrene nanoplastics with in vitro models of the human intestinal barrier. *Arch. Toxicol.* **94**, 2997–3012 (2020).

195. Galkin, V. E., Orlova, A. & Egelman, E. H. Actin filaments as tension sensors. *Current Biology* **22**, R96–R101 (2012).

196. Coradeghini, R. *et al.* Size-dependent toxicity and cell interaction mechanisms of gold nanoparticles on mouse fibroblasts. *Toxicol. Lett.* **217**, 205–216 (2013).